Study of Optoelectronic Properties of Two-Dimensional Materials and Mixed-Dimensional Heterostructures through Dielectric Engineering

A thesis submitted in partial fulfillment of

the requirements of the degree of

Doctor of Philosophy

by

Vrinda Narayanan P

(Roll No. 20173562)

to

INDIAN INSTITUTE OF SCIENCE EDUCATION AND RESEARCH (IISER), Pune

January 16, 2023

Certificate

Certified that the work incorporated in the thesis entitled '**Study of Optoelectronic Properties of Two- Dimensional Materials and Mixed- Dimensional Heterostructures through Dielectric Engineering**', submitted by **Vrinda Narayanan P** was carried out by the candidate, under my supervision. The work presented here or any part of it has not been included in any other thesis submitted previously for the award of any degree or diploma from any other University or institution.

Pune-411008 **Dr. Atikur Rahman**

January 16, 2023 Supervisor

Declaration

I declare that this written submission represents my ideas in my own words and where others' ideas have been included, I have adequately cited and referenced the original sources. I also declare that I have adhered to all principles of academic honesty and integrity and have not misrepresented or fabricated or falsified any idea/data/fact/source in my submission. I understand that violation of the above will be cause for disciplinary action by the Institute and can also evoke penal action from the sources which have thus not been properly cited or from whom proper permission has not been taken when needed.

Pune - 411008 **Vrinda Narayanan P**

January 16, 2023 **Roll No - 20173562**

To my Mother

Acknowledgement

With immense pleasure, I express my indebted gratitude to all the wonderful people who have been my side during this long Ph.D. journey.

First and foremost, I express my profound gratitude and deep regard to my supervisor Dr. Atikur Rahman for his guidance, valuable feedback, and constant encouragement. I highly appreciate the freedom and space that he gave me to learn things at my pace. I admire his experimental skills and optimistic attitude. He was very approachable and always made himself available for scientific discussions.

I am greatly indebted to Gokul. His support in earning this Ph.D. degree is huge. During all the uncertain times and when in self-doubt, he gave me the confidence to move forward. I have never met someone like him, who is so selfless, caring, and down to earth. I am always inspired by his knowledge, logical way of thinking, and intellectual curiosity. I cannot thank you enough and sincerely wish to see you conquer greater heights in life.

I sincerely thank my RAC members, Dr. Pankaj Poddar and Dr. Aparna Deshpande, for all the critical feedback, thoughtful questions, and comments. I thank DST INSPIRE for the fellowship.

I extend my gratitude to my teachers Prof. Siby Mathew, Dr. Jimmy Sebastian, and Dr. Roby Cherian from Sacred Hearts College, Thevara, for motivating me to pursue Ph.D.

I am grateful to Sudhir sir for teaching various experimental techniques and always being available whenever we faced technical issues. I thank all the technical staff at hcross for all the help extended. I thank Prabhakar sir and Dhanasree mam from the Physics office and all other people from the Academic office.

It's my pleasure to thank Pranab, Bhumika, Umashankar, Manisha, and Ankit for giving me constant company and for all the fun. Thanks, Pranab for listening to me, for all our outings, fun and definitely for being my badminton partner. Many thanks to you for all the efforts that you put in for teaching me badminton. Thanks Ankit for your constant company throughout the initial years of Ph.D. I cherish the company of Bhumika and Manisha. Thanks, Bhumika for all the laughter, long walks, thoughtful discussions, cooking, gym sessions, movies, and parties. I enjoyed your company a lot. Thanks, Manisha for motivating me to join the dance class and for being my reel partner. We had great time dancing and hanging out together. Thanks Uma, for all the care and support you showered. I was also fortunate to have countless friends at IISER. Thanks to Priya and Neethu for your valuable company. Many thanks to Kundan, Amal, Diya, Naveen, Sreeram, Markose, Cavya, and Sandra for all the trips, celebrations and memorable moments. Special thanks to my batchmates Sneha, Sarvottam, Anupam, Navita, Chetna, and Sushant for making me comfortable at IISER during the initial periods.

I thank all my past and present lab members. Special thanks to Sagnik for designing the cover page for my research article and Divya chechy for your scientific insights and company. Talking to Suraj was always a stress relief for me and I really enjoyed his company. Thank you, Suraj. Thanks to Tamaghna for the scientific feedback and Sudipta for the scientific discussions. I would also like to thank Ayesha mam for her great hospitality, delicious food, and warm welcoming personality.

At IISER, I got the opportunity to play various sports like basketball, badminton, and cricket and be part of the inter-IISER sports meet (IISM). I thank my basketball coach and all my co-players. I thank all the people with whoever I have interacted at IISER.

Many thanks to my brother Vivek and my friends Indulekha, Anjali, and Abhijith for being my constant pillars throughout this journey. I am forever thankful to my

mother for constantly believing in me and encouraging me to conquer greater heights. This thesis is dedicated to you, mom. I am grateful to my father for his unconditional love and support. A huge thanks to my husband for all his love, care, support, and unwavering faith in me. Above all, I thank Almighty for giving me the ability to make it possible.

Abstract

Layered two-dimensional materials (2D) have aroused huge research interest since the breakthrough of graphene. Prominent among them are the transition metal dichalcogenides (TMDs), with distinct optical, electrical, and mechanical properties. While considered as promising candidates for future device applications, they also form the playground for exploring novel physical phenomena. In the 2D limit, TMDs experience reduced dielectric screening, making their electrical and optical properties sensitive to the surrounding environment. In this thesis, we first discuss the synthesis of TMDs using Chemical Vapor deposition (CVD). By choosing MoS_2 as a model system, the role of different growth parameters in the synthesis was systematically investigated and the growth conditions were optimized to obtain monolayer MoS_2 with centimeter-scale large-area coverage. The optoelectronic transport properties of monolayer MoS_2 were then improved by exploiting the sensitivity of TMDs to their surrounding environment. Engineering the local dielectric medium has been demonstrated to be an efficient method of modifying their optoelectronic properties. A two-order enhancement in mobility and improvement in photoresponse times were attained by modulating their surrounding dielectric medium. The strong optical absorption and excellent light-matter interaction in MoS_2 are compelling enough to employ them for various optoelectronic applications. But their atomic thickness and the associated reduced dielectric screening results in large exciton binding energy causing an inefficient separation of photogenerated carriers. Forming a p-n junction can solve this problem. The inherent electric field generated at the junction helps separate the photogenerated charge carriers. We, therefore, made a p-n junction between silicon and MoS_2, studied the optoelectronic properties, and aimed to enhance their photoresponse. A nearly three-order enhancement in photocurrent was successfully achieved by tuning their local dielectric medium. The photoresponse in these devices can often be limited by non-radiative recombinations, diminish-

ing their quantum efficiency. In the last chapter, through temperature-dependent studies, deep-level defects were identified as a major cause of recombinations limiting the photoresponse. We devised a method to reduce these recombinations by screening the deep-level defects and enhancing the device photoresponse. This thesis demonstrates the importance of the surrounding dielectric medium in determining the performance of TMD devices and illustrates a pathway of using dielectric engineering for the development of 2D materials-based high-efficiency optoelectronic devices.

Abbreviations

- **2D** : Two Dimensional
- **TMDs** : Transition Metal Dichalcogenides
- **CVD** :Chemical Vapor Deposition
- **FET** : Field Effect Transistor
- **vdW** : van der Waals
- **FESEM** : Field Emission Scanning Electron Microscope
- **HRTEM** : High Resolution Transmission Electron Microscope
- **SAED** : Selected Area Electron Diffraction
- **AFM** : Atomic Force Microscope
- **SEM** : Scanning Electron Microscope
- **PL** : Photoluminescence
- **LED** : Light Emitting Diode
- **IPA** : Isopropyl Alchohol
- **MEK** : Methyl Ethyl Ketone
- **PVDF-TrFe** : Poly(vinylidene fluoride-co-trifluoroethylene)

List of Publications

Included in the thesis

- "How to train your CVD to grow large-area 2D materials", **Vrinda Narayanan P**, Gokul M A, Atikur Rahman, *Materials Research Express*, 2019, 6(12), 125002

- "Improving the optoelectronic properties of monolayer MoS_2 field effect transistor through dielectric engineering", **Vrinda Narayanan P**, Gokul M. A., Chetna Taneja, G.V Pavan Kumar, Atikur Rahman, *(Submitted)*

- "Giant Photoresponse Enhancement in Mixed-Dimensional Van der Waals Heterostructure through Dielectric Engineering", **Vrinda Narayanan P**, Gokul M. A., Tamaghna Chowdhury, Chandan K. Singh, Shailendra Kumar Chaubey, Takashi Taniguchi, Kenji Watanabe, Mukul Kabir, G. V. Pavan Kumar, Atikur Rahman, *Advanced Materials Interfaces*, 2022, 9(9), 2102054

- "Role of Defects in the Transport Properties and Photoresponse of a Silicon–MoS_2 Mixed-Dimensional Van der Waals Heterostructure", **Vrinda Narayanan P**, Gokul M Anilkumar, Manisha Rajput, Atikur Rahman, *ACS Applied Electronic Materials*, 2022, 4(12), 6038–6046

Contributed Works (not included in the thesis)

- "Modulating flow near substrate surface to grow clean and large-area monolayer MoS_2", M A Gokul, **Vrinda Narayanan P**, Atikur Rahman, *Nanotechnology*, 2020, 31(41), 415706

- "Conformal growth of high-quality monolayer TMDs- Towards novel devices via morphology control" Gokul M. A, **Vrinda Narayanan P**, Aditi Moghe,

Shailendra K Chaubey, G. V. Pavan Kumar, Prasenjit Ghosh, , Stéphane Berciaud, Sooyeon Hwang, and Atikur Rahman. *(Submitted)*

Conference presentations

- "Understanding the interface of Silicon- MoS_2 heterostructure", **Vrinda Narayanan P (presenting author)**, Atikur Rahman, *Energy Day*, IISER Pune, 2018 (Poster presentation)
- "Dielectric Engineering in Silicon- MoS_2 Heterostructure", **Vrinda Narayanan P (presenting author)**, Atikur Rahman, *International Conference on Nano Science and Technology (ICONSAT)*, Kolkata, March 2020 (Poster Presentation) : Recieved Best poster award
- "Large Enhancement of Photoresponse Through Dielectric Engineering in Silicon-MoS_2 Heterostructure ", **Vrinda Narayanan P (presenting author)**, Atikur Rahman, *Materials Research Society Hybrid Fall Meeting and Exhibit*, 2021 (Oral presentation)
- "Giant Photoresponse enhancement in mixed-dimensional van der Waals heterostructure through dielectric engineering", **Vrinda Narayanan P (presenting author)**, Atikur Rahman, *APS March Meeting* , 2022 (Oral presentation)

Contents

List of Figures **xvii**

1 Introduction **1**

1.1 Overview of two-dimensional materials 1

1.2 Molybdenum disulfide (MoS_2) 3

1.3 Effect of surrounding dielectric medium 5

1.3.1 Modulation of bandgap and exciton binding energy by dielectric medium 6

1.3.2 Dielectric screening of defects 8

1.3.3 Dielectric screening of Coulomb impurities 11

1.4 Applications of MoS_2 13

1.5 Field effect transistors 14

1.6 Mixed-dimensional van der Waals heterostructures 16

1.7 Thesis outline 17

2 Experimental Techniques **19**

2.1 Synthesis techniques 19

2.1.1 Chemical Vapor Deposition(CVD) 19

2.2 Spectroscopic Techniques 23

2.2.1 Raman Spectroscopy 23
2.2.2 Photoluminiscence Spectroscopy 26
2.3 Microscopic Techniques 28
2.3.1 Atomic Force Microscopy 28
2.3.2 Scanning Electron Microscopy 29
2.3.3 Transmission Electron Microscopy 30
2.4 Low-frequency noise spectroscopy 31
2.4.1 Hooge Model 32
2.4.2 McWhorter model 33
2.5 Device fabrication 35
2.5.1 Photolithography 35
2.5.2 Thermal Evaporation 37
2.5.3 Etching Processes 38

3 Synthesis of 2D Transition Metal Dichalcogenides 41

3.1 Introduction 41
3.2 Experimental details 43
3.3 Results and discussions 44
3.3.1 Effect of growth promoter (NaCl) 44
3.3.2 Effect of position of the substrate 51

3.3.3 Effect of temperature 53

3.3.4 Effect of flowrate 55

3.4 Summary 57

4 Modulating the Transport Properties of Monolayer MoS_2 FET through Dielectric Engineering 59

4.1 Introduction 59

4.2 Experimental details 61

4.3 Results and discussions 63

4.3.1 Transfer Characteristics 63

4.3.2 Output Characteristics 67

4.3.3 Time resolved photoresponse 69

4.4 Summary 71

5 Photoresponse Enhancement in Mixed-Dimensional vdW Heterostructure through Dielectric Engineering 72

5.1 Introduction 72

5.2 Experimental details 75

5.2.1 CVD synthesis of MoS_2 75

5.2.2 Heterostructure fabrication 75

5.3 Results and discussions 77

5.3.1 Optical Charactersation 77

5.3.2 Electrical Characterisation 79

5.3.3 Temperature dependent study 80

5.3.4 Time resolved photoresponse 82

5.3.5 Optoelectronic studies 82

5.4 Effect of dielectric environment 84

5.4.1 Effect of varying the dielectric environment 87

5.5 Summary 91

6 Role of Defects on the Transport Properties and Photoresponse of Silicon-MoS_2 Heterostructure 93

6.1 Introduction 93

6.2 Experimental details 95

6.3 Results and discussions 96

6.3.1 Electrical Characterisation 96

6.3.2 Temperature dependence of ideality factor (n) 99

6.3.3 Space charge limited current (SCLC) 100

6.3.4 Temperature dependence of photocurrent 101

6.3.5 Photocurrent enhancement with dielectric medium 102

6.3.6 Temperature dependence of time-resolved photoresponse 103

6.3.7 Temperature dependence of intensity-dependent photocurrent 105

6.3.8 Temperature dependence of low frequency 1/f noise 107

6.4 Summary 109

7 Conclusions and Future Directions **111**

7.1 Conclusions 111

7.2 Future directions 112

Bibliography **113**

List of Figures

1.1 (a) Top view of monolayer MoS_2 (b) Different polymorphs of MoS_2. Image reproduced with permission from [1] 4

1.2 (a) The change in the transition levels of donor and acceptor impurity in MoS_2 as a function of the environmental dielectric constant. Image reproduced with permission from [2] (b) Transition level of defects in monolayer MoS_2, WS_2, and in MoS_2/WS_2 vdW heterostructure as a function of dielectric constant. Image reproduced with permission from [3].Copyright © 2018, American Chemical Society 10

1.3 The effect of different dielectric mediums on the Coulomb potential of a point charge. Image reproduced with permission from [4] 12

2.1 Various steps involved in chemical vapor deposition process. Image reproduced with permission from [5] 20

2.2 Home built CVD set up used for synthesis 23

2.3 (a) Band structures evolution of MoS_2 at various number of layers (b) Photoluminescence spectra MoS_2 layers with different thickness. Images reproduced with permission from [6], Copyright © 2010 American Chemical Society 27

2.4 Superposition of different Lorentzians forming a $1/f$ spectrum. Image reproduced with permission, from [7] Copyright © 2007, IEEE 34

2.5 Schematic of projection lithography. Image reproduced with permission from[8] 36

2.6 Schematic of the thermal evaporation system. Image reproduced with permission from [9] Copyright © 2021, American Chemical Society . 37

2.7 (a) and (b) Different patterns of devices fabricated, (c) and (d) Multiple devices fabricated on a substrate 38

2.8 Schematic of the Reactive Ion Etching system. Image reproduced with permission from [10] 39

2.9 Home-built reactive ion etching setup used for dry etching. 40

3.1 Optical microscope images of the sample synthesized (a) without salt (b) with salt coated over the substrate. Scale bar: 20 µm. (c) Comparison of MoS_2 monolayers formed over the entire substrate (right) with a bare substrate (left). 45

3.2 FESEM images of the MoS_2 samples synthesized (a) without salt (b) with salt coating. Scale bar (a) 1 µm(b) 10 µm. 46

3.3 (a,b) HRTEM image (bottom inset: SAED pattern, top inset : d spacing) of monolayer MoS_2 46

3.4 (a) Raman and (b) photoluminescence spectra of samples with and without salt coating. It is clearly evident that a similar quality monolayer is obtained in both cases. The absence of any additional peak on the lower side of the Raman spectra indicates no additional disorder is present in the sample synthesized with NaCl. 47

3.5 *I-V* characteristics and *I-t* characteristics of the MoS_2 sample synthesized (a), (b) without salt (c), (d) with salt coated over the substrate. White LED of 0.15 mW cm^{-2} intensity was used for the photocurrent measurement in (a) and (c). UV LED of 405 nm wavelength and 12 mW cm^{-2} intensity was used for the transient photoresponse measurement shown in (b) and (d) 49

3.6 Source-drain current versus back gate voltage sweep (I_{sd}- V_{bg}) and source-drain current versus source-drain voltage sweep (I_{sd}- V_{sd}) of devices made on the MoS_2 film synthesized (a), (b) without salt, and (c), (d) with salt. I_{sd}-V_{bg} characteristics show n-type unipolar behavior and good current saturation observed in I_{sd}- V_{sd} characteristics for both type of sample. 50

3.7 (a) Schematic of the effect of position of substrate (distance measured from the edge of the MoO_3 boat) and (b) the schematic shows the variation of coverage of the film over the substrate with the position of the substrate. (c)–(h) Optical images of the sample placed at various distances. Scale bar: 100 µm. 52

3.8 Optical microscope images of samples synthesized at various temperatures for different positions of substrates. Scale bar 20 µm. 54

3.9 Optical images of the obtained MoS_2 sample at a different flow rate of argon: (a) 5 sccm (b) 7.5 sccm (c) 10 sccm (d) 15 sccm. Scale bar 20 µm. It is clear that at 7.5 sccm flow a continuous clean monolayer is obtained with minimal overgrowth. 56

3.10 Continous monolayer of MoS_2 obtained over the entire substrate (bottom). Bare Si/SiO_2 substrate (top) for comparison. 57

4.1 (a) Schematic of the device geometry and PDMS well patterned around the device to restrict the liquid just at the top of the device (b) Optical microscope image of the device fabricated over monolayer MoS_2.To avoid any leakage current, the liquid was prevented from coming in direct contact with the metal contacts by depositing silicon nitride and an opening (area within the dotted lines) was made at the semiconducting channel to control the surrounding dielectric environment. (c) Raman spectra and (d) Photoluminescence (PL) spectra of monolayer MoS_2. 62

4.2 (a) Comparison of transfer characteristics of MoS_2 FET in the presence of various dielectric mediums. (V_g^* is the gate voltage at which I_{sd} starts increasing above the OFF state) (b) Mobility as a function of the dielectric constant of different mediums. 64

4.3 Variation of conductivity (σ) with ΔV_g in (a) air and in the presence of different dielectric mediums (b) Anisole (c) Novec (d) MEK. The dependence of conductivity on the carrier density can give information about the nature of screening of Coulomb impurities. 66

4.4 Source drain characteristics in the presence of (a) air, (b) hexane and (c) MEK as the surrounding dielectric medium. 68

4.5 (a) Time-resolved photoresponse across monolayer MoS_2 when illuminated with 405 nm LED at an intensity of 10 mW/cm^2. Comparison of (b) rising edge (c) falling edge, (d) rise time, and fall time in the presence of various dielectric mediums. 69

5.1 (a) AFM image and (b) Line profile (corresponding to the blue line in fig.(a)) of the silicon surface after etching the SiO_2 layer. 76

5.2 Schematic of the steps involved in patterning the SiO_2/Si substrate and subsequent transfer of monolayer MoS_2 to form the Si- MoS_2 heterostructure. 77

5.3 (a) FESEM and (b) Optical microscope images of the silicon– MoS_2 heterostructure. In the optical image monolayer MoS_2 is only visible on the SiO_2 part. (c) Photoluminescence (PL) and (d) Raman spectra of as-grown monolayer MoS_2 before and after transferring on to the patterned substrate. 78

5.4 (a) *I–V* characteristics of the Si–MoS_2 heterostructure in the absence and presence of light (535 nm LED of intensity 2 mW cm^{-2}. The reverse current increases in the presence of light with a nearly constant forward current exhibiting a photodiode-like behavior. (b) *I-V* characteristics of a device fabricated on silicon with gold contacts. (c)Gate dependent *I-V* characteristics of a device fabricated on MoS_2 with gold contacts.The linear and symmetric *I–V* characteristics confirm the formation of nearly Ohmic contacts at the MoS_2-Au and silicon-Au interface and hence the nonlinear *I–V* characteristics of the Si-MoS_2 heterostructure is due to the formation of the p-n junction. 80

5.5 (a)Dark current (normalised by 40 ℃ value) for 3V reverse and forward bias. While the reverse current increases with temperature, the forward bias current does not show any significant temperature dependence. (b) Reverse bias dark *I-V* characteristics measured in the temperature range from 30 ℃ to 140 ℃. (c) Temperature-dependent current at an applied reverse bias of -3 V in dark and in the presence of light. With increasing temperature dark current increases and the photocurrent decreases. 81

5.6 (a)Time-dependent photocurrent under the illumination of a 535 nm LED with intensity 2 mW cm^{-2} at a bias of -2 V. (b) Rise time and (d) fall time indicating a faster rise and fall time. 82

5.7 (a) Plot showing the dependence of photocurrent with an incident light intensity of the heterojunction when illuminated using a 465 nm LED. The data points are fitted well by the power law. (b) Responsivity and detectivity as a function of the power density of an incident wavelength of 465 nm. Both the responses were measured at an applied reverse bias of 3 V. 83

5.8 (a) Reverse bias I–V characteristics in the presence of light before and after coating PVDF-TrFe. (b) Responsivity as a function of different wavelengths in the presence and absence of PVDF-TrFe coating. The responsivity ratio with and without PVDF-TrFe coating has been shown as a function of wavelength in the inset. (c) The photocurrent is shown as a function of power density when illuminated with a 465 nm LED at an applied reverse bias of 3 V in the presence and absence of PVDF-TrFe coating (blue line indicates linear fitting). 85

5.9 Normalized photoresponse is shown for devices with and without a high dielectric environment (here, Novec). From the data, it is clear that in the presence of a large dielectric constant environment, the temporal response is faster, and the slow part is absent. 86

5.10 (a) Device geometry of the test device used for measuring the conductivity of the liquid dielectric mediums without MoS_2. (b) Device geometry of the silicon- MoS_2 heterostructure (c) I-V curve showing the current as a function of voltage passing through various liquid mediums alone. 88

5.11 (a) Ratio of reverse bias photocurrent in the presence of various dielectric mediums shown as a function of bias voltage. (b) Enhancement of photocurrent shown as a function of relative dielectric constant with respect to air for -3 volt bias 88

5.12 Photoluminescence spectra of monolayer MoS_2 in the presence and absence of deionised water 89

6.1 (a) Optical microscope image and (b) FESEM image of a monolayer MoS_2 transferred onto a patterned Si/ SiO_2 substrate. (c) Raman spectrum of monolayer MoS_2. 97

6.2 (a) *I-V* characteristics of silicon-MoS_2 p-n junction in the absence and presence of light. An asymmetric *I-V* curve with a rectification ratio of nearly 10^2 at $\pm$ 2 V was obtained. At a reverse bias of 2 V, the current enhances by 30 times upon illumination under 630.nm light of intensity 2 mW/cm^2 (b)*I-V* characteristics (under dark conditions) measured across MoS_2 using Cr/Au as contact electrode. 97

6.3 (a) Temperature-dependent dark *I-V* characteristics (b) Rectification ratio measured at 2 V as a function of temperature. 99

6.4 (a)Variation of barrier height and ideality factor with temperature. (b)Ideality factor calculated from dark *I-V* characteristics plotted as a function of inverse temperature and (c) temperature. 100

6.5 (a) Log-log plot of forward current versus voltage of the pristine silicon-MoS_2 p-n junction. (b) Plot of the power law exponent with inverse temperature. 101

6.6 (a) Variation of photocurrent with the temperature of the silicon-MoS_2 p-n junction in the presence and absence of PVDF-TrFe at a reverse bias of 2 V.(b) Plot of log of photocurrent versus inverse temperature in the absence of PVDF-TrFe (c) Dependence of responsivity corresponding to (a) with temperature 102

6.7 (a) Time-resolved photoresponse and (b) rise time and fall time of a pristine silicon-MoS_2 p-n junction when illuminated with a 630 nm LED at a reverse bias of 3 V at 300 K. Comparison of the (c) rise time (τ_r) and (d) fall time (τ_f) with temperature in the presence and absence of PVDF-TrFe. The generation of more shallow levels by the dielectric medium increases the lifetime of the photogenerated carriers. 104

6.8 (a) Intensity-dependent photocurrent measured at a reverse bias of 2 V and temperatures 50K and 300K. (b) Dependence of the exponent (α) in the power law $I \propto P^{\alpha}$ with temperature.A transition from bimolecular to monomolecular recombination is observed with an increase in temperature. 106

6.9 Normalized noise spectral density of silicon-MoS_2 p-n junction at 2 V reverse bias under dark conditions in the (a) presence and (b) absence of PVDF-TrFe at different temperatures. Comparison of (c) variation of normalized noise spectral density at 10 Hz frequency and (d) Noise amplitude (A) with temperature in the presence and absence of PVDF-TrFe. Hopping conductivity through the defect states (localized states) causes $1/f$ noise. 108

Chapter 1

Introduction

Dimensionality strongly influences the properties of materials. The same material can show drastically different properties depending on their dimensions. Two-dimensional (2D) materials, due to strong quantum confinement in the vertical direction, exhibit remarkably different electronic and optical properties from that of their bulk counterparts. Of all low-dimensional materials, only two-dimensional (2D) materials have a bulk counterpart, making them extremely interesting. They have a layered structure and can be easily synthesized using a bottom-up or top-down approach. Present reports suggest that the 2D family consists of around 1800 layered materials [11], with a wide range of conduction mechanisms from metallic, semimetallic, semiconducting, insulating to superconducting.[12]

1.1 Overview of two-dimensional materials

The advent of 2D materials started with the successful isolation of graphene by K.S. Novoselov and A.K. Geim in 2004.[13] With a simple technique like mechanical exfoliation using a scotch tape, they unraveled the unique properties of graphene and revamped the unchallenged belief that atomic monolayers cannot exist in the free-standing form.[13] The great scientific drive towards graphene originated from its peculiar electronic structure. The charge carriers follow a linear dispersion relation and mimic massless relativistic particles.[14] They have demonstrated remarkable properties like very high mobility greater than 10^5 $cm^2V^{-1}s^{-1}$ [15], high electrical conductivity ($\sim$ 10^4 $\Omega^{-1}cm^{-1}$), large room temperature thermal conductivity

(3×10^3 $Wm^{-1}K^{-1}$), high Young's modulus (1.1 TPa), large specific surface area, and high optical transmittance ($\sim 97.7\%$).[16] Despite the rich physics and potential applications graphene offers, the absence of a bandgap limits its use in switching applications like logic devices and field effect transistors. This diverted the research attention toward other 2D materials. Transition metal dichalcogenides (TMDs) with finite bandgaps were the first descendants of graphene that triggered research interest.

TMDs are a class of layered materials, denoted as MX_2, where M corresponds to transition metal (Mo, W, Pt, Pd) and X to chalcogens (S, Se, Te). A single layer of TMD is composed of hexagonally arranged transition metal atoms sandwiched between two layers of hexagonally arranged chalcogen atoms. Different layers with strong in-plane covalent bonding are held together by weak van der Waals forces to form a bulk crystal.[17] In general, TMDs like MoS_2, WS_2, WSe_2,$MoSe_2$ are semiconducting and have an indirect bandgap in their bulk form and undergo a cross-over to direct bandgap in their monolayer form, with the bandgap increasing with decreasing number of layers.[18] They also have additional features like strong spin-orbit coupling, large oscillator strength, valley degree of freedom, and inversion symmetry breaking in the odd number of layers, making them suitable for valleytronics, spintronics, optoelectronics, and various non-linear optical applications.[17] TMDs like TaS_2, $TiSe_2$, $NbSe_2$ on the other hand are metallic and exhibit exotic physical properties like superconductivity and charge density waves.[19] It is worth mentioning that TMDs were known and were used extensively for applications like lubrication and catalysis, even before the discovery of graphene. For example, monolayer MoS_2 was first isolated in 1966 mechanically using an adhesive tape [20] and 20 years later using chemical exfoliation.[21]

Post-metal chalcogenides like SnS, GaS, SnS, $InSe_2$, SnS_2 have also generated huge interest due to their large photoresponsivity,in-plane anisotropy, and high mo-

bility. SnS_2 with a large direct bandgap of around 2.8 - 2.9 eV is considered ideal as a buffer layer in solar cells.[22] The larger optical absorption coefficient, and high transmittance, along with a bandgap of 0.9 eV to 1.8 eV, makes SnS a suitable choice as an absorber layer in photovoltaic applications.[23]

Hexagonal boron nitride (hBN) is another widely studied 2D material. It is a wide bandgap insulator and is considered a graphene analog with carbon atoms replaced by boron and nitrogen. The atomically smooth and dangling bond-free surface makes hBN an ideal choice as gate dielectric and encapsulating material for various 2D material applications.[24]. They are suitable as deep UV emitters and detectors and exhibit single photon emission at room temperatures.[25]

Besides 2D compounds, several 2D elemental materials like borophene (B), phosphorene (P), antimonene (Sb), bismuthene (Bi), silicene (S), arsenene (As), etc. are also being explored.[26] Sb, As, and Bi display distinct topological insulator properties. Black phosphorus has a puckered atomic structure and exhibits large in-plane anisotropy in optical conductivities and absorption, which makes them an ideal candidate for light modulators and viable linear polarizers.[27] With a bandgap intermediate of graphene and TMDs, they display exciting properties like high field effect mobility, tunable direct bandgap at all thicknesses, strong photon absorption, etc. But their instability under ambient conditions poses a limitation.[27] In this thesis, we focus on the properties and applications of single-layer MoS_2.

1.2 Molybdenum disulfide (MoS_2)

MoS_2 is a layered TMD with a single layer composed of three atomic planes of S-Mo-S atoms arranged in a hexagonal lattice structure. Different layers interact through weak van der Waals forces, whereas within a layer, molybdenum and sulfur atoms

are held together by strong covalent bonds. A single layer MoS_2 has a thickness of 0.65 nm.[28] Depending on the coordination of the metal atoms and the stacking order of the metal chalcogen metal plane, bulk MoS_2 exist in 3 different polytypes- 1T, 2H, and 3R.[17] Here the letters H, T and R respectively denote hexagonal, tetragonal and rhombohedral symmetry and the number represents the number of layers per unit cell. 2H, and 3R polytypes have trigonal prismatic coordination (D_{3h}) of Mo-atoms, with different stacking orders. 2H is the most stable phase and has a bravais hexagonal lattice structure. On the other hand, the 1T phase is a metastable phase with octahedral coordination (O_h) of Mo-atoms. Through atomic gliding of the layers, 2H and 1T phases can be transformed into one another.[17] While 2H and 3R phases are semiconducting, 1T is metallic. Monolayer MoS_2 can exist in the 2H or 1T phase.[28]

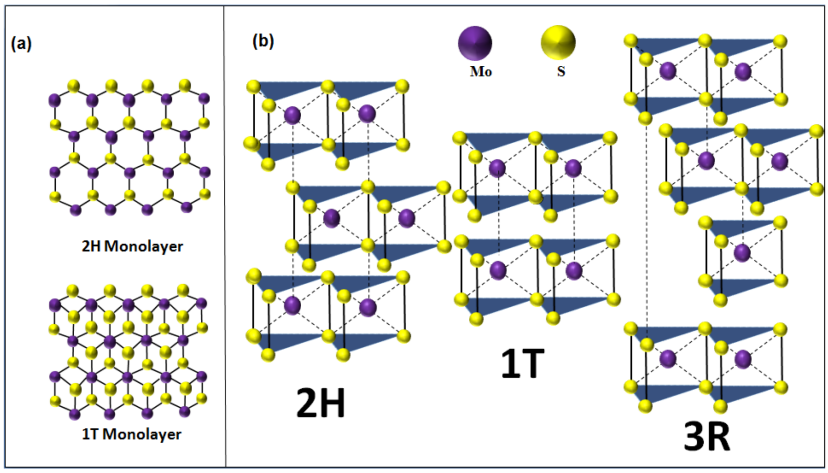

Figure 1.1: (a) Top view of monolayer MoS_2 (b) Different polymorphs of MoS_2. Image reproduced with permission from [1]

MoS_2 has an indirect bandgap of 1.2 eV in bulk with the valence band maximum positioned at Γ point and conduction band minimum along the Γ-K direction in the hexagonal Brillouin zone. When thinned down, due to the increased quantum confinement effect and decreased interlayer interactions, the bandgap increases and becomes direct (1.9 eV) at the K point of the Brillouin zone in the monolayer limit.[18]

This cross-over from indirect to direct bandgap results in an enhanced photoluminescence efficiency in monolayers, which is 10^4 times compared to that of bulk.[6] The absence of an inversion centre in monolayer MoS_2, along with strong quantum confinement of carriers and large mass of the constituent elements, results in strong spin-orbit splitting.[29] The absence of dangling bonds and thermal stability up to 1100 ℃ in vacuum also escalates the interest in MoS_2. Monolayer MoS_2 has a large Youngs modulus of 270 ± 100 GPa, comparable to steel, and exhibits good mechanical flexibility. It can sustain elastic deformations up to 25 % [30] before rupture and can withstand strain up to 11%.[31] It also has a comparable Seebeck coefficient and larger bending modulus to that of graphene.[30] The exciting electrical, optical and mechanical properties exhibited by MoS_2 makes it a multipurpose material suitable for fundamental scientific studies as well as in various emerging applications.

1.3 Effect of surrounding dielectric medium

Owing to the atomic thickness, monolayer TMDs experience reduced dielectric screening. This results in strong electron-electron and electron-hole Coulomb interactions leading to large exciton binding energies and quasiparticle bandgaps.[32, 33, 34] But in the presence of a surrounding dielectric medium, these long-range Coulomb interactions get screened, and the band gap and exciton binding energies reduce by several hundreds of meV.[35, 36, 37] Therefore, the electronic transport and optical transitions in monolayer TMDs become very sensitive to the surrounding dielectric environment and can be efficiently tuned by modulating the surrounding medium.[36] Furthermore, the dielectric medium also have a strong influence on the defect transition levels and Coulomb impurity scattering in TMDs.[2, 38]

1.3.1 Modulation of bandgap and exciton binding energy by dielectric medium

In monolayer TMDs, the electric field lines between electrons and holes lie mostly outside the film and are majorly unscreened. But if the separation between the electron and hole (r) is of the order of the thickness of the film, some of the field lines lie within the film and are partially screened. This inhomogeneous environment creates a non-local dielectric screening phenomenon in 2D TMDs, leading to large exciton binding energy (E_b) (100s of meV), small exciton radius and non-hydrogenic electrostatic potentials $V_{2D}(r)$.[36] When there is a large dielectric mismatch between the TMD layer and the surrounding dielectric environment, the effective interaction potential between the charge carriers given by Keldysh [39] follows[40]

$$V_{2D}(r) = \frac{\pi e^2}{(\epsilon_1 + \epsilon_2) r_0} [H_0(\frac{r}{r_0}) - Y_0(\frac{r}{r_0})] \tag{1.1}$$

where H_0 and Y_0 is a Struve function and a Bessel function of the second kind, respectively. Here the effective screening length r_0 depends on the polarisability of the 2D film, and ϵ_1, ϵ_2 are the dielectric constant of the top and bottom surrounding environment. At large electron–hole separations $r \gg r_0$, the potential $V_{2D}(r) \sim \frac{1}{r}$, similar to classical 3D Coulomb law and at short distances ($r \ll r_0$) screening by the 2D film becomes strong, with $V(r) \propto \log(r)$.[40] Knowing the above-screened interaction potential, the exciton binding energy can be calculated using the effective mass approximation theory.[36] With an increase in the dielectric screening, the strength of interaction potential decreases, and the exciton binding energy decreases. The exciton binding energy and the effective dielectric constant ($\epsilon_{\text{eff}} = \epsilon_1 + \epsilon_2$) are related through the scaling relationship [36]

$$E_{b0} = E_{b0}(\epsilon_{eff})^{\alpha} \tag{1.2}$$

where E_{b0} is the exciton binding energy in vacuum and α is an empirical scaling factor.

The quasiparticle bandgap (E_g) in a 2D TMD is given by the energy difference between the quasiparticle conduction and valence bands. This bandgap has contribution from two different effects- carrier confinement and dielectric screening. The geometric confinement of carriers results in an increase in kinetic energy causing the bandgap to increase. In addition, the strong Coulomb interactions between the charge carriers enhance the self-energy associated with the repulsive interaction between similar charges and increase the quasiparticle band gap.[41] If we recall the fact that the quasiparticle conduction band measures the electron affinity and valence band of the ionization potential of electrons. When an excess charge is created, the TMD material and the surrounding environment get polarized in such a way that the potential energy of the charge depends on their local dielectric environment.[42]The bandgap gets renormalized due to the change in this self-energy of the electron due to dielectric screening.[36]

Using GW calculations, the electronic bandgap of MoS_2 was estimated to be around 2.8 eV.[35] But the experimentally observed values are always less than this. These differences indicate that the traditional concept of assigning a specific bandgap to a material does not apply to 2D materials. The value of their bandgap sensitively depends on the surrounding environment. For instance, experimental results show that the electronic bandgap, optical bandgap, and exciton binding energy of a monolayer $MoSe_2$ when placed on a bilayer graphene substrate changes from their free-standing values of 2.26 eV , 1.61 eV, 0.65 eV to 2.18 eV, 1.63 eV, and 0.55 eV respectively.[33] This concept of dielectric-dependent bandgap renormalization has also been used in designing lateral heterojunctions [43, 37] and tunable bandgap transistors. [35] Though the electronic bandgap and exciton binding energies are sensitive to the surrounding dielectric medium, the optical transition energy ($E_{op} = E_g$

- E_b) is relatively insensitive.[42, 36] This is due to the counteracting changes in exciton binding energy and bandgap renormalization energy with dielectric screening, which are equal in magnitude but opposite in sign.[36]

1.3.2 Dielectric screening of defects

Defects in a semiconductor introduce electronic energy levels within the bandgap and strongly influence their electrical and optical properties. Depending on their position in energy, defects can be classified as deep or shallow. Deep defects have energy levels deep within the bandgap, with larger ionization energies and therefore contribute only fewer free charge carriers. Those levels lying at the middle of the bandgap with equal capture cross sections for both electrons and holes behave like recombination centers.[44] Non-radiative recombination of electrons and holes can contribute to energy and carrier losses and reduce the efficiency of the material.[45] But shallow levels on the other hand have energy levels closer to the conduction or valence band edges, $\sim$ 0.1 eV below, and can get thermally ionized at room temperature, generating free carriers. For electronic device applications, shallow defects are favorable because of their profound role in controlling electrical conductivity and doping in semiconductors.[2] In contrast, deep defects are detrimental, as they decrease the mobility and carrier lifetime due to the scattering and recombination of the charge carriers. Hence finding methods to suppress the deep defect levels while preserving the electronic property of the semiconducting materials becomes important.[46]

Different types of defects are usually found in TMDs, which could have been introduced either during the growth or in the post- processing stages. Due to their lower formation energies, anion vacancies are the most commonly found point defects in TMDs.[47] Sulfur vacancies, for example, present in MoS_2, introduces deep

electron trap and shallow hole trap levels. Similarly, antisite defects formed when the molybdenum atom replaces sulfur atoms create a deep electron trap, a shallow hole trap attached to the valence band edge and a deep hole trap adjacent to the electron trap close to the Fermi energy.[48] The radiative direct recombination time in a perfect monolayer MoS_2 was calculated to be 388 ps. But the presence of antisites accelerates the recombination by a factor 8.3, whereas vacancies by a factor of 1.7. [48] Various methods like the introduction of additional dopants and alloying the constituent atoms in the semiconductor were developed to suppress the deep defect levels. But these methods were challenging due to the difficulty in controlling the solubility of the foreign dopants, exact composition, etc.[46]

A simpler and more convenient method to tune the defect levels in 2D materials can be achieved by modulating their surrounding dielectric environment. A defect with charge q has a formation energy given by [49, 50]

$$E_f(q) = E_{tot}(q) - E_{host} + \sum_i n_i \mu_i + q\mu_e \tag{1.3}$$

where $E_{tot}(q)$ and E_{host} are the total energies of the material in the presence and absence of defect, n_i atoms of different species i with chemical potential μ_i are exchanged during defect formation and the Fermi energy μ_e spans from valence band maximum (VBM) to the conduction band minimum (CBM). The charged transition level (CTL) of a defect is described as the fermi energy at which the formation energies of two nearby charged states q and $q^{'}$ are equal, given by[49, 50]

$$\mu(q|q^{'}) = \frac{E_{tot}(q) - E_{tot}(q^{'})}{q^{'} - q} \tag{1.4}$$

The energy needed to free an electron or hole given by the defect ionization energy is then the difference between the CTL and the band edges (CBM for acceptors and VBM for donors) The presence of a surrounding dielectric environment screens

the Coulomb interaction between the charges and affects the formation energy of the charged states, which in turn changes the ionization energy. As the screening of the environment increases, the energy needed to ionize the defects decreases, creating shallower defect levels.

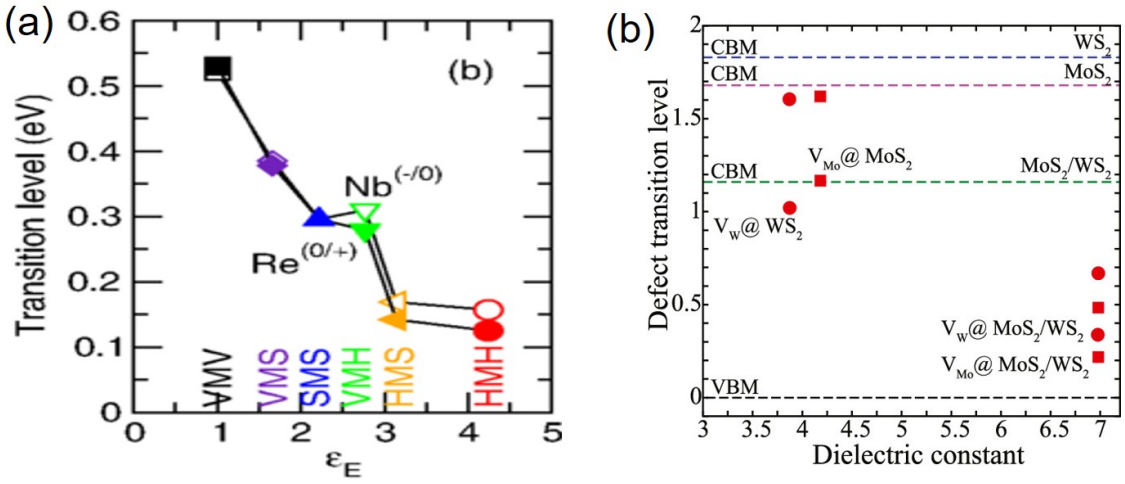

Figure 1.2: (a) The change in the transition levels of donor and acceptor impurity in MoS_2 as a function of the environmental dielectric constant. Image reproduced with permission from [2] (b) Transition level of defects in monolayer MoS_2, WS_2, and in MoS_2/WS_2 vdW heterostructure as a function of dielectric constant. Image reproduced with permission from [3].Copyright © 2018, American Chemical Society

DFT calculations have shown the energy levels of the defect transitions in MoS_2 to increase with increasing dielectric constant of the encapsulating medium.[2] The strong Coulomb interactions associated with the deep defect levels tend to strongly localize the charge carriers. But in the presence of a high dielectric surrounding medium, the Coulomb interactions between these bound electrons and the charged defects get screened. This screening spreads defect charge densities by delocalizing their spatial distributions and generates shallow levels.[2] In another study, a heterostructure formed between MoS_2 and WS_2 caused the deep levels in the individual monolayers to undergo a transition to shallow levels due to the change in the effective dielectric constant. The study showed that using this method of heterostructuring,

the deep levels corresponding to the molybdenum and tungsten vacancy in MoS_2 and WS_2 respectively become shallower by nearly 4 and 2 times.[3] Hence controlling the effective dielectric constant of the surrounding medium is a simple and powerful method to tune the defect levels in 2D materials.

1.3.3 Dielectric screening of Coulomb impurities

The electronic transport in 2D TMD is very sensitive to their surrounding environment. Due to their atomic thickness, the charge carriers are susceptible to various intrinsic and extrinsic scattering sources.[51] Hence the values of field effect mobility, one of the key transport parameters, are observed to be far lower than their theoretically predicted values. For example, in MoS_2, at room temperature, theoretically predicted phonon limited mobility is around 410 $cm^2V^{-1}s^{-1}$.[52] But in a backgated geometry, the experimentally observed value is often one order less than this.[53] Coulomb impurities present within the TMDs or at the substrate surface often scatter the charge carriers and have been identified to play a dominant role in determining the charge transport.[54, 55, 38] Various studies have shown that scattering from these Coulomb impurities can be reduced and mobility significantly improved by placing the 2D TMD in a high dielectric medium.[56, 4, 57, 54, 38]

Consider a single layer of MoS_2 of thickness a , and dielectric constant ϵ_s, with a point charge e placed inside the layer at (0,0,z_0). In the presence of a dielectric environment with dielectric constant ϵ_e, an infinite sequence of image charges forms at points $z_n = na + (-1)^n z_0$, where n 0,1,2... due to the dielectric mismatch between the semiconducting film and the environment. Magnitude of n^{th} point charge will be $e\gamma^n$, where γ is a measure of dielectric mismatch given by $\gamma = \frac{\epsilon_s - \epsilon_e}{\epsilon_s + \epsilon_e}$. In the absence of any screening, the potential encountered by a mobile electron at a point $(\vec{\rho}, z)$ due

to an ionized Coulomb impurity within the film is given by [56, 4]

$$V_{\text{unsc}}^{\text{Coul}}(\rho, z) = \sum_{n=-\infty}^{\infty} \frac{e\gamma^{|n|}}{4\pi\epsilon_0\epsilon_s\sqrt{|\vec{\rho}|^2 + [z - z_n]^2}} \tag{1.5}$$

If $\epsilon_e < \epsilon_s$, all the image charges will have the same sign and the electron experiences a larger effective potential whereas when $\epsilon_e > \epsilon_s$, the effective potential reduces and the image charge's sign alternate between positive and negative.[56] The effect of dielectric mismatch diminishes above a critical film thickness of $a_{cr} \sim \frac{a_B{}^*\epsilon_e}{\epsilon_e+\epsilon_s}$, where $a_B{}^*$ is the hydrogenic Bohr radius in bulk semiconductor, and the Coulomb scattering becomes bulk like.[56] Hence scattering of charge carriers due to Coulomb impurities in a thin film can be suppressed by surrounding it with insulating dielectric materials with $\epsilon_e > \epsilon_s$.

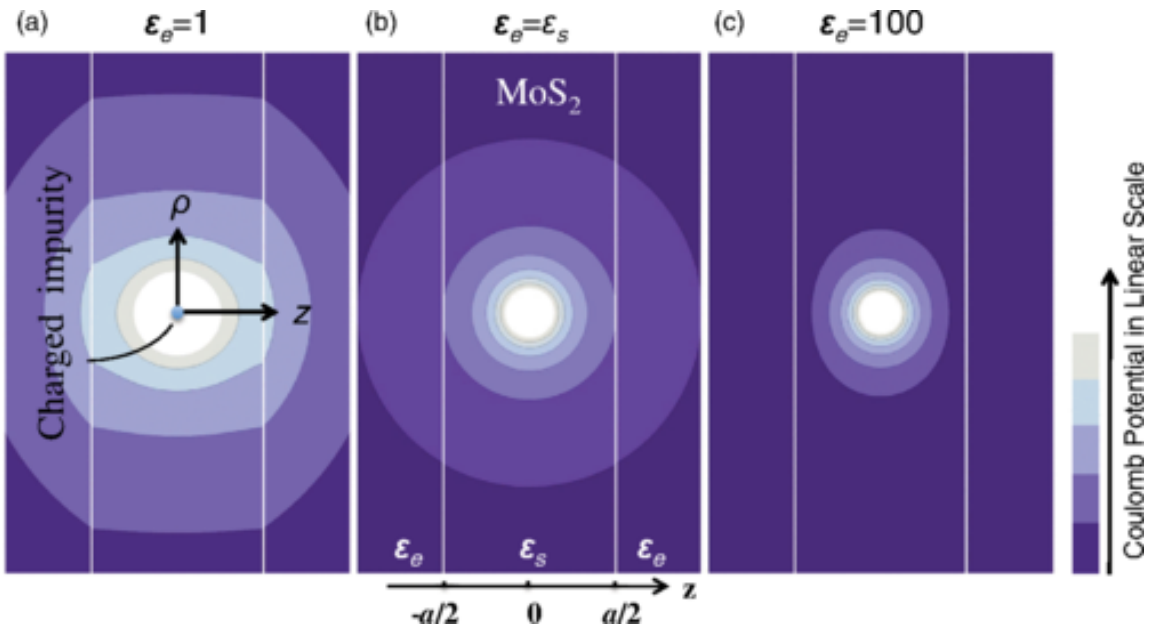

Figure 1.3: The effect of different dielectric mediums on the Coulomb potential of a point charge. Image reproduced with permission from [4]

The Coulomb scattering rate was observed to reduce by 20 times when the dielectric constant of the surrounding environment of a 1 nm thin film was changed from

1 to 100.[56] But if the surrounding dielectric supports polar vibrational modes, the charge carriers will experience scattering from the surface optical phonons of the dielectric.[4] Hence carriers in single layer MoS_2 experience enhanced carrier scattering when placed in close proximity to high dielectric materials that support low energy polar vibrational modes.[4, 51]

1.4 Applications of MoS_2

With a large bandgap, atomic thickness, and appreciable mobility values, MoS_2 finds applications in field effect transistors [57, 58], logic circuits [59], amplifiers [60, 61] and various advanced functional devices like flash memory[62]. The strong light-matter interactions in MoS_2 make them a suitable candidate for various optoelectronic applications. For instance, single layer MoS_2 phototransistor exhibited high photoresponsivity of 880 A/W and noise levels much lower than commercial state-of-the-art silicon avalanche photodiodes.[63] MoS_2 also exhibits strong electroluminescence, which makes them a good choice for light-emitting devices.[64, 65] The light absorption in a single layer of TMD, exceeds that of conventional semiconductors like silicon and GaAs by more than one order of magnitude. This makes them suitable for photovoltaic applications like solar cells.[66] Schottky junctions or p-n junctions based on TMDs are utilized in solar cells. A power conversion efficiency of 11.1 % has been achieved in a trilayer-graphene/MoS_2/n-Si-based solar cell.[67] Combining MoS_2 with other organics and perovskite materials in hybrid solar cells has also shown promising results.[68, 69, 70] The piezoelectric property of MoS_2 attributed to its broken inversion symmetry and piezoresistive effect due to the strain-induced bandgap change, makes them a potential choice for ultralow power piezoelectric transduction logic devices.[71, 72] The mechanical flexibility of MoS_2 combined with the excellent electrical and optical properties make them suitable

for flexible and wearable electronic devices.[73] Due to its porous morphology, the electrochemical performance of MoS_2 enables its application as electrode material in supercapacitors.[74] Their thermal properties finds potential in thermal nanodevices, such as on-chip power generators and nanosystems for waste thermal energy harvesting.[75, 76, 77] MoS_2 is also reported to have potential in various sensing applications like protein detection [78], label-free biosensors [79], gas sensing [80], and chemical sensing [81]. MoS_2 has also been stacked with various other 2D as well as different dimensional materials to form van der Waals heterostructures. The synergistic advantages of different materials paves the way towards observing interesting physics and improved device properties.[82, 83, 84] In this thesis, we will be discussing about field effect transistors and mixed dimensional van der Waals heterostructures based on MoS_2.

1.5 Field effect transistors

Finding ways to mitigate the short-channel effects and lower the power consumption associated with the downscaling of complementary metal-oxide semiconductor (CMOS) technology led to the search for materials beyond silicon. The subnanometre thickness, with the absence of dangling bonds and large bandgap makes semiconducting MoS_2 a suitable candidate. For a material to be considered suitable for logic device applications, it should possess a current ON/OFF ratio between $10^4 - 10^7$ and a bandgap exceeding 400 meV.[85] In 2011, FET based on monolayer MoS_2 (with a bandgap of 1.8 eV) using hafnium oxide as the gate dielectric exhibited a high mobility of 200 $cm^2V^{-1}s^{-1}$ at room temperature and an ON/OFF ratio of 10^8.[57] Further, in 2012, the first phototransistor based on single-layer MoS_2 was demonstrated with a shorter photoswitching time of 50 ms and a photoresponsivity of 7.5 mA/W, much higher than in graphene devices.[86] But often, the experimen-

tally observed mobility in MoS_2 is far lower than its theoretically predicted phonon limited value of 410 $cm^2V^{-1}s^{-1}$ at room temperature.[51] The experimentally observed low mobility values could be due to scattering from various extrinsic sources like Coulomb impurities (CIs) within the semiconductor or near the semiconductor-dielectric interface, or charge traps, and defects.[51] Several methods like using a high dielectric constant (ϵ) gate dielectric or encapsulating the device in a high ϵ environment or increasing the carrier density have been reported to screen the Coulomb impurities and suppress the carrier scattering. A mobility enhancement up to 150 $cm^2V^{-1}s^{-1}$ has been obtained in MoS_2 FET by using hafnium oxide as a back gate dielectric.[54] But high ϵ dielectrics can also contribute to additional scattering at room temperature due to the presence of polar surface optical phonons in the dielectric. The extent of scattering depends on the strength of dielectric coupling and the frequency of the surface optical phonons.[51] The effect is more prominent in dual-gated devices. Dielectrics like hafnium oxide have low-energy phonons, which can get easily populated at room temperature, whereas those like hBN have high-energy phonons. Hence at room temperature, scattering from hBN will be less compared to hafnium oxide.[51] Top gate FETs, owing to the improved dielectric screening and increased carrier density due to better electrostatics, have always shown superior performance over back gate FETs. But their deposition process can also add additional Coulomb impurities and traps. The performance of the FETs can also be affected by the high density of interface traps present at the semiconductor-dielectric interface. SiO_2 is the most commonly used dielectric and is known to have dangling bonds at the surface, which, in addition to scattering, also causes charge trapping detrapping resulting in large hysteresis and threshold instabilities.[55] This circumstance can be improved by coating the substrate or encapsulating the device with polymers like polymethyl methacrylate (PMMA) [87] or using a hBN substrate [88]. Atomic vacancies or point defects in MoS_2 can also contribute to short-range scattering resulting in constant mobility independent of temperature and carrier density.

Sulfur vacancies, which are one of the prominent point defects in MoS_2 has been treated using thiol chemistry and mobility enhancement up to 80 $cm^2V^{-1}s^{-1}$ has been achieved in a back-gated FET.[53] Apart from the above-mentioned factors, mobility in MoS_2 is underestimated due to the presence of contact resistance due to the formation of the Schottky barrier at the metal-semiconductor interface. Several methods like the use of low work function metals like scandium [89], metal alloys [90], semimetals as contact materials [91], making edge contacts [92], phase engineering and degenerate doping of 2D layers [93] and inserting inter layers between metal and 2D materials [94, 95] etc. has been adopted to lower the contact resistance and significant improvement in mobility has been observed. In addition to mobility and contact resistance, subthreshold swing and ON/OFF ratio are also essential metrics in deciding the FET performance.[96]

1.6 Mixed-dimensional van der Waals heterostructures

Heterostructures of different materials often exhibit properties distinct from their constituents. They offer the possibility of overcoming the limitation of the individual components and developing multifunctional devices. Conventional hetero structures confronted problems related to poorly defined and complex interfaces with the active junction buried deep within the sample.[84] But the advent of atomically thin 2D materials facilitated well-defined interfaces. The low permittivity and better electrostatic control of 2D materials allowed modulation of the interface properties using an applied gate voltage, providing an additional knob to tune the device properties.[84] In van der Waals heterostructures, the passivated interfaces, in the absence of any dangling bonds, interact through van der Waals forces. At such interfaces, charge transfer occurs through tunneling or hopping as opposed to orbital hybridization in

covalently bonded surfaces. Hence conventional concepts of band bending and formation of the depletion region, which are based on the carrier diffusion model, get redefined.[97, 98]

The recent progress attained in the wafer-scale synthesis of 2D materials with CMOS-compatible fabrication techniques is promising enough to integrate them with mature silicon semiconductor technology to produce cost-effective commercial devices for practical applications. MoS_2 with a direct bandgap, large optical absorption, and strong light-matter interaction when combined with silicon forms type II 2D-3D heterostructures. They have demonstrated promising applications in various optoelectronic devices like solar cells [66, 99], photodetectors [100], light emitting diodes [65], and in optical communications [101]. In 2014, solar cell fabricated using monolayer MoS_2 and silicon p-n junction demonstrated a power conversion efficiency (PCE) of 5.23 %.[66] At an optimal thickness of MoS_2 the PCE of Si/MoS_2 solar cell has been theoretically predicted to be as high as 24.76 %.[102] Research on MoS_2 based solar cells is still at the developmental stage and issues related to power conversion efficiency and stability have to be addressed in detail.[68] Photodetectors based on silicon and MoS_2 have shown noise equivalent power lower than the commercial silicon photodetectors and very high responsivity of 76.1 A/W.[103] The promising results shown by silicon-MoS_2 heterostructure are compelling enough to study this system further and understand the performance limiting factors and find ways to improve them.

1.7 Thesis outline

The thesis is organized into the following seven chapters.

Chapter 1 gives a brief introduction to two-dimensional materials and gives an overview of the properties and applications of MoS_2. The application of MoS_2 in

field effect transistors and in mixed dimensional van der Waals heterostructures is reviewed briefly. The influence of the surrounding dielectric environment on the properties of TMDs is also discussed.

Chapter 2 presents the major growth method used for synthesizing TMDs and various characterization techniques used in the thesis.

Chapter 3 explains how various growth parameters influence the chemical vapor deposition of TMDs and the important role of growth promoters in obtaining good coverage growth. The parameters were optimized for synthesizing monolayer MoS_2 with large area coverage.

Chapter 4 discusses a method of improving the field effect mobility of monolayer MoS_2 FET and investigates the effect of surrounding dielectric medium on their transport properties. The study resulted in a two-order enhancement in mobility and variation in the photoresponse relaxation time.

Chapter 5 foremost investigates various optoelectronic properties of monolayer MoS_2 - silicon mixed dimensional vdW heterostructure and further demonstrates a method of improving their photoresponse by modulating the surrounding dielectric environment. A nearly three-order enhancement in photoresponse was achieved by tuning the dielectric constant of the surrounding medium.

Chapter 6 examines the role of defects in the optoelectronic transport properties of silicon-MoS_2 heterostructure. The temperature-dependent studies revealed the profound influence of deep-level defects in limiting the photoresponse.

Chapter 7 concludes the thesis and presents the future directions.

Chapter 2

Experimental Techniques

This chapter discusses the major growth technique used for synthesizing TMDs and various characterization techniques used in this thesis.

2.1 Synthesis techniques

2D materials can be synthesized using various top-down or bottom-up synthesis techniques like mechanical exfoliation, liquid exfoliation, and several vapor phase techniques. Good quality 2D materials can be obtained, suitable for laboratory-scale studies using mechanical exfoliation, but cannot be produced at a larger scale.[104] Also, there is no control over the size, shape, and orientation of the resulting flakes. On the other hand, the liquid exfoliation technique has good scale-up capability with limitations in quality and flake size.[105] High-quality and large-scale 2D materials with good control can be synthesized using vapor phase techniques like Chemical Vapor deposition (CVD). Their growth parameters can be tuned to obtain the desired number of layers, orientation, size, morphology, and doping. These advantages, along with the reasonable cost of production, make CVD a very promising technique for the synthesis of 2D materials.[106]

2.1.1 Chemical Vapor Deposition(CVD)

Chemical Vapor deposition is a thermodynamic process in which one or more volatile precursors undergo a chemical reaction or decompose on the substrate surface and

forms a thin film. The process proceeds through several steps like- mass transport of the precursors in the gas phase, diffusion through the boundary layer, adsorption of precursors on the substrate, subsequent surface diffusion to the growth sites, chemical reaction at the surface to form a thin film, desorption of byproducts and transporting the byproducts out of the reaction chamber.[107]

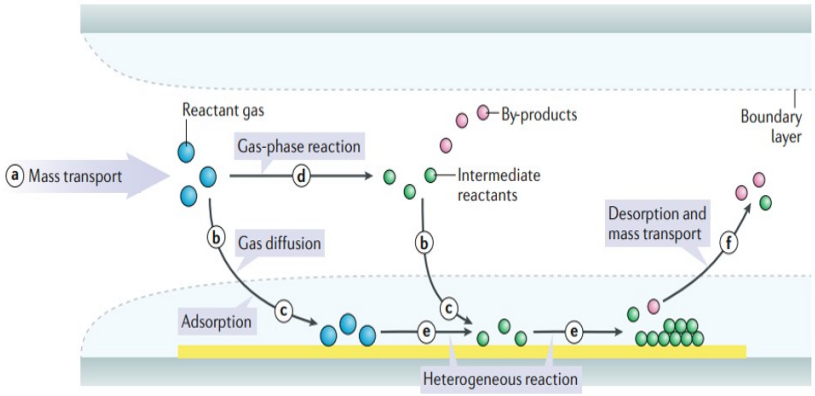

Figure 2.1: Various steps involved in chemical vapor deposition process. Image reproduced with permission from [5]

There are majorly three modes of epitaxial growth, namely, layer-by-layer mode (also called Frank–Van der Merwe growth), isolated islands mode (also called Volmer–Weber growth), and layer-plus-islands mode (also called Stranski–Krastanov growth). [108] In the layer-by-layer mode, the interaction between the substrate and the atoms in the film is much stronger, whereas, in the isolated mode, the interaction between the film atoms is stronger than that with the substrate. The layer-by-layer mode has a faster diffusion and results in a layer-by-layer film formation. The diffusion of atoms in isolated mode is rather slow and the atoms accumulate and coalesce on the substrate forming three-dimensional islands. The layer-plus-island mode combines both island and layer-by-layer growth mechanisms. Layer by layer is the most preferred growth mode for obtaining single crystalline large-area 2D materials.[109] The CVD growth of 2D TMDs progresses through multiple steps like- the vaporization of transition metal oxides, subsequent reduction to suboxides, the reaction between

the suboxides and reducing (chalcogen) vapors forming TMDs. Their properties like size, morphology, crystalline quality, phase, etc. can be controlled by optimizing various growth parameters like temperature, pressure, precursor, growth substrate, etc. The effect of some of the general parameters is explained below.

Temperature

Temperature determines the uniformity and composition of the 2D films. A slight change in temperature can cause large changes in the saturation pressure of the solid precursors in their vapor phase and affect growth. Temperature controls the reaction rate as it influences the mass transport of the reactant species and reaction at the substrate surface. With an increase in temperature, the proportion of precursor in the gas phase increases. Hence at higher temperatures, growth is limited by diffusion, whereas mass transport limits growth at lower temperatures.[106, 108]

Pressure

The pressure inside the reaction chamber influences the flow of the gas. Lower pressures give better control over the reaction because of the increased velocity of the reactant species and lower concentration of the precursor. Monolayer growth is favorable at lower pressure. Nucleation of the second layer occurs mostly at the grain boundaries at low pressures. In contrast, at higher pressures, nucleation occurs arbitrarily producing a combination of monolayer and multilayer growth.[106]

Precursor

Solid precursors like transition metal oxides, metal foil (for molybdenum and tungsten) and sulfur or selenium powders are used to synthesize TMDs. Since the vapor

pressure of solid precursors are sensitive to temperature, accurate control over temperature is crucial while using solid precursors.[110] Whereas gaseous precursors give better control over the number of reactant molecules, the purity of the precursor is crucial in deciding the sample quality. [111][106]

Substrate

The properties of the synthesized 2D material also depend on the microstructure and lattice structure of the substrate.[106] The commonly used substrates are Si/SiO_2[87], mica [112], saphire [113], $SrTiO_3$ [114] and polyimide.[115] TMDs also show certain orientation preferences depending on the crystal symmetry and surface terrace of the substrate.[106, 113, 116] Metals or metal foils like gold, tungsten foil, etc, have also been used as substrates. Crystallography of gold chosen by selecting different facets dictates the nucleation and domain size of TMDs.[117] The substrate orientation influences the morphology of the film.[118] To promote nucleation and the growth of TMDs, substrates are treated with several growth promoters or seeding layers.[119] They react with the high melting point precursors and form volatile intermediates.[120, 121]

The CVD synthesis carried out in this thesis was done in a home-built atmospheric pressure CVD setup. The system consists of a quartz tube placed inside a furnace, whose inlet is connected to a mass flow controller (MFC) and outlet to a series of bubblers. Argon and Nitrogen was used as the carrier gas whose flow rate was controlled by the MFC. The volatile byproducts were removed through the exit. The precursors and substrates were placed inside the quartz tube on a ceramic boat. Further details of the growth parameters are discussed in Chapter 3.

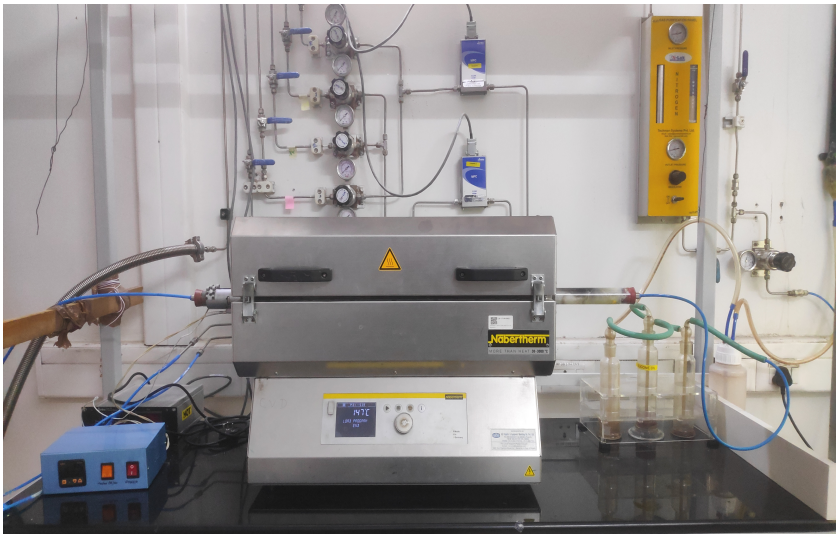

Figure 2.2: Home built CVD set up used for synthesis

2.2 Spectroscopic Techniques

2.2.1 Raman Spectroscopy

Raman spectroscopy is a rapid, powerful, and non-destructive characterization tool to study the electronic and vibrational states of materials. This technique utilizes the principle of Raman scattering, discovered by Sir C.V Raman in 1928, and for which he was awarded the Nobel Prize for Physics in 1930.[122] When light is incident on a substance, it gets either absorbed, reflected, or scattered.[123] If the scattered and the incident light has the same frequency, no energy transfer occurs and results in an elastic collision process called Rayleigh scattering. This is usually very strong. The remaining light is weakly scattered with frequencies different from the incident light through a process known as Raman scattering. A higher scattered frequency results in Antistokes scattering and lower in Stokes scattering. There is energy transfer involved in this inelastic scattering and gives information about the vibrational modes of the system. The intensity of the scattered light is proportional

to the number of scattering molecules. At room temperature in thermal equilibrium, maximum molecules occupy the ground (lowest energy level) state. Hence Stokes scattering is more intense than Antistokes scattering making the Raman scattered light mostly Stokes scattered.[122]

Raman spectroscopy is widely used in 2D materials to get information about their vibrational properties, layer number, disorders, doping, and strain-induced. [124] With a unit cell containing two molybdenum and four sulfur atoms, bulk 2H MoS_2 belongs to the space group D_{6h}^4 ($P6_3/mmc$).[125]On the other hand, the space group in monolayer and few-layer samples is determined by the parity of the number of layers, due to the lack of translational symmetry along the c-axis. Samples with an even number of layers preserve the inversion symmetry and belong to the space group D_{3d} whereas those with odd number of layers lack a centre of inversion and belongs to D_{3h} symmetry.[126] Bulk 2H MoS_2 with 6 atoms in the unit cell and 18 possible vibrations, can be represented using the following irreducible representation at the Brillouin zone center (Γ point), [125]

$$\Gamma_{2H} = A_{1g} \bigoplus 2A_{2u} \bigoplus 2B_{2g} \bigoplus B_{1u} \bigoplus E_{1g} \bigoplus 2E_{1u} \bigoplus 2E_{2g} \bigoplus E_{2u} \tag{2.1}$$

where A_{1g}, E_{1g} and $2E_{2g}$ are the Raman active modes, A_{2u} and E_{1u} are infrared active acoustic modes and B_{2g}, B_{1u} and E_{2u} are inactive phonon modes.[127] Here, A_{1g} represents the out-of-plane relative motion of sulfur atoms, E_{1g} to the in-plane relative vibration of sulfur atoms, E_{2g} to the in-plane opposing motion of molybdenum and sulfur atoms and B_{2g} corresponds to the out-of-plane vibration of molybdenum and sulfur atomic planes relative to each other.

But for monolayers with one molybdenum and 2 sulfur atoms in the unit cell, and a 3-fold rotational axis is represented as [125]

$$\Gamma_{monolayer} = {A_1}' \bigoplus E" \bigoplus 2{A_2}" \bigoplus 2E' \tag{2.2}$$

(since odd and even numbers of layers have different symmetries, the representation of various modes is also different. But in the later chapters of the thesis, we have used the bulk representation for monolayers also out of convenience.)

Monolayers of MoS_2 are usually characterised by the peaks $E^{'}$ at ~ 385 cm^{-1}(${E_{2g}}^1$ in bulk) and ${A_1}^{'}$ at ~ 403 cm^{-1} (A_{1g} in bulk). $E^{'}$ denotes the in-plane vibrations of molybdenum and sulfur atoms, whereas ${A_1}^{'}$ the out-of-plane vibrations of the sulfur atoms. The difference in frequency between these modes increases with the number of layers and is considered as an indicator of the number of layers.[125] The inter-layer van der Waals forces increase with the number of layers suppressing the atomic vibrations and resulting in larger force constants. The out-of-plane vibrations get affected and produce a blue shift in the ${A_1}^{'}$ mode. On the contrary $E^{'}$ mode red shifts with increase in layer number. This is due to increased long-range Coulombic inter-layer interactions or the stacking-induced structural changes.[124] Upto 4 layers can be identified using this method, beyond which the modes converge to the bulk values.[124] Full width at half maximum (FWHM) of both the modes increases with decreasing thickness.[127] Apart from the above-mentioned high-frequency modes, the relative vibrations between the layers result in shear (in-plane) and breathing (out of plane) modes in the low-frequency range (< 50 cm^{-1}).[125]

Raman spectroscopy is a very sensitive tool and hence factors like temperature, strain, doping, and disorder can influence the spectra. For example, on the application of a uniaxial strain, due to the isotropic in-plane symmetry breaking, the $E^{'}$ peak splits into two and redshifts with increasing strain. But ${A_1}^{'}$ peak is unaffected by tensile strain. Whereas both $E^{'}$ and ${A_1}^{'}$ modes redshifts when a biaxial strain is applied.[127] Both these modes are reported to linearly blueshift with a decrease in temperature. This shift is attributed to the lattice expansion caused by the anharmonicity of the interatomic potential.[75] Similarly, an increase in laser power also softens both the modes due to heating induced by the laser.[75] Doping also

significantly influence the Raman spectrum of MoS_2. The frequency of $A_1{}'$ mode was observed to decrease, intensity decrease and its linewidth increase with increase in n type doping [128] whereas p doping results in a blue shift and increase in intensity for the $A_1{}'$ mode.[129] In both the cases, the position and linewidth of E' mode was found insensitive to doping. This is because of the stronger electron phonon coupling experienced by $A_1{}'$ mode over E' mode.[128] The presence of disorder also broadens both the peaks and results in a decrease in frequency of E' and increase in frequency of $A_1{}'$ peaks. Several defect-induced peaks appeared, of which the intensity of LA (M) peak ~ 227 cm^{-1} signaled a proportionality to the level of defects in the system.[130]

In our study, Raman spectroscopy was performed using a 532 nm Continous Wave diode laser and a 100 x objective with 0.95 NA in the backscattered configuration. Grating with 1800 lines/mm was used to disperse the Raman signal.

2.2.2 Photoluminiscence Spectroscopy

Photoluminescence spectroscopy, often referred to as PL, is a non-contact, fast and non-invasive tool to probe materials. PL involves the excitation of a material with laser light of energy larger than the bandgap of the sample and recording the resulting luminescence as a function of the wavelength and intensity of emitted light. The absorption of photons from the laser creates electrons and holes in the conduction and valence band. The energy and momentum of the excited electrons and holes relax and move towards the conduction and valence band minima, leading to eventual recombination and emission of photons.[131] PL spectroscopy has been used in semiconductors to determine the bandgap, impurity levels, concentration of defects, material quality, recombination mechanisms, etc.[132]

Bulk MoS_2 exhibits negligible photoluminescence, whereas it is strongest in mono-

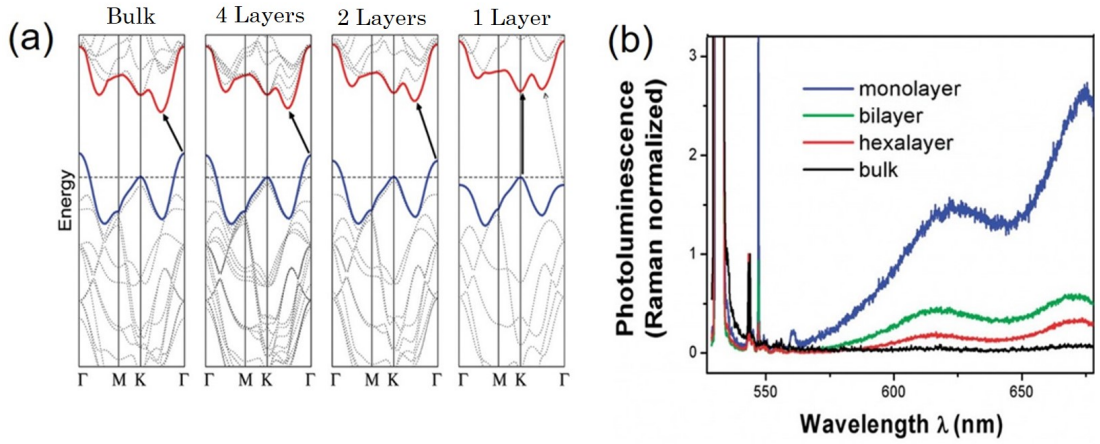

Figure 2.3: (a) Band structures evolution of MoS_2 at various number of layers (b) Photoluminescence spectra MoS_2 layers with different thickness. Images reproduced with permission from [6], Copyright © 2010 American Chemical Society

layers. The PL efficiency of a free-standing monolayer is more than 10^4 times compared to its bulk.[18] This difference is associated with the nature of bandgap- direct in monolayer and indirect in bulk MoS_2.[18, 6] These interesting optical properties can be attributed to the d orbitals of molybdenum atoms that dominate the valence and conduction bands.[133] The indirect bandgap in bulk MoS_2 originates from the transition between the top of the valence band at the Γ point and the bottom of the conduction band, located halfway between the Γ and K point. The direct bandgap is positioned at the K point. The conduction band states at the K point are composed of molybdenum d orbitals. As the Molybdenum atoms are positioned within the layer, these states are unaffected by the interlayer interactions. In comparison, the electronic states at the Γ point and the point of indirect bandgap are composed of a linear combination of d-orbitals of the molybdenum atoms and anti-bonding p_z orbitals of sulfur atoms and are influenced by the strong interlayer coupling. Hence with the increase in layer thickness, the direct excitonic transition at the K point of the Brillouin zone remains unchanged, but due to the increased interlayer coupling, the indirect bandgap energy decreases.[18] Due to the large atomic number of molybdenum atoms, the band structure at the K point is further modified due to the

strong spin-orbit interactions causing a valence band splitting. Hence for monolayer MoS_2, this results in two direct excitonic transitions at 1.85 eV and 1.98 eV corresponding to A1 and B1 excitons, respectively.[18] The PL spectra of TMDs can give information about strain, doping, exciton and trion binding energies, and defects and depends sensitively on temperature. In monolayer TMDs, the strong dependence of PL on the intensity of the excitation laser has resulted in the observation of exciton-exciton collisions and multiexciton formations.[134] Hence PL spectroscopy is a valuable tool for extracting a good deal of information about TMD systems.

Photoluminescence in our experiment was measured using a 532 nm Continous Wave diode laser. A 100 x lens with 0.95 NA (numerical aperture) was used in the backscattering configuration for excitation and collection. 300 lines/mm grating was used to disperse the PL signal.

2.3 Microscopic Techniques

2.3.1 Atomic Force Microscopy

Atomic Force Microscope (AFM) was invented in 1985 by Binnig, Quate, and Gerber.[135] It is a category of scanning probe microscopy in which a topographical image of a sample surface can be obtained by raster scanning a sharp tip attached to a flexible cantilever.[136] As the tip interacts with the surface, depending on the atomic force variations, the tip gets deflected. The extent of deflection is measured by focussing a laser beam onto the backside of the tip coated with a reflective material. The reflected laser beam then falls onto a photodetector, whose position is used in a feedback loop to monitor the surface. AFM can be used in either contact mode or tapping mode.[136] The versatility of this surface imaging technique lies

in its atomic resolution and 3D topographic imaging capability. With the development of advanced novel AFM modes, information about various quantities like surface potential, conductivity, adhesion, modulus, permittivity, absorption, reflection etc.[137, 138] can also be obtained. AFM can also be operated at ambient and in controlled environments like in liquids, at various temperatures etc.[136] The thickness of TMDs can be measured using AFM, which can be used along with Raman and PL spectroscopy to identify the number of layers.[6, 139] In this thesis, AFM measurements were performed using Keysight 5500 AFM.

2.3.2 Scanning Electron Microscopy

Scanning electron microscope (SEM) use electron beams to image sample surfaces with nanometre scale resolution. [140] Electrons emitted from an electron gun are collimated into a beam and then focussed onto a spot using electromagnetic fields and lenses. When high-energy electrons impinge the sample surface, several signals like backscattered electrons, secondary electrons, Auger electrons, and X-rays are generated. Backscattered electrons (BSE) are elastically scattered incident electrons generated from the surface which can give information about the sample's composition with lower-resolution images. Secondary electrons (SE) produce inelastic interactions with energy lower than the backscattered electrons and give topographic information of the sample. BSE originates from a few micrometers below the sample surface, whereas SE originates from the surface region within a few nanometers. Information about the sample's elemental composition can be obtained from the X-Rays. The resolution of SEM images can be improved by replacing the electron source with a field emission gun that produces extremely focused high and low-energy electron beams. This system, known as field emission scanning electron microscope (FESEM), has in lens detectors and works with low acceleration potential, which minimizes the charging effect on insulating samples.[141]

In this thesis, the FESEM images were taken with a Zeiss Ultra Plus field emission scanning electron microscope (FESEM) equipped with an integral charge compensator and embedded EsB and AsB detectors (Oxford X-max Instruments 80 mm^2 (Carl Zeiss NTS, GmbH)).

2.3.3 Transmission Electron Microscopy

In Transmission electron microscopy (TEM), the interactions between an electron beam and atoms, when passed through a thin sample, give the sample's image under examination. Electrons with 100,000 times shorter wavelengths than visible light can resolve features as low as 0.05nm. TEM can be used either in image mode or diffraction mode.[142] Image mode gives information about the microstructure and diffraction mode about the crystalline structure of the sample. The electrons passing through the sample can either get transmitted without any interaction or get diffracted depending on the interaction. These electrons are collected by detectors placed at various angles. Larger the atomic number, the more the number of scattered electrons. Bright-field (BF) captures the least scattered electrons whereas High angle annular dark field (HAADF) detector collects electrons scattered at larger angles. HAADF image is also known as Z contrast image, as the image contrast is directly related to changes in thickness or mass. TEM has two principal modes of operation-parallel and converging beam mode. In parallel beam mode, broad and parallel beams illuminating the sample produce high-resolution TEM (HRTEM) images, whereas, in converging mode, small converging beams scan across the sample, recording scanning TEM (STEM) images.[143] TEM also has disadvantages like knock-on damage and distortion of the image due to aberrations. But the advancement of aberration-corrected TEM, with lower acceleration voltages, has solved these problems.[144] TEM is extensively used to characterize 2D materials. The potential of atomic resolution imaging with a wealth of information about the crystalline

structure, presence of atomic defects, grain boundary, interstitial sites, etc, makes it very useful analysis tool. [144]

In this thesis, high-resolution transmission electron microscope JEOL JEM 2200FS, Japan equipped with a 200 KeV field emission gun (FEG) and in-column energy filter (Omega filter) was used.

2.4 Low-frequency noise spectroscopy

Any undesirable signal produced by the fluctuation in current or voltage that interferes with the actual signal and distorts the desired signal is considered as noise. The source of noise can be either extrinsic or intrinsic. External noise can be controlled using proper filter circuits or shielding, grounding, etc. But intrinsic noise is generated within the system and hence a detailed understanding is needed to minimize them. Though noise has a detrimental effect on the device performance and should be controlled, it can also give useful information about defects, interface quality, material condition, etc. of the system. Noise analysis finds application in various fields, including telecommunication, nanoelectronics, mesoscopic structures and biological systems.

In condensed matter, fluctuations or the noise produced from a physical system can give useful information about the associated physical phenomenon. [145] Thermal noise, shot noise, generation recombination noise, and $1/f$ noise are the four important types of intrinsic electronic noise present in semiconductors. A thermal noise, otherwise known as Johnson noise originates from the thermal fluctuations of electrons in a conductor and depends on the temperature. Shot noise arises due to the discrete nature of electrons and is proportional to the current passing through the conductor. Both thermal and shot noise are white noises with no dependence

on frequency. Generation recombination noise is associated with fluctuations in the number of carriers due to the generation, recombination, or trapping of carriers.[146] It is usually observed at low frequency and its spectral density is described by a Lorentzian function given by

$$S_I(f) = \frac{S_0}{1 + (2\pi f\tau)^2} \tag{2.3}$$

where S_0 is the frequency independent portion observed at frequency less than $(2\pi\tau)^{-1}$ and τ is the time constant of a specific trapping.[147] Fluctuations in conductance with a power spectral density proportional (PSD) to $1/f^{\alpha}$ with $\alpha = 1 \pm 0.1$ constitutes $1/\ f$ noise. The PSD of $1/\ f$ can be written as

$$S_I = \frac{AI^{\beta}}{f^{\alpha}} \tag{2.4}$$

where A is the noise amplitude. For an equilibrium phenomenon, the value of exponent $\beta = 2$ suggests that fluctuations in current are due to the resistance fluctuations and not due to the variations in applied current.[148] These types of noises are usually observed at lower frequencies 1 Hz to 10 kHz.[146] Electrical current, expressed as $I \propto qN\mu$, depends on the number (N) and mobility (μ) of the charge carriers. Hence fluctuation in current can be due to either a mobility fluctuation or a carrier number fluctuation or both.[147] Here we discuss the two different models used to describe the $1/\ f$ noise.

2.4.1 Hooge Model

Hooge, in 1969 proposed that the flicker noise in homogeneous bulk systems is due to mobility fluctuations based on Hooge's empirical relation [146]

$$\frac{S_I}{I^2} = \frac{\alpha_h}{fN} \tag{2.5}$$

and

$$N = \frac{C_{ox}(V_g - V_{th})W_{ch}L_{ch}}{q} \tag{2.6}$$

α_H is the dimensionless parameter called Hooge's parameter which gives a relative measure of noise in a sample, N is the total number of carriers, C_{ox} is the gate oxide capacitance per area, V_g is the gate voltage, V_{th} is the threshold voltage, W_{ch} and L_{ch} are the width and length of the channel. Initially, α_H was proposed to have a constant value of 2×10^{-3}. But later, it was observed that the value of α depends on the quality of the sample and on various scattering mechanisms that determine mobility.[146] Major scattering mechanisms influencing the mobility of a semiconductor are scattering from the lattice and impurities. Hence using the Matheisens rule, measured mobility can be written as

$$\frac{1}{\mu_{measured}} = \frac{1}{\mu_{lattice}} + \frac{1}{\mu_{impurity}} \tag{2.7}$$

Hooge and Vandamme in 1978, experimentally observed that lattice scattering generates 1/f noise with no appreciable contribution from impurity scattering.[149] As impurities have limited influence on mobility fluctuations, this model is more suitable to clean and homogeneous metals and semiconductors.[150]

2.4.2 McWhorter model

This model is named after McWhorter, who in 1957, proposed the origin of $1/f$ noise to the carrier number fluctuation in the channel. This model was introduced to explain the $1/f$ noise in silicon MOSFET, where the slow trapping and de-trapping of charge carriers at the channel and dielectric interface could explain the magnitude and spectral shape of the observed noise.[150] The model assumes the low-frequency noise to have a surface origin.[151] Each trapping/de-trapping event is described as a quantum tunneling between the charge and trap state. The characteristic relaxation

time constant τ for a specific trapping event, is given by

$$\tau = \tau_0 e^{\gamma x} \tag{2.8}$$

where τ_0 is a microscopic time scale of the order of the phonon frequency, γ is the attenuation coefficient in the oxide and x is the distance from the oxide. A single trapping/de-trapping produces a generation recombination noise with a Lorentzian spectrum. But when there is a spatial distribution of trap states, the superposition of all Lorentzian spectra gives rise to a $1/f$ spectrum.

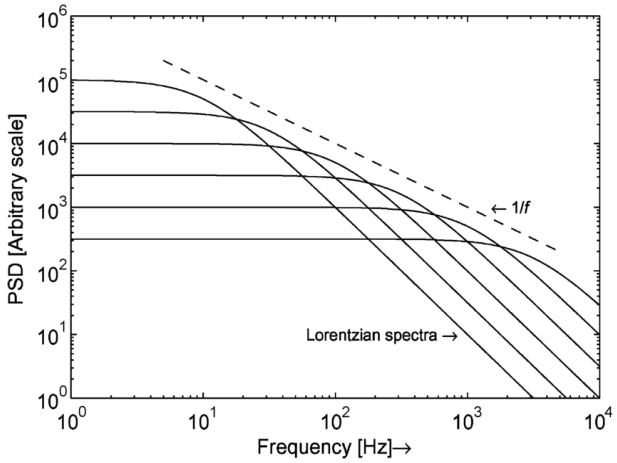

Figure 2.4: Superposition of different Lorentzians forming a $1/f$ spectrum. Image reproduced with permission, from [7] Copyright © 2007, IEEE

In most condensed matter systems, low-frequency noise arises due to the relaxation of defects, each of them with a finite relaxation time. Hence, low frequency noise is a very sensitive tool that possesses information about the fundamental statistics of defects and the associated relaxation phenomenon contributing to the noise.[145] The level of low-frequency noise present determines the sensitivity of amplifiers and transducers used in various sensors. The level of 1/f noise also affects the phase noise of oscillating systems used in various high-frequency communication applications.[147]

In this thesis, for measuring low-frequency noise, a DC bias was applied across the sample using a battery. The current fluctuations were recorded using a low noise current preamplifier (Stanford Research SR 570) and the sampling of the output was done by National Instruments Digital Acquisition (DAQ) card. From the acquired data, FFT analysis and the power spectral density were recorded using the lab view software.

2.5 Device fabrication

To perform the electrical characterization and study the transport properties of 2D materials, devices were fabricated by depositing contact materials on them after patterning the desired regions using photolithography.

2.5.1 Photolithography

Photolithography is a technique that uses light to transfer a desired pattern onto a substrate. A light-sensitive material called photoresist is coated on the substrate, which after light exposure, undergoes a chemical reaction and becomes soluble in a developing solution.[152] There are two types of photoresists-positive and negative. In positive photoresists, the light-exposed regions are soluble and hence get removed after developing, whereas in negative photoresists the process reverses. The exposed regions become insoluble and the remaining portion gets removed. Hence when using a positive photoresist, the pattern same as the mask, and for a negative photoresist, the reverse pattern as that of the mask is formed on the substrate. In optical lithography, light can be exposed in two different methods namely shadow printing and projection printing. In shadow printing either the mask is in direct contact with the substrate or in close proximity. A high resolution of $\sim 1\mu m$ can be obtained in

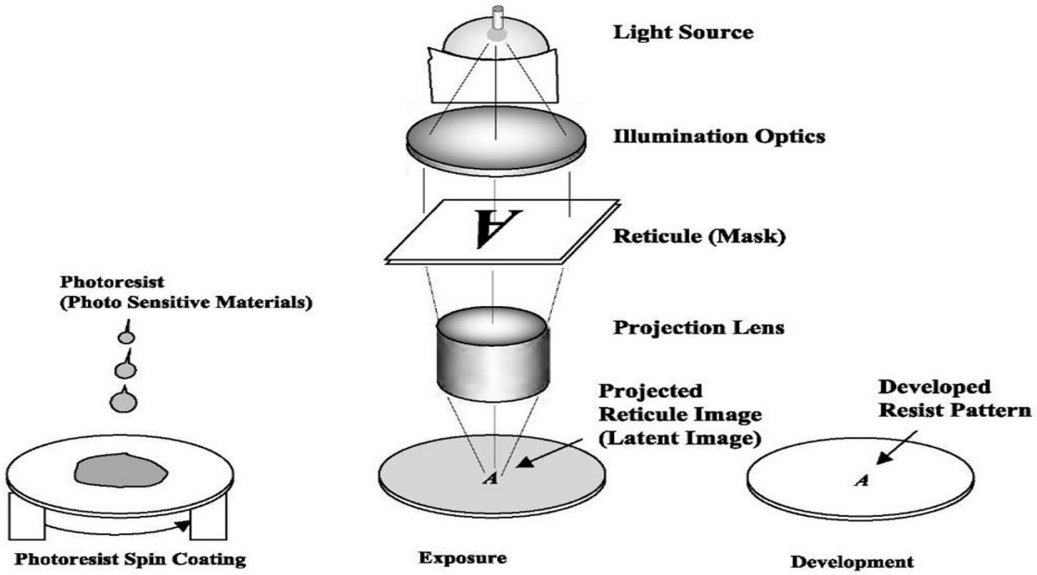

Figure 2.5: Schematic of projection lithography. Image reproduced with permission from[8]

shadow printing but can encounter problems due to the presence of dust particles in the mask or defects in the substrate. We use the method of projection printing for all device fabrications carried out in this thesis. In projection printing, the pattern on the mask is projected onto a substrate kept centimeters far away from the mask. The minimum line width (W) of the pattern formed on the substrate is given by

$$W = \frac{\lambda}{NA} \tag{2.9}$$

where λ is the wavelength of light used and NA is the numerical aperture given by [152] $NA = nsin\theta$, where n is the refractive index of the imaging medium (air) and θ is the half angle of the cone of light converging to a point image at the substrate.[153] The depth of focus (DOF), an important factor in projection printing, which is a measure of the displacement of the image plane upto which a sharp feature size can be retained, is given by

$$DOF \propto \frac{\lambda}{NA^2} \tag{2.10}$$

An optimum value of NA should be chosen to have a higher resolution and a larger depth of focus.

2.5.2 Thermal Evaporation

Thermal evaporation is a Physical vapor deposition (PVD) technique used for depositing thin films of various materials onto a surface. The material to be deposited is heated to its melting point, which is placed in a resistive coil (or metal plate). The evaporated material then gets condensed onto the target surface. The resistive coil is usually made with high melting point materials like tungsten and is heated by passing a direct current through it. The entire process is carried out in a high vacuum to prevent the collision of the evaporated material with gas molecules. This method is suitable for depositing materials with low melting points.[154] In this thesis, Gold was deposited as the contact material, along with Chromium as an adhesion layer.

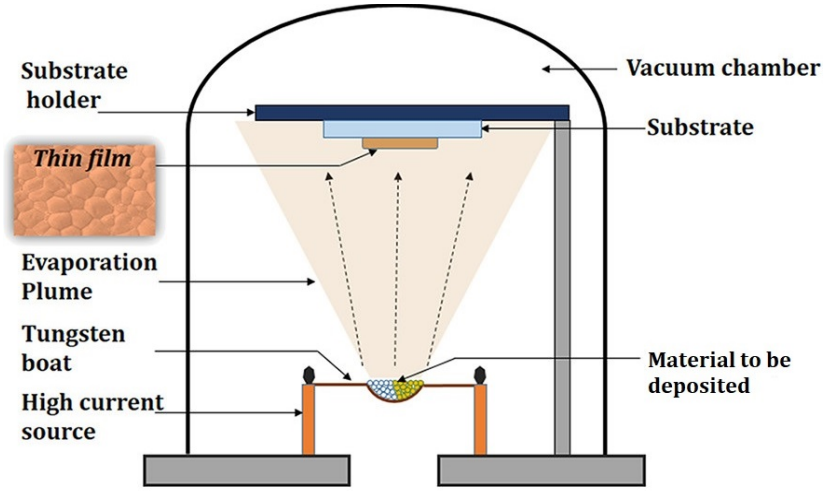

Figure 2.6: Schematic of the thermal evaporation system. Image reproduced with permission from [9] Copyright © 2021, American Chemical Society

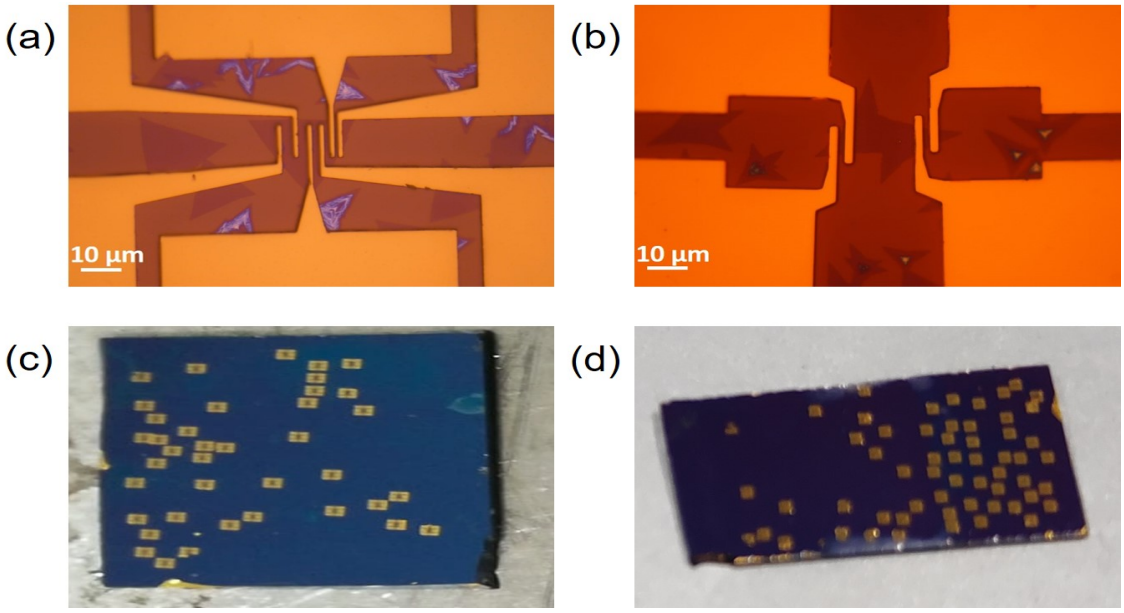

Figure 2.7: (a) and (b) Different patterns of devices fabricated, (c) and (d) Multiple devices fabricated on a substrate

2.5.3 Etching Processes

Etching is a process of removing material from a substrate. Depending on the etchant phase, there can be wet or dry etching.[155] The reaction products are soluble in wet etching and volatile in dry etching. Wet etching is highly isotropic and can affect the resolution of the required pattern. However, dry etching is mostly anisotropic and directional. Hydrofluoric acid (HF) together with ammonium fluoride (NH_4F) forms a wet etchant to remove SiO_2 whereas hydrofluoric acid (HF) with nitric acid (HNO_3) is used to etch silicon.[10] Plasma etching and Reactive ion etching are the two major types of dry etching.[156]

Reactive Ion etching

Reactive ion etching (RIE) is a plasma process used to remove material from a substrate surface using a combination of physical and chemical reactions. It is a

highly anisotropic process in which highly energetic ions bombard the substrate surface. RIE chamber has a parallel plate arrangement in which a capacitively coupled source (CCP) generates both plasma and DC voltage. Radiofrequency (13.6 MHz) power is used to generate plasma (ions) and a negative bias is applied to a substrate placed on a powered electrode. The negative bias enhances the acceleration of ions and surface bombardment. Along with ion bombardment, a radical substrate reaction also takes place. A volatile product is formed when the radical bonds with the substrate, which is then removed by the vacuum pump.[155] RIE process is carried out at low pressures.

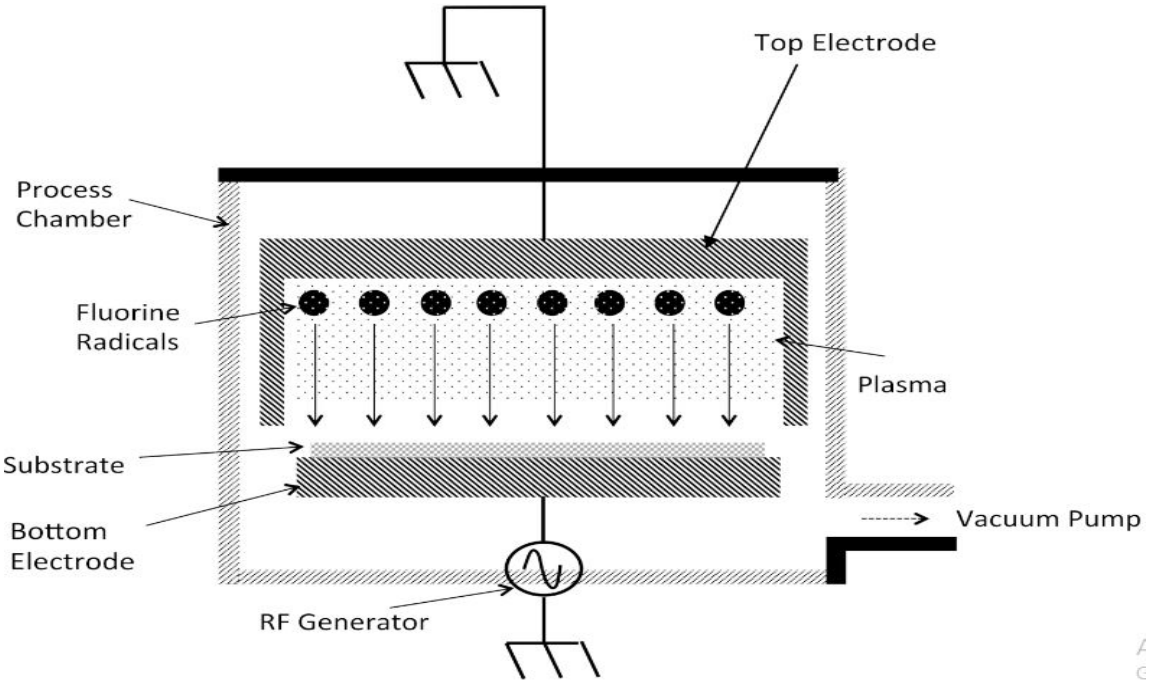

Figure 2.8: Schematic of the Reactive Ion Etching system. Image reproduced with permission from [10]

Various patterns can be etched by selectively protecting the desired areas by using an etch mask. Photoresist is a common etch mask. Other materials used as etch masks include silicon dioxide (SiO_2), silicon nitride (Si_3N_4), and metals, such as aluminum (Al) or chromium (Cr).[10] Selectivity, etch rate, sidewall profile, and

aspect ratio are the important features of etching. A higher selectivity is essential to prevent the etching of etch mask and remove the protected areas. RIE generally has high selectivity. Good etching requires a large number of low-energy ions and low pressure, But this results in a low etching rate, in the trade-off of good selectivity, uniformity, and etch profile.[155]

In this thesis, we have used both wet and dry etching to remove SiO_2 to pattern silicon substrate for making silicon- MoS_2 heterostructure. Buffered oxide etchant (BOE) and HF was used as wet etchants. For RIE, SF_6 and oxygen was used in the 4:1 ratio at 120 Watt RF power. The entire process was carried out in a home-built RIE chamber.

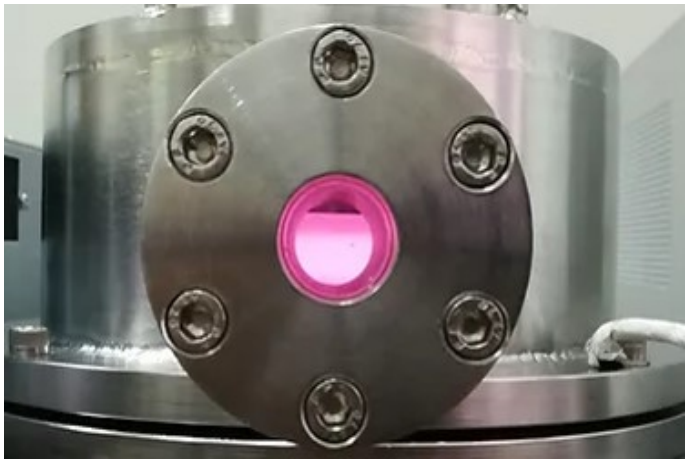

Figure 2.9: Home-built reactive ion etching setup used for dry etching.

Chapter 3

Synthesis of 2D Transition Metal Dichalcogenides

This chapter is an adaptation of the research article published in "Materials Research Express, 6 (12), 125002, 2019".

3.1 Introduction

The isolation of a single layer of graphene [157] by mechanical exfoliation using scotch tape in 2004 by Geim and Novoselov opened a plethora of new possibilities. Further research on graphene [158] laid a path for the exploration of various other 2D materials like TMDs, hexagonal boron nitride, phosphorene, silicene, germanene etc.[28, 159, 160, 161, 162] TMDs usually represented as MX_2, where M is a group IVB, VB, VIB, VIIB transition metal and X a chalcogen (S, Se, Te) are a class of layered materials which are held together by weak van der Waals force with strong in-plane covalent bonds. Different TMDs exhibit insulating (HfS_2) [163] , metallic (NbS_2, VSe_2) [163] , semi-metallic (WTe_2,TeS_2) [163], semiconducting (MoS_2)[164] and superconducting (TaS_2) [164, 165] behaviour. TMDs find numerous applications including in field effect transistors [166, 88], photovoltaic solar cells [167, 168, 66], photodiodes [167, 169], photodetectors [170], light emitting diode [167], sensors [171] ,memristors.[172]

Among various TMDs, MoS_2 is one of the most widely researched materials. MoS_2 exhibits an indirect (1.29 eV) to direct (1.9 eV) bandgap transition with en-

hanced photoluminescence efficiency (more than a factor of 10^4 compared to bulk) when the thickness is reduced to a monolayer.[18] Bandgap changes with the number of layers and lies in the visible region. At excitonic resonances, single layer MoS_2 can absorb upto 10 % of the incident photons.[173] Field effect transistors based on MoS_2 have exhibited mobility upto 200 $cm^2V^{-1}s^{-1}$ with 10^8 current on/off ratio.[57] Large mechanical strength, tunable bandgap [18], lack of dangling bonds, and thermal stability upto 1100 °C [57] makes it attractive for electronic and optoelectronic applications. MoS_2 also finds applications in valleytronics and spintronics due to the broken inversion symmetry, which results in two inequivalent valleys in its band structure.[174]

MoS_2 can be synthesised by mechanical exfoliation [175], liquid exfoliation [176], chemical exfoliation [177, 178], chemical vapour deposition (CVD) [179, 180, 181], molecular beam epitaxy (MBE) [182], atomic layer deposition (ALD) [183], physical vapour deposition (PVD).[184] Among different synthesis methods, CVD offers the advantage of wafer-scale coverage, low cost, and direct synthesis over various substrates with large grain-size films.[48] Another advantage is that by choosing a suitable condition, it is possible to grow lateral heterostructure with an atomically sharp interface between MoS_2-$MoSe_2$, WS_2-WSe_2 [185],WS_2-MoS_2 [82], WSe_2-MoS_2 [186]. Much research is being carried out in CVD grown MoS_2 with reported several millimeters to centimeter-scale coverage over the substrate. [179, 187, 188] Sulfur and various molybdenum containing materials such as MoO_3 powder [179], evaporated molybdenum thin films [189], $MoCl_5$ [190],$(NH_4)_2MoS_4$ [191] are used as the precursor for the chemical vapor deposition of MoS_2.

One of the main challenges in CVD is to get reproducible results from batch-to-batch growth. Even on the same batch, depending on the position of the substrate, the growth can be different. This is mainly due to the poor control over the vaporization and amount of precursor reaching the substrates during the reaction, which

are crucial in deciding the morphology of the resultant film.[188] Apart from the substrate surface treatment, reproducible 2D materials growth using CVD depends critically on various growth parameters such as carrier gas flow rate, reaction temperature, position of the substrate, reaction time, distance between the precursors and substrate.[192, 106] In this chapter, we have studied in detail the effect of the flow rate of the carrier gas, position of substrate, temperature and the role of growth promoter in the synthesis of MoS_2 monolayer using a home built atmospheric pressure CVD. We were successful in growing continuous monolayer of MoS_2 over the entire substrate (cm^2 area) with repeatable results under the same growth conditions.

3.2 Experimental details

The general procedure used for the study is as follows. MoO_3 powder was placed in an alumina boat at the center of the furnace in a quartz tube with sulfur powder in another boat upstream at a fixed distance away from the MoO_3 boat. 300 nm SiO_2 coated silicon wafers ultrasonically cleaned (in acetone and IPA) and oxygen plasma treated were used as the substrates and were placed downstream on a separate boat facing up away from the MoO_3 boat. The substrates were coated with a drop of NaCl solution to promote growth. The furnace temperature was ramped to the desired temperature at the rate of 5 ℃ min^{-1} and remained at that temperature for 20 minute and allowed to cool down gradually. Argon/Nitrogen was used as the carrier gas. Various growth conditions were varied depending on the study.

3.3 Results and discussions

3.3.1 Effect of growth promoter (NaCl)

Several approaches to enhance the growth and coverage of monolayer TMDs, like using aromatic seeding promoters,[179] alkali halides.[120, 193, 194] and patterned substrates [195] have been studied previously. All these methods help in lowering the nucleation energy barrier. Studies reveal that sodium in NaCl assist in the growth [196] and can easily be removed during the transfer process. A two order increase in the lateral dimension of single crystalline MoS_2 was observed in the presence of alkali halide (NaCl or KI).[197] We have systematically studied the need and role of a growth promoter like NaCl (commonly known as salt)in continuous layer formation. The advantage of using NaCl as a seeding layer is its ease of deposition, easy availability, and the resulting continuous coverage over the entire substrate with minimal quantity. We first aimed to optimize and understand the role of the growth promoter in enhancing the coverage of the monolayer and its impact on the optical and electrical properties of the as-grown film (without transferring it to a different substrate).

50 mg MoO_3 and 500 mg sulfur separated by a distance of 18 cm were used as the precursors and was placed in a 4 cm inner diameter quartz tube. 60 sccm nitrogen was used as the carrier gas. The substrates were placed on a separate boat facing up 5 cm away from the edge of the MoO_3 boat downstream. The reaction temperature was set to 750 ℃ for a duration of 20 minutes.

When the synthesis was carried out without using NaCl, it was observed that small patches of monolayer MoS_2 were formed discontinuously over the substrate at random locations. The layers were formed mostly around some inhomogeneities and towards the edges of the substrates (Figure 3.1(a)). This suggests that the

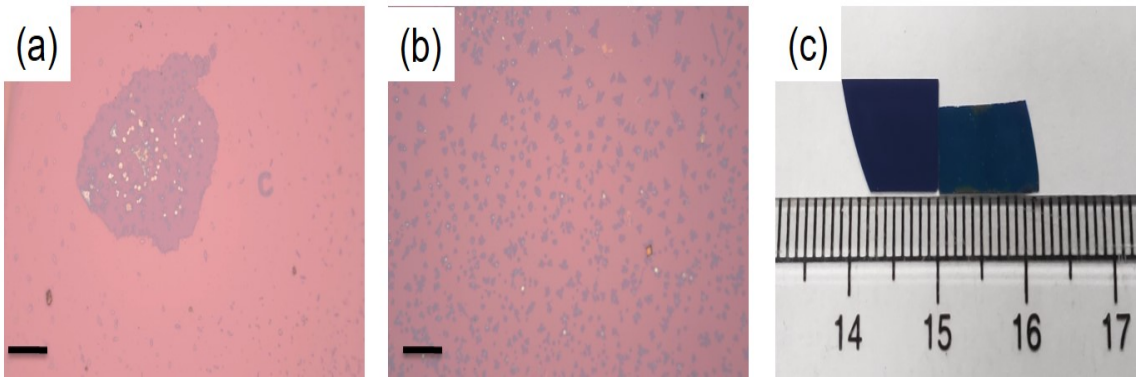

Figure 3.1: Optical microscope images of the sample synthesized (a) without salt (b) with salt coated over the substrate. Scale bar: 20 µm. (c) Comparison of MoS_2 monolayers formed over the entire substrate (right) with a bare substrate (left).

inhomogeneities help in the nucleation and formation of MoS_2 film. Similar observations have been reported earlier.[195, 198] In the absence of any growth promoter, MoS_2 formation was random, and also the repeatability of the result was limited. Monolayers with a length upto 132 µm were obtained at best using this method.

To study the effect of growth promoter, keeping the growth conditions fixed, synthesis was carried out using NaCl (salt) as a growth promoter. 2mM NaCl solution was prepared in distilled water. The solution was coated over the substrate by spin coating and then heated at 150 ℃ to remove water molecules. It was observed that there was a continuous coverage of monolayer over a scale of a centimeter (Figure 3.1(b)). The coverage was only limited by the size of the substrate as we were able to get repeated continuous coverage over bigger substrates under optimal conditions (Figure 3.1(c)). Small patches of bilayers were also observed throughout the sample. NaCl and MoO_3 react in the vapor phase to form an intermediate compound that gets deposited over the substrate, undergoes further sulfurization and promotes the growth of the film.[193] It has been reported that when NaCl is used as a growth promoter, it reacts with MoO_3 first to form an intermediate less volatile compound Na_xMoO_y which reacts with sulfur and form MoS_2.[121] We observed that an optimum concentration of salt is required to grow a large-area monolayer. A higher or

lower concentration resulted in predominantly bulk growth or poor coverage, respectively.

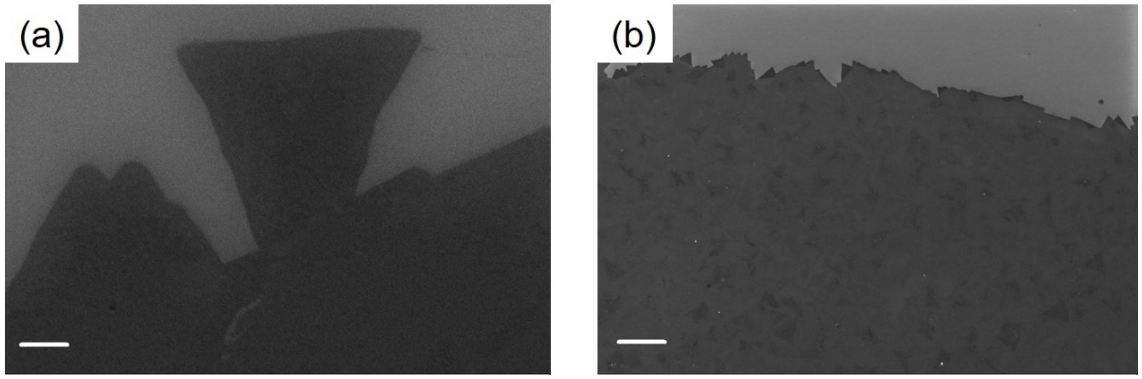

Figure 3.2: FESEM images of the MoS_2 samples synthesized (a) without salt (b) with salt coating. Scale bar (a) 1 µm(b) 10 µm.

Field emission scanning electron microscope (FESEM) images (Figures 3.2(a) and (b)) show the continuity of the synthesized films. The crystal quality of the synthesized film can be inferred from the transmission electron microscope (TEM) images. (Figure 3.3) The selected area electron diffraction (SAED) pattern shows the hexagonal crystal lattice structure and confirms the single crystalline nature of the synthesized MoS_2.

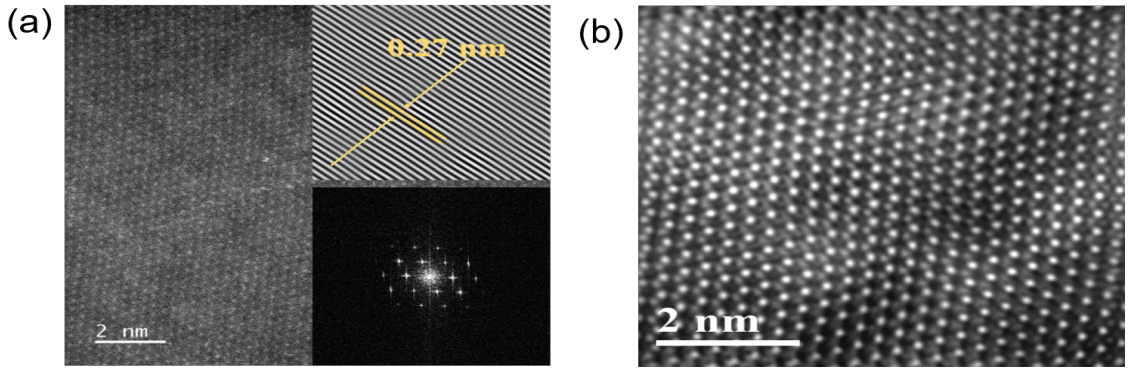

Figure 3.3: (a,b) HRTEM image (bottom inset: SAED pattern, top inset : d spacing) of monolayer MoS_2

Optical Characterisation

Figure 3.4 shows the Raman and Photoluminescence spectra of samples synthesized with and without growth promoter. The difference in E^1_{2g} and A_{1g} peaks, which

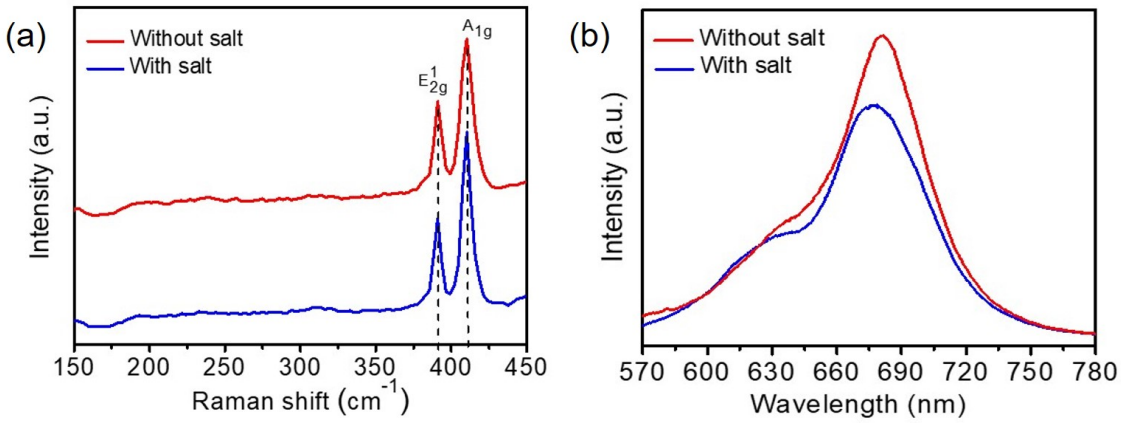

Figure 3.4: (a) Raman and (b) photoluminescence spectra of samples with and without salt coating. It is clearly evident that a similar quality monolayer is obtained in both cases. The absence of any additional peak on the lower side of the Raman spectra indicates no additional disorder is present in the sample synthesized with NaCl.

indicates the number of layers, was found to be 19.24 cm^{-1} (Figure 3.4(a)), which is in accordance with the value of the monolayer.[199] It has been reported that in the presence of disorder, a low-frequency peak in Raman spectra is observed, labeled as LA(M) peak at around ∼227 cm^{-1}. [200, 201, 130] No such peaks were observed in our sample indicating the absence of any disorder. The absence of any additional peaks in the low-frequency side of the Raman spectra indicates that the addition of NaCl did not produce any doping in the as-grown MoS_2.[121]

PL spectra show two direct excitonic peaks corresponding to A1 and B1 excitons.[6] The excitonic peak positions of A1 and B1 were found to be at 681 nm and 634 nm, respectively, for sample without salt and at 677 nm and 631 nm for sample with salt coating (Figure 3.4(b)). The PL peak intensities were higher for the samples

without salt. But our Raman data indicates no enhancement of vacancy-mediated defect in these samples. We think that the lower PL signal from the NaCl-assisted grown sample is due to the reduction of grain boundaries. We have observed that the MoS_2 layers grown without NaCl have more circular in shape with smooth edges (Figure 3.1(a)). This is because in the absence of any growth promoter, MoS_2 flakes were observed to grow in random orientation and with smaller domain size due to the sparsely located nucleation points. This results in flakes with more grain boundaries and irregular shapes. Whereas flakes synthesized with NaCl are composed of large triangular domains. Enhancement of PL from the grain boundary has been reported previously. [202] Also, the shoulder peak in PL spectra of the sample synthesized with NaCl near to 677 nm indicates the presence of negatively charged excitons (trions A-). The appearance of charged excitons indicates that the addition of NaCl during growth can promote the emission efficiency of the excitons.[203]

Electrical Characterisation

Electrical characteristics (Figures 3.5 and 3.6) of the films were studied by fabricating devices using photolithography, followed by depositing 5 nm chromium and 65 nm gold contact materials using thermal evaporation. In both cases, I–V characteristics showed a linear behavior indicating the formation of Ohmic contacts (Figures 3.5(a) and (c)). Significant photoresponse was observed in both cases when illuminated with a white light-emitting diode (LED) of 0.15 mW intensity (Figures 3.5(a) and (c)).

The transient photoresponse of the devices was studied using a 405 nm wavelength LED with 12 mW cm^{-2} illumination intensity and at 1.5 volts applied bias on the sample. Representative photoresponse of samples synthesized without salt coating and with salt coating are shown in Figures 3.5(b) and (d), respectively. The rise time

was slightly less for the sample with salt coating (14.7 s) compared to that without salt (15.9 s), whereas the decay time (32.3 s) was same for both the cases.

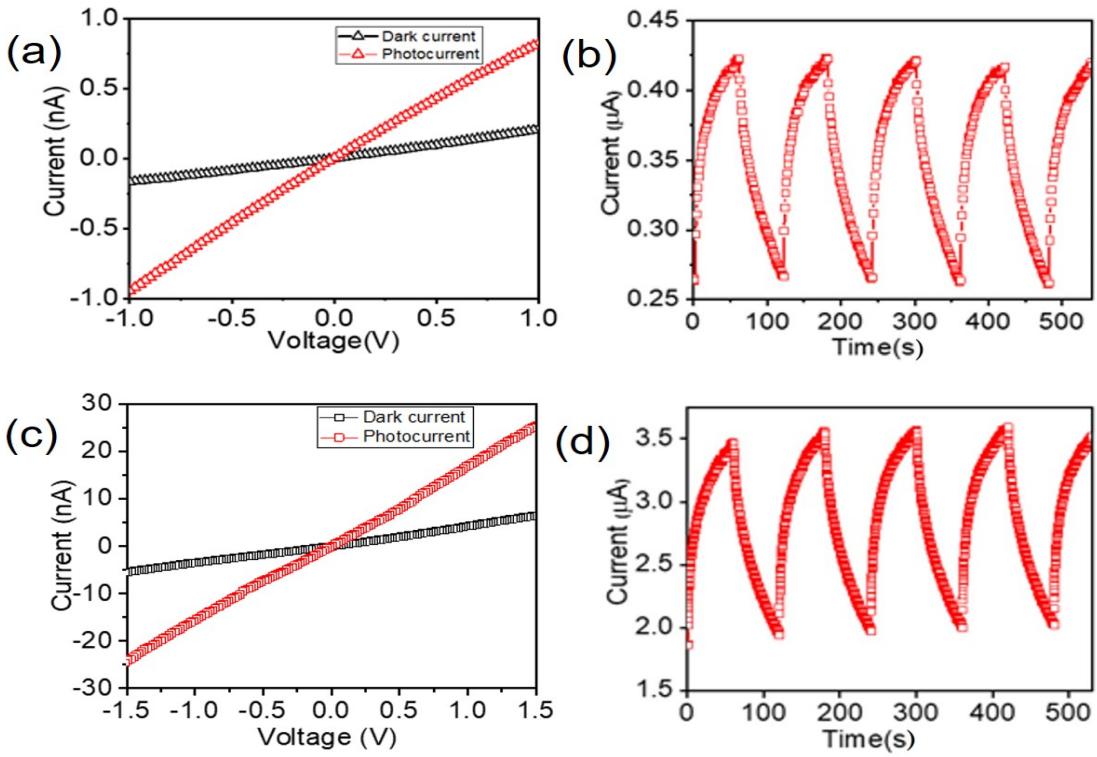

Figure 3.5: *I-V* characteristics and *I-t* characteristics of the MoS_2 sample synthesized (a), (b) without salt (c), (d) with salt coated over the substrate. White LED of 0.15 mW cm^{-2} intensity was used for the photocurrent measurement in (a) and (c). UV LED of 405 nm wavelength and 12 mW cm^{-2} intensity was used for the transient photoresponse measurement shown in (b) and (d)

Carrier transport in the devices was investigated using back gated field-effect transistor (FET) configuration at ambient conditions without any annealing. I_{sd}- V_g transfer curve shows n-type unipolar behavior of MoS_2 (Figures 3.6(a) and (c)). All the devices exhibited an on/off ratio of the order of $> 10^4$. The I_{sd}- V_{bg} transfer curves showed good saturation behavior for both types of samples (Figures 3.6(b) and (d)). Mobility was calculated from the slope of I_{sd}-V_g curve using the following

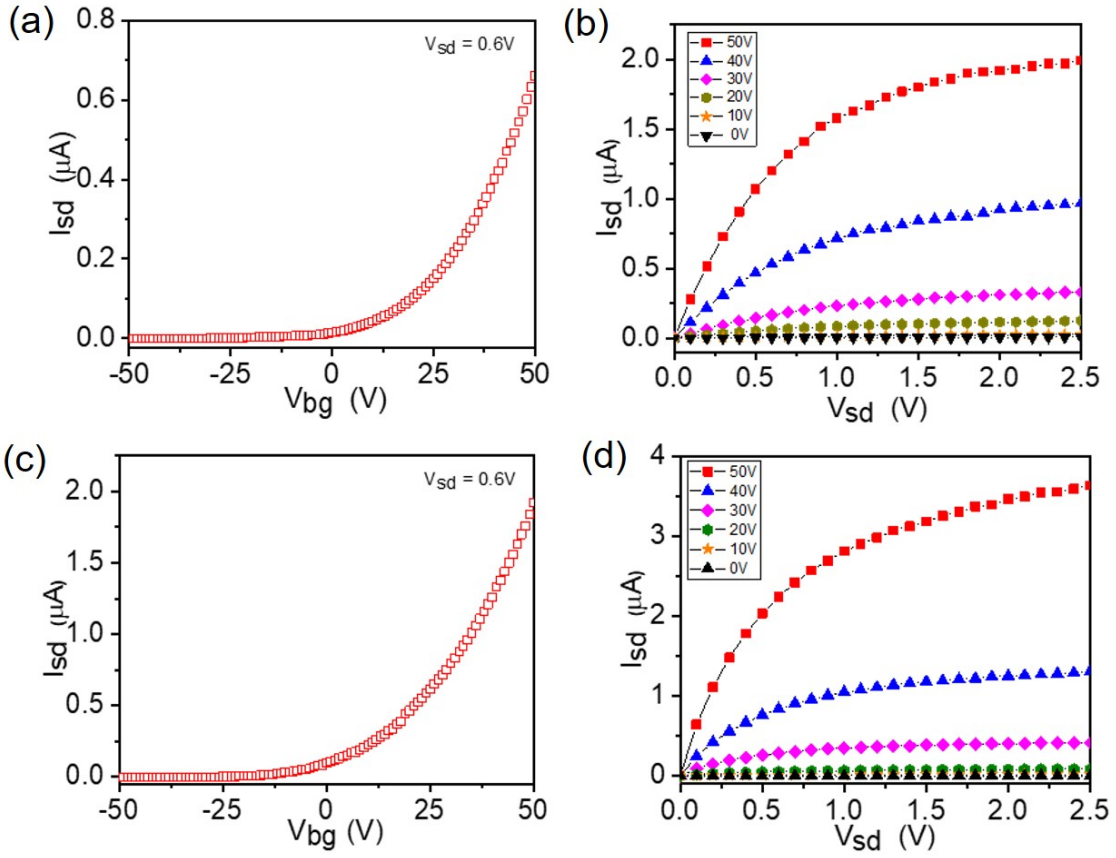

Figure 3.6: Source-drain current versus back gate voltage sweep (I_{sd}- V_{bg}) and source-drain current versus source-drain voltage sweep (I_{sd}- V_{sd}) of devices made on the MoS_2 film synthesized (a), (b) without salt, and (c), (d) with salt. I_{sd}-V_{bg} characteristics show n-type unipolar behavior and good current saturation observed in I_{sd}-V_{sd} characteristics for both type of sample.

equation [120]

$$\mu = \frac{dI_{sd}}{dV_g}\frac{L}{WC_gV_{sd}} \tag{3.1}$$

where L is the channel length, W is the channel width,C_g is the gate capacitance per unit area (C_g = 8.854 x 10^{12} F m^{-1}, ε_r for SiO_2 is 3.9, and d is the thickness of SiO_2, here it is 300 nm). Sample with salt coating showed higher mobility of 1.06 $cm^2V^{-1}s^{-1}$ compared to without salt (0.28 $cm^2V^{-1}s^{-1}$). The reason for the lower value of mobility in without salt sample might be because of an increase in the number of grain boundaries. We have shown in Figure 3.1(a) that without salt grown MoS_2 has

an irregular shape, which could arise if the individual grain sizes within the patch are small. The enhanced scattering of the charge carrier from these grain boundaries is probably the reason for the observed low mobility in samples synthesized without salt. As we have discussed earlier that samples having more grain boundary will have more PL intensity [202], which is also consistent with the relatively large PL intensity observed in these samples (Figure 3.4(b)). Mobility values for samples grown with salt were comparable to those reported at ambient conditions.[204, 205, 206] Since the study was focused only on understanding the effect of growth promoter, there is still scope for enhancement in mobility by annealing, transferring the as-grown sample to another suitable ultra-clean substrate, providing a high dielectric environment or by depositing top gate. Details of the mobility limiting factor will be addressed in the next chapter.

3.3.2 Effect of position of the substrate

The distance and position of the substrate with respect to the source has a profound impact on the resultant film. We have studied the effect of the position of the substrate by keeping the substrate at varying distances from the source. MoO_3 powder was kept at 16 cm from the sulfur source. The substrates were placed 3 mm away from each other on a separate boat at 3.8 cm away from the end of the molybdenum boat, as shown in Figure 3.7(a). Considering the sensitivity of CVD parameters to the resultant film, we fixed a combination of flow rate, growth temperature, time, amount of precursor, the distance between sources and substrate and carefully studied the effect of substrate position by varying the distance of the substrate from the source.

It was observed that (Figures 3.7(c)–(h)) as the distance of the substrate increases, the relative size and coverage of the film first increase and then decrease.

In every substrate, triangle-shaped monolayers were formed, which started merging and forming different shapes showing a tendency to form a continuous film. This tendency initially increased with distance and then decreased (schematically shown in Figure 3.7(b)). Coverage of the film was calculated using ImageJ software. We found that the monolayer area increased from (a) 54.09 % (b) 54.74 % (c) 69.98 % and then decreased to (d) 48.97 % (e) 33.43 % (f) 16.51 %.

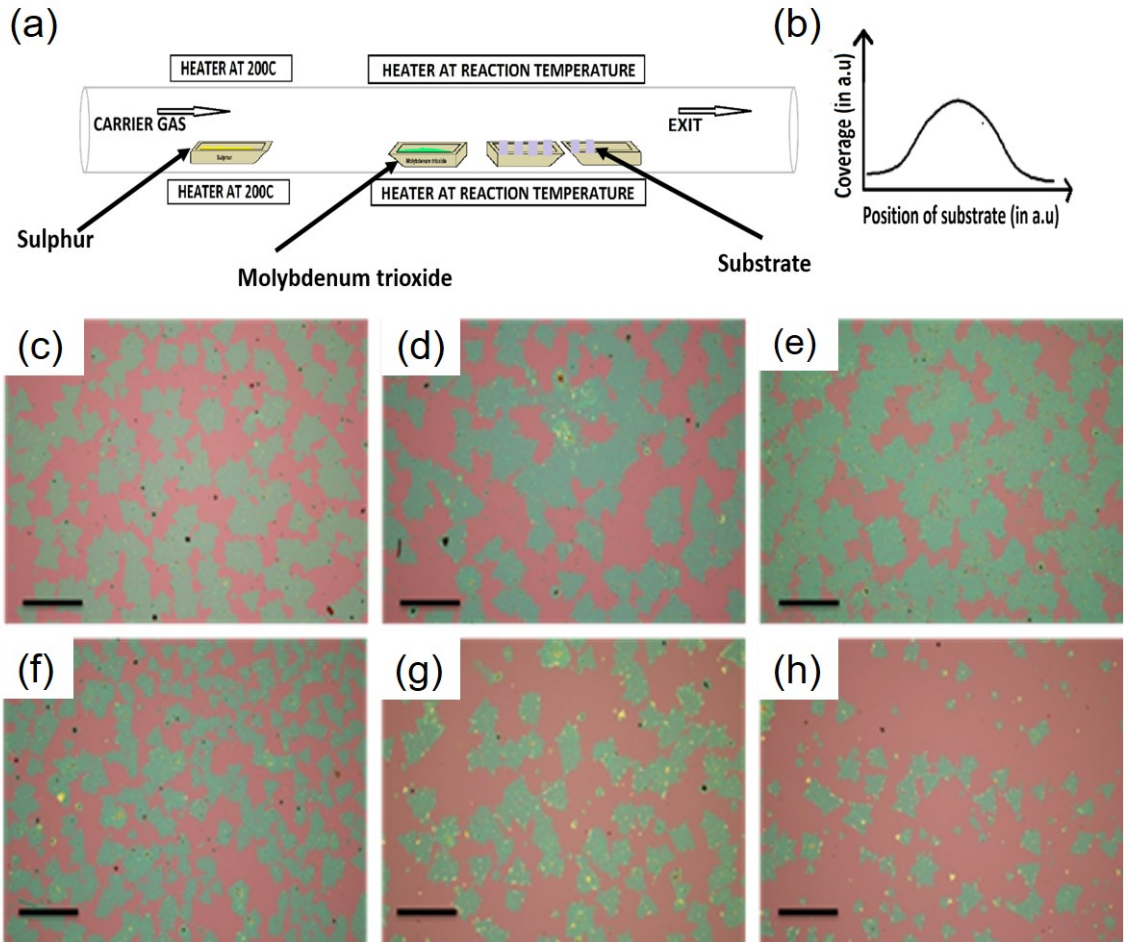

Figure 3.7: (a) Schematic of the effect of position of substrate (distance measured from the edge of the MoO_3 boat) and (b) the schematic shows the variation of coverage of the film over the substrate with the position of the substrate. (c)–(h) Optical images of the sample placed at various distances. Scale bar: 100 µm.

These results show that for a particular set of growth temperature, flow rate,

amount, and distance between the precursors, there is a particular position (sweet spot) of the substrate where the monolayer coverage will be the best. We have repeated the study for different combinations of parameters and found that the position of the sweet spot changes with other parameters. For example, with an increasing (decreasing) flow rate, it moves away (closer) from the MoO_3 boat, and the trend of coverage remains the same. We speculate that the concentration gradient of the vapourised precursor over distance might result in different mixing ratios of the precursors at different points resulting in the different densities and sizes of the layer.

3.3.3 Effect of temperature

Temperature decides the amount of material in the vapor phase, which influences the adsorption-desorption mechanism. The position determines the ratio of the precursor mixture. So we studied the effect of temperature on different positions of the substrates. We choose the values of various other parameters such that the effect of temperature will be prominently visible. The distance between sulfur and MoO_3 sources was fixed at 15 cm. The flow rate of Argon gas was fixed at 24 sccm (which gave a decent flake size of more than 20 microns at 700 ℃).

SiO_2/Si substrates of nearly 1 × 1 cm were placed away from each other. At 650 ℃, we observed the presence of small triangular-shaped monolayer (optical microscope images shown in Figure 3.8), and few-layer (from the optical contrast they were identified as more than 3 layers) triangular domains throughout the substrate up to 6.5 cm. Beyond this distance, the substrates do not have any observable deposition. At 675 ℃, monolayer triangles were observed in all the substrates, with increased size and density compared to 650 ℃. Also at 2.5 cm, long nanorods were observed whose length and density substantially decreased at 4.5 cm and almost was absent

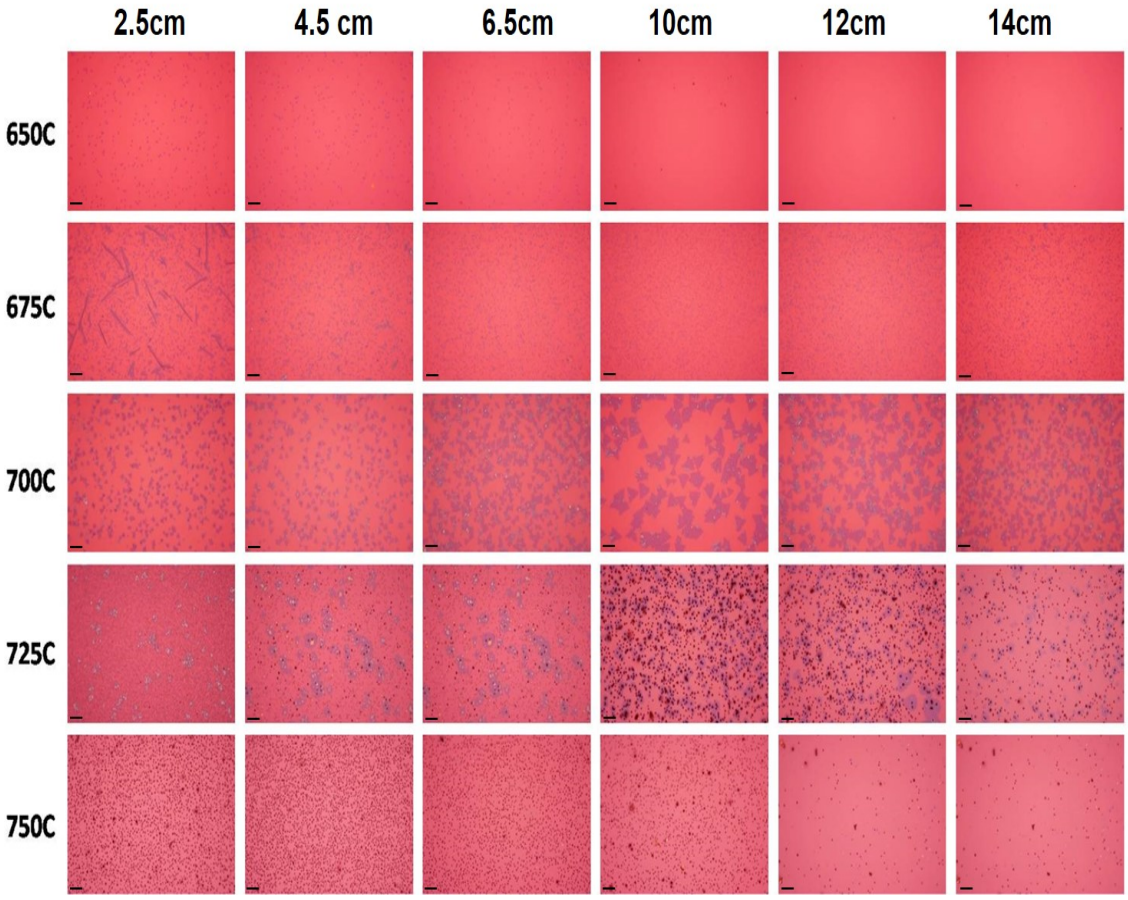

Figure 3.8: Optical microscope images of samples synthesized at various temperatures for different positions of substrates. Scale bar 20 µm.

beyond that. At 700 ℃, along with triangular domains, some star-shaped domains also appeared.

The size of the individual domains increased with distance and became maximum at 10 cm then decreased. At 725 ℃, along with monolayers, the substrate was covered with particles (these are basically bulk MoS_2 deposition) whose density also showed an increase and then decreased. At 750 ℃, the substrates were covered with these bulk MoS_2 particles, and no layers were observed anywhere. From the optical microscope images (Figure 3.8), we also observe that for a fixed distance, an increase in temperature increases the size of the monolayer domain. And after attaining a

maximum size, it starts to decrease on further increase in temperature. For the given conditions, we observed that 700 ℃ was the optimal temperature for the growth of monolayer MoS_2.

These observations can be explained by considering the availability of reactants at a particular substrate position with temperature. At lower temperatures, the rate of vaporization of MoO_3 is less, thereby limiting the available precursor for the reaction. With the increase in temperature, the concentration of available reactants and the rate of reaction increases, which increases the size of the monolayer domain. However, at higher temperatures along with adsorption, desorption of reactants also takes place.[207] The preference of monolayer or multilayer growth will also strongly depend on the amount of precursor available in that particular position. For higher concentrations of precursor and low desorption rate, multilayer or particle growth will be promoted.

3.3.4 Effect of flowrate

To study the effect of the flow rate of carrier gas on the growth of MoS_2 different growth parameters like the amount of precursor, the distance between the precursors, and temperature were fixed while varying only the flow rate of the carrier gas (we have used argon as carrier gas). The flow rate of the carrier gas decides the amount of reactants available for reaction and the time for which the reactants stay at a particular point.

When the flow rate was below 5 sccm we did not observe any deposition on the substrate (Figure 3.9(a)), which indicates that a lower flow rate of the carrier gas cannot carry sufficient precursor to the substrate to facilitate proper reaction. But with 5 sccm argon flow, the substrate was covered with particles. As the flow rate is increased to 7.5 sccm, a continuous monolayer of MoS_2 was obtained (Figure 3.9(b)).

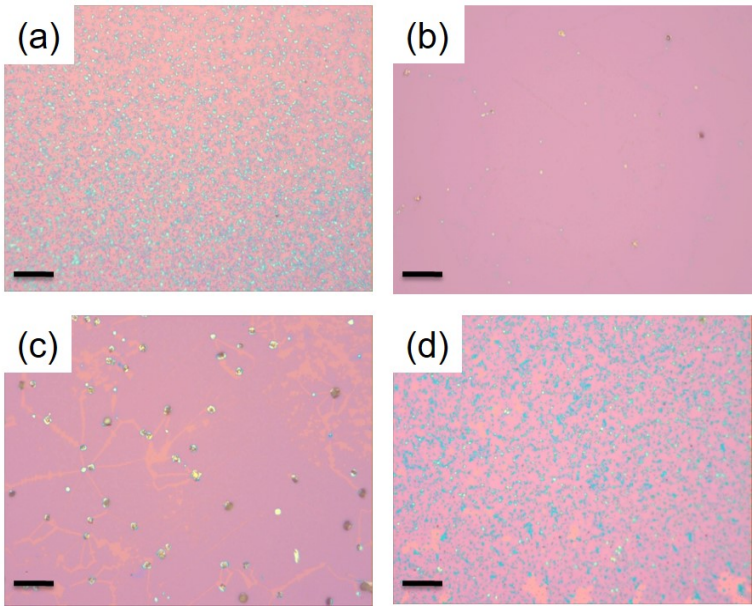

Figure 3.9: Optical images of the obtained MoS_2 sample at a different flow rate of argon: (a) 5 sccm (b) 7.5 sccm (c) 10 sccm (d) 15 sccm. Scale bar 20 µm. It is clear that at 7.5 sccm flow a continuous clean monolayer is obtained with minimal overgrowth.

Further increasing to 10 sccm, cracks were observed in the layer with visible layer boundaries (Figure 3.9(c)). At 15 sccm, along with discontinuous layers, bulk depositions were observed throughout the layer (Figure 3.9(d)). This could be because the presence of excess reactants helps in further nucleation and thereby result in bulk depositions. Our results clearly indicate the presence of a very narrow window (∼2 sccm) of flow rate in which continuous monolayer can be obtained. It is important to mention that this window will depend on the diameter of the CVD tube, the distance between the precursor and substrate, and the amount of precursor.

Optimizing all the growth parameters, we successfully synthesized large area continuous monolayer MoS_2.

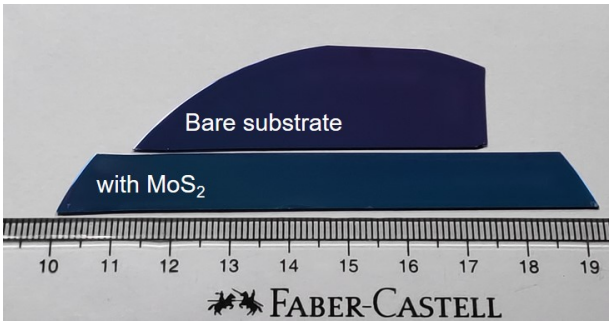

Figure 3.10: Continous monolayer of MoS_2 obtained over the entire substrate (bottom). Bare Si/SiO_2 substrate (top) for comparison.

3.4 Summary

Here we have discussed the synthesis of monolayers of 2D materials using CVD considering MoS_2 as a model system. It is important to mention that the CVD parameter depends primarily on the particular materials one needs to grow.[208, 209, 210] Here we have tried to provide a methodology that will help to optimize parameters for the growth of new materials relatively quickly and in less number of trials. We have discussed various growth parameters taking MoS_2 as an example. For other materials, the parameters will change. But the methodology will be equally useful for the optimization of CVD growth of any 2D materials. In order to elucidate the methodology, we have studied the effects of different growth parameters like flow rate, the position of the substrate, and temperature. A direct comparison of the film synthesized with and without growth promoter was made. Our study shows that treating the substrate with a growth promoter helps in enhancing the coverage of the monolayer and does not degrade the electrical performance of the devices. Also, an optimum concentration of growth promoter is required for large-area monolayer growth. Our study provides a recipe to optimize CVD growth parameters for achieving large-area monolayer of 2D materials. We suggest that, in order to optimize the CVD process (apart from using a suitable growth promoter where the prior knowl-

edge might be available), among several lab-dependent parameters such as flow rate, position of precursors and substrates, one should first take a sufficient amount of precursors, then fix a suitable temperature for growth of a particular material, then do the position-dependent study (by placing substrate at various places) for various flow rate at this temperature. This study will help to quickly find the suitable position of substrate and flow rate for a particular temperature. As temperature and vapor pressure will control the rate of adsorption and desorption on the substrate surface, optimization of temperature for a given precursor concentration will help to reduce the overgrowth. Alternatively, one can fix the temperature and vary the precursor amount. The latter method is preferred for materials with a small temperature window. We hope this systematic study will allow researchers to quickly find the optimum growth condition for the monolayer of many 2D materials using CVD.

Chapter 4

Modulating the Transport Properties of Monolayer MoS_2 FET through Dielectric Engineering

4.1 Introduction

The unique electronic and optical properties of 2D TMDs have attracted research attention over the past decade owing to their potential in various electronic and optoelectronic applications and in fundamental studies.[104, 28] Atomically thin 2D TMDs are very sensitive to their surrounding environment.[37] They experience reduced dielectric screening, producing strong electron-electron and electron-hole interactions.[56] Since the dielectric screening within a 2D material is low, the surrounding environment can strongly modify the interaction between the charge carriers and alter their electronic transport and optoelectronic properties.[37, 36] Dielectric screening provided by the surrounding environment strongly influences the electronic bandgap, exciton binding energy, Coulomb impurity scattering, and defect level transitions in 2D materials.[37, 56, 36, 2]

For example, the quasiparticle bandgap and exciton binding energy of monolayer TMDs have been tuned by several 100 meVs, by varying the surrounding dielectric environment.[211, 35] 2D TMDs are also known to have various structural defects.[212, 213, 53] Depending on the energy level of the defects, they can be shallow or deep.[214, 215] The deep defects, which can be detrimental to the de-

vice's performance can be made shallow by modifying the effective dielectric constant of the surrounding environment.[3] 2D TMDs also suffer from low mobility values, primarily due to the scattering of charge carriers by the Coulomb impurities.[4] Mobility can be enhanced considerably by screening the long-range Coulomb impurities using a high dielectric constant (ϵ) gate dielectrics or by encapsulating in a high ϵ environment.[56, 4, 38] For instance, transport studies in graphene transistors have shown mobility enhancement by varying the surrounding dielectric environment.[216, 217] Similarly in TMDs, the room temperature mobility in a monolayer MoS_2 FET was increased to 200 cm^2/Vs by depositing 30 nm HfO_2 as the top gate dielectric.[57] A threefold enhancement in mobility was also observed when a thin layer of Al_2O_3 was coated on a back-gated monolayer MoS_2 device.[206]

Though high ϵ solid dielectrics effectively screen the Coulomb impurities and enhance the mobility, the surface optical phonons from the dielectric degrade the mobility of the devices by scattering the charge carriers at room temperature.[217, 51, 218] The competitive effect between dielectric screening and surface phonon scattering in high ϵ dielectrics leaves little room for mobility improvement. [4, 217, 219] On the other hand, the absence of long-range surface phonon vibrations in liquid dielectrics [220] makes them suitable for understanding the effect of Coulomb impurities on carrier scattering with a tunable dielectric environment.

In this chapter, we modulate the electronic transport and optoelectronic properties of monolayer MoS_2 by varying their surrounding dielectric environment using various liquid dielectrics. A major advantage of using liquid over solid dielectrics is the possibility of studying the effect of several dielectric mediums on the same device. The dielectric screening of charged impurities by the dielectric medium produced a significant improvement in the ON current and mobility of the FET device. For a back-gated FET, mobility monotonously increased with the dielectric constant of the medium demonstrating more than two-order enhancement. Also, with an increase

in the source-drain bias and in the presence of a high ϵ medium, the output characteristics exhibited a non-linear increase in the source-drain current deviating from the saturating behavior. We also observed a change in the photoresponse relaxation times calculated from the time-resolved photoresponse of the device with the dielectric medium. The rise time increased, and decay time decreased with an increase in the dielectric constant of the medium. These results are discussed in terms of the dielectric screening of Coulomb interactions between the charge carriers and defects by the dielectric medium.

4.2 Experimental details

FET devices were fabricated on CVD-grown monolayer MoS_2. A degenerately doped p-type silicon with 300 nm thermally grown SiO_2 was used as the substrate. Contact leads were patterned using photolithography, followed by chromium/Gold (5nm/65nm) metal deposition by thermal evaporation. Devices had a channel length (L) of 4 µm and width (W) of 27 µm (Figure 4.1(b)). The surrounding dielectric environment was varied by exposing the semiconducting MoS_2 channel to various organic liquids (Hexane, Anisole, Novec 7100, Isopropyl alcohol (IPA), Methyl ethyl ketone (MEK)) with dielectric constant varying from 1.89 to 18. A constant supply of the liquid was maintained to ensure that the liquid did not get dried on the device and any additional scatterer got adsorbed on the channel surface. To prevent the liquid from coming in contact with the back silicon and change the effective capacitance, PDMS (poly(dimethylsiloxane)) wells were patterned around the devices, which will restrict the liquid to the top of the device only (Figure 4.1 (a)).The inner diameter and the depth of the PDMS well were around 0.5 cm. PDMS does not dissolve in any of the chosen liquids [221] and hence do not contribute to any additional scattering or conductivity. To prevent errors due to any leakage current, the metal contact pads were

masked by depositing an insulating layer of silicon nitride (SiN_x), which prevents the metal pad from coming in direct contact with the liquids. Measurements were also performed without masking, and similar results were obtained. After every measurement, the liquid was removed, and devices were washed in acetone and IPA and then blow-dried with nitrogen gas. Possible errors due to any leakage current through the liquid mediums were also taken care of by measuring a blank device of the same dimension without MoS_2. FET measurements were performed using Yokogawa GS820 multichannel source-measure unit. All the measurements were performed at ambient conditions and at room temperature.

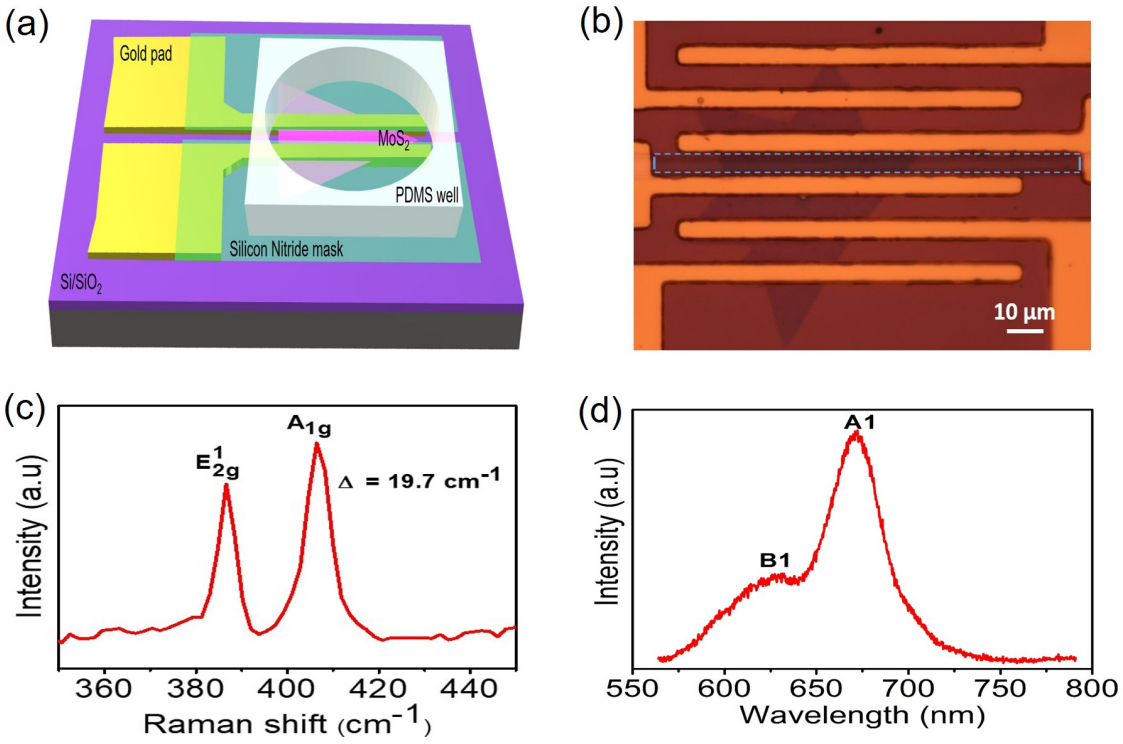

Figure 4.1: (a) Schematic of the device geometry and PDMS well patterned around the device to restrict the liquid just at the top of the device (b) Optical microscope image of the device fabricated over monolayer MoS_2.To avoid any leakage current, the liquid was prevented from coming in direct contact with the metal contacts by depositing silicon nitride and an opening (area within the dotted lines) was made at the semiconducting channel to control the surrounding dielectric environment. (c) Raman spectra and (d) Photoluminescence (PL) spectra of monolayer MoS_2.

4.3 Results and discussions

Figure 4.1 (b) shows the optical microscope image of the device fabricated over CVD-grown monolayer MoS_2 with an insulating layer of silicon nitride deposited on top, which prevents the gold contacts from coming in direct contact with the liquid dielectric medium. Monolayer MoS_2 was identified and confirmed by Raman spectroscopy. Figure 4.1 (c) shows the Raman spectra of monolayer MoS_2. Raman shift of 19.7 cm^{-1} between the in-plane (E^1_{2g}) and out-of-plane (A_{1g}) vibrational modes confirm the formation of monolayer MoS_2.[124, 191] Further, the photoluminescence peaks were observed at 671 nm and 628 nm corresponding to the A1 and B1 excitons of monolayer MoS_2.[6]

4.3.1 Transfer Characteristics

The influence of the surrounding dielectric environment was studied by performing electrical measurements on two terminal devices fabricated on monolayer MoS_2 with silicon as the back gate. The transfer characteristics of the devices (Figure 4.2 (a)) in the presence of various liquid dielectric mediums like hexane, anisole, Novec, IPA, and MEK were studied. The ON current and the transconductance of the device increased in the presence of the dielectric medium. The larger the dielectric ϵ of the medium, the greater the enhancement observed. This enhancement can be attributed to the reduction in the charge carrier scattering due to the dielectric screening of Coulomb impurities. All the devices maintained an ON/OFF ratio $\geq 10^4$ in all mediums. In addition to the dielectric screening of Coulomb impurities, the increase in OFF current could also be due to the detrapping of electrons from the defect states. Various defects present in MoS_2 can act as deep or shallow traps depending on their position in the energy gap.[222] Sulfur vacancies, usually present

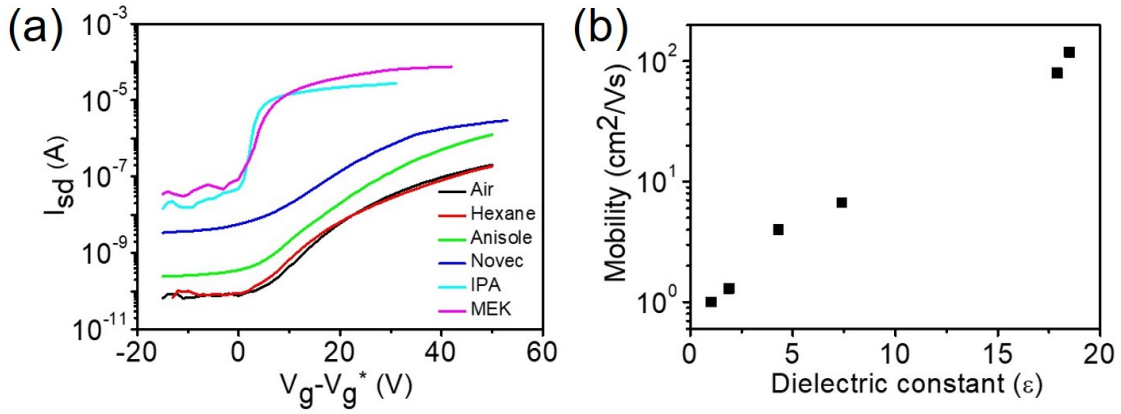

Figure 4.2: (a) Comparison of transfer characteristics of MoS_2 FET in the presence of various dielectric mediums. (V_g^* is the gate voltage at which I_{sd} starts increasing above the OFF state) (b) Mobility as a function of the dielectric constant of different mediums.

in MoS_2, can induce deep defect levels.[47] Deep defect levels can be screened by a dielectric medium and get transitioned into shallow levels.[3] Depending on the dielectric constant of the medium, more shallow levels can be generated. When a negative gate voltage is applied, the fermi level is far away from the conduction band edge, and the detrapping of electrons from the shallow levels lying closer to the conduction band occurs, causing an increase in the OFF current.[223] Hence we observe an increase in both the ON and OFF current with an increase in the dielectric constant of the surrounding dielectric medium. In addition, the reduction in the bandgap of MoS_2 with the dielectric environment could also contribute to the increase in OFF current.[35]

The field effect mobility (μ) of the devices were calculated using the Y function method.[96] Mobility determined using this method is considered more accurate and free from the influence of contact resistance due to the presence of Schottky barrier at the source and drain electrodes. Y function is defined as [96]

$$Y = \frac{I_{sd}}{\sqrt{g_m}} \tag{4.1}$$

and

$$\mu = [\frac{dY}{d(V_g - V_t)}]^2 \frac{L}{WC_{ox}V_{sd}} \tag{4.2}$$

where I_{sd} is the source-drain current, C_{ox} is the oxide capacitance, V_t is the threshold voltage, g_m is the trans conductance defined as $g_m = \frac{dI_{sd}}{dV_g}$ and V_g is the gate voltage. The device exhibited mobility of 1 cm^2/Vs in the absence of any liquid dielectric medium. This value is in the range of previously reported mobility values measured at ambient conditions and for devices fabricated on Si/SiO_2 substrate without any dielectric encapsulation.[57, 179] But there was a significant mobility enhancement in the presence of the dielectric medium. Mobility monotonously increased with an increase in the dielectric constant of the medium. A maximum value of 119 cm^2/ Vs was obtained for the device measured in MEK, demonstrating more than two order enhancements. Four devices were measured and all the devices showed a similar trend. This enhancement in mobility can be attributed to the dielectric screening provided by the surrounding dielectric medium.

Mobility in 2D TMDs are often limited by various charge scattering mechanisms like Coulomb impurities, structural defects, traps, lattice phonons, and remote interfacial phonons etc.[224] Relatively low initial mobility of devices in the ambient conditions and the significant mobility enhancement in the presence of dielectrics points out the presence of a substantial amount of Coulomb impurities. Coulomb impurities act as sources of long-range scattering centers. Various sources of Coulomb impurities can be the charge traps present at the interface between MoS_2 and the dielectric [38] or sulfur vacancies, defects, or traps within MoS_2 [53] etc. In addition, gaseous adsorbents at the channel surface at ambient conditions or any chemical residues from fabrication can also contribute to Coulomb impurity scattering. Hence the Coulomb interaction between the charge carriers and charged impurities have been screened by the surrounding dielectric medium, reducing the charge carrier scattering and increasing the mobility.[225]

The screening of Coulomb impurities by the dielectric medium can be observed by studying the dependence of conductivity ($\sigma = \frac{L}{W}\frac{I_{sd}}{V_{sd}}$) on the carrier density $n \propto \Delta V_g$. For two-dimensional electron systems with parabolic energy bands, $\sigma \propto n^2$, indicates

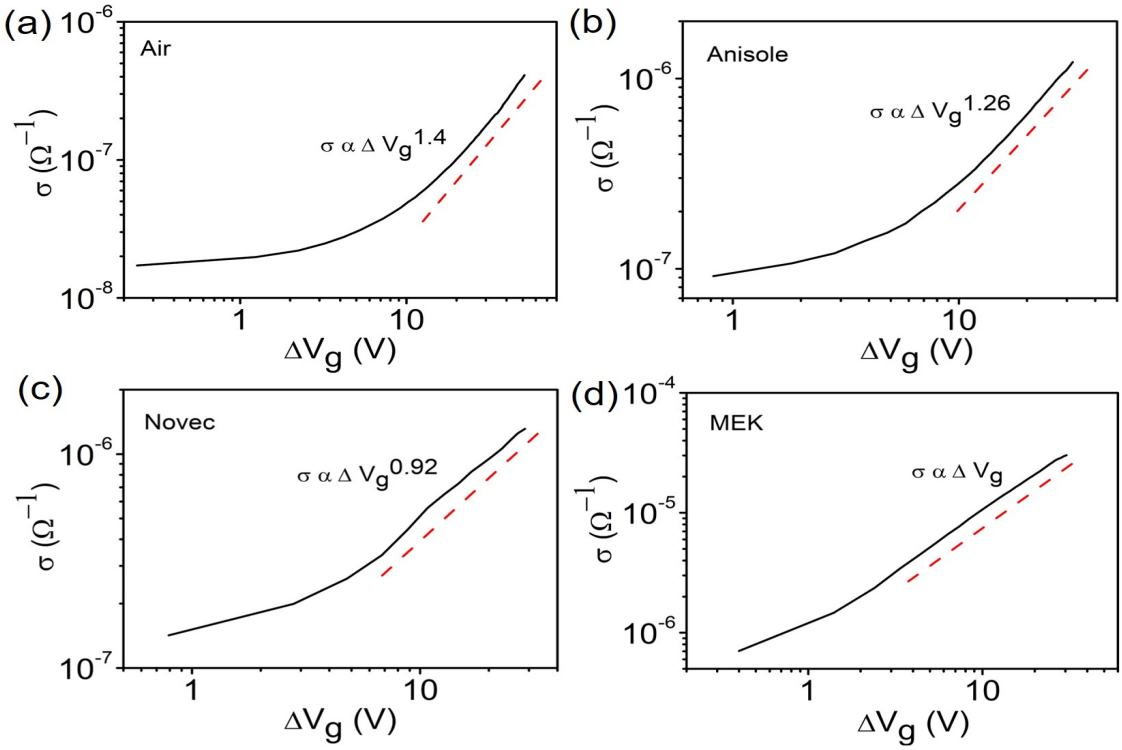

Figure 4.3: Variation of conductivity (σ) with ΔV_g in (a) air and in the presence of different dielectric mediums (b) Anisole (c) Novec (d) MEK. The dependence of conductivity on the carrier density can give information about the nature of screening of Coulomb impurities.

an unscreened Coulomb impurity, whereas $\sigma \propto n$ indicates a screened Coulomb impurity.[55, 226] Figure 4.3(a-d) shows the dependence of σ on ΔV_g ($\Delta V_g \propto n$) in the absence and presence of various dielectric mediums. In the absence of any high dielectric medium, σ had a stronger dependence on n, ($\Delta {V_g}^{1.4}$) whereas the dependence gets weaker with the increasing dielectric constant of the medium. In the presence of MEK, σ has a linear dependence on n, indicating an efficient dielectric screening of Coulomb impurities.

The Subthreshold swing (SS) of the devices was calculated and the values were usually high 10V/decade in the absence of any dielectric medium. SS was calculated using the following expression [96]

$$SS = \frac{dV_g}{dlog_{10}I_{sd}} = \frac{kT}{q}ln(10)(1 + \frac{C_S + C_{IT}}{C_{OX}}) \tag{4.3}$$

(where V_g is the gate voltage, I_{sd} is the source drain current, k is the Boltzmann constant, T is the temperature, q is the electron charge, C_S is the is the semiconductor capacitance, C_{IT} is the interface trap capacitance and C_{OX} is the oxide capacitance). For a fully depleted MoS_2 FET, $C_S = 0$.[96] If there were no interface traps present, then the term in the bracket in equation (4.3) would be equal to one giving SS = 60mV/dec. But the obtained high value of SS in our device clearly signifies the presence of interface traps at the semiconductor dielectric interface.[227] Several reports have shown the presence of charge traps at the semiconducting channel and at the channel dielectric interface.[51, 55, 54] Structural defects like sulfur vacancies also contribute to interface trap states. With an increase in the dielectric constant of the surrounding dielectric medium, we observed a significant decrease in the value of SS from 10 V/decade in air to less than 2 V/decade in MEK. This improvement in SS can be ascribed to the dielectric screening of the charge traps and Coulomb impurities.

4.3.2 Output Characteristics

The effect of surrounding dielectric was further studied by analyzing the source-drain (output) characteristics of the devices. Output characteristics exhibited good saturation behavior under ambient conditions (Figure 4.4(a)) and without any high dielectric medium. The nature of the source-drain characteristics remains the same in the presence of lower dielectric medium (Figure 4.4(b)), whereas in the presence

of a higher dielectric medium, (Figure 4.4(c)) a significant deviation was observed. In the presence of MEK, I_{sd} does not maintain the saturation character. The out-

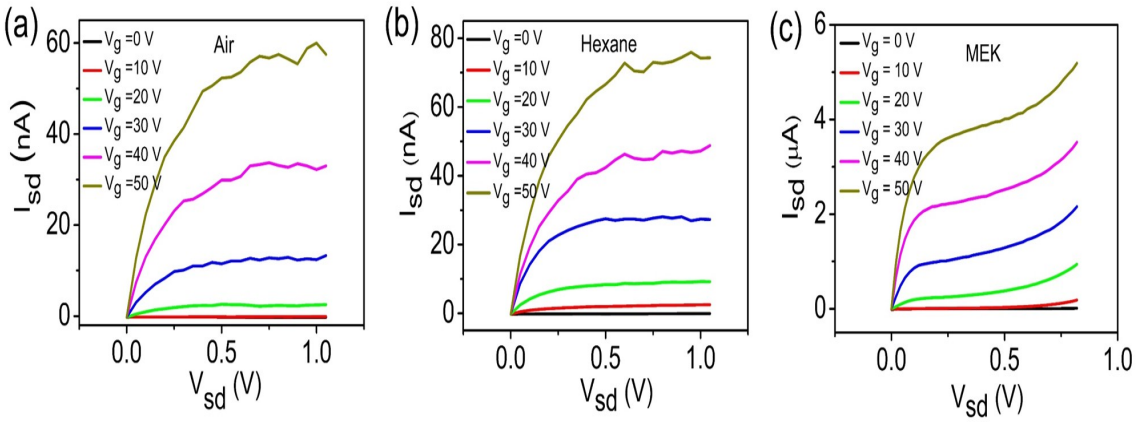

Figure 4.4: Source drain characteristics in the presence of (a) air, (b) hexane and (c) MEK as the surrounding dielectric medium.

put curve now increases above the saturation current for a lower source-drain bias. Such a sudden increase in current is usually observed with an increase in carrier concentration. In 2D materials, various defects, and impurities present can act as deep-level traps. Since 2D materials are very sensitive to their surrounding environment, the Coulomb interaction between the bound electrons and charged impurity in the presence of a dielectric medium gets screened and weakened producing a deep to shallow defect level transition.[2] The position of the defect transition level increases with an increase in the dielectric constant of the surrounding dielectric medium.[2, 3] More deep levels become shallow, and the energy needed to produce mobile charge carriers reduces. Thus as the source-drain bias V_{sd} increases, more electrons get de-trapped and are now available for conduction.[228, 229] Hence, an increase in dielectric screening delocalizes the spatial distributions of the defect charge densities [2], reducing their strength and increasing the source-drain current. Another possible reason for the observed output characteristics could be the reduction in the bandgap of MoS_2 in the presence of a higher dielectric medium. With a decrease

in the bandgap, the voltage (V_{sd}) range over which the current remains saturated decreases.[230]

4.3.3 Time resolved photoresponse

The dielectric environment, also strongly modulates the optoelectronic properties of 2D materials. Studying the time-resolved photoresponse of monolayer MoS_2 in the presence of various dielectric mediums can give further insights into the effect of dielectric screening on carrier transport. The relaxation times were measured in the presence of two different dielectric mediums (anisole and Novec) and compared with that of the pristine device. (Figure 4.5)

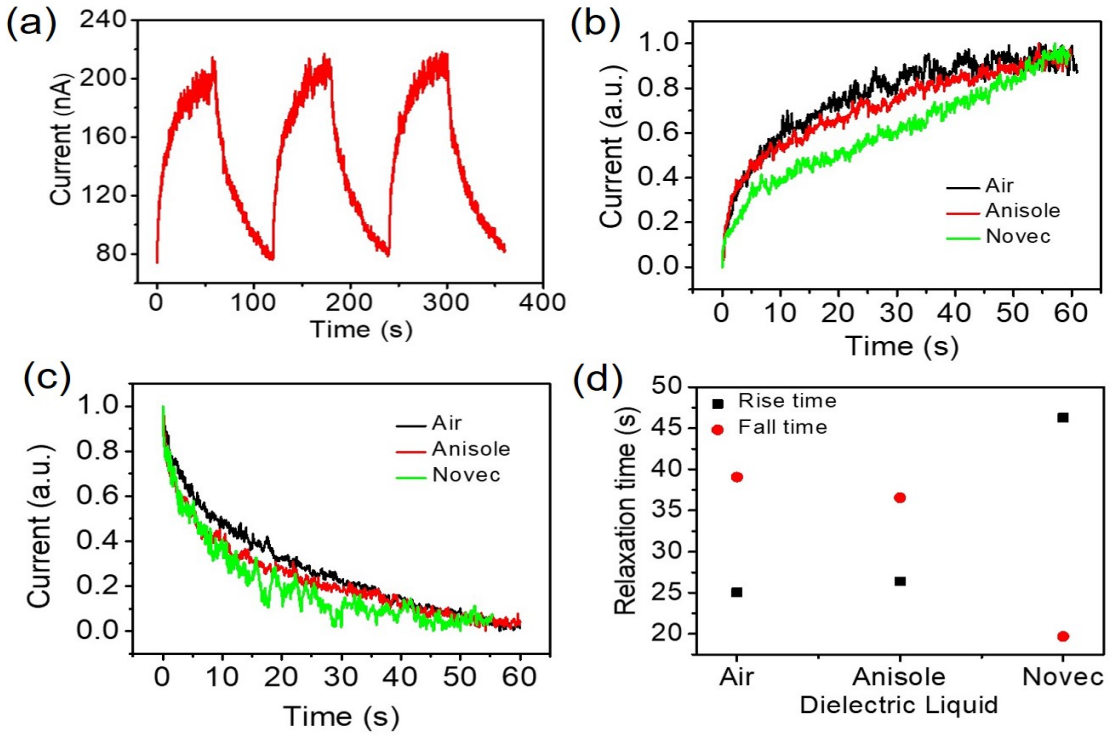

Figure 4.5: (a) Time-resolved photoresponse across monolayer MoS_2 when illuminated with 405 nm LED at an intensity of 10 mW/cm^2. Comparison of (b) rising edge (c) falling edge, (d) rise time, and fall time in the presence of various dielectric mediums.

The chosen liquids do not have any absorption at the incident wavelength. The device was biased at 1 V and illuminated with a 405 nm LED at an ON-OFF interval of 1 minute (Figure 4.5(a)). The rise and fall time demonstrated a dependence on the dielectric constant of the medium. (Figure 4.5(b,c)) With the increase in dielectric constant, the rise time was observed to increase and the fall time to decrease (Figure 4.5(d)). This change can be associated with the screening of defect levels in MoS_2 by the dielectric medium.

The trap states present in the device determine the time taken by the photocurrent to reach a steady state value, whereas the value of the steady-state current is determined by the recombination centers.[231] When a semiconductor is illuminated with light, the equilibrium Fermi level splits into two steady-state Fermi levels corresponding to the density of holes and electrons in the valence and conduction bands. Those states lying between the steady states act as recombination centers whereas those lying between the steady state and band edges act as trap states. Here, as the increased dielectric screening provided by the surrounding dielectric medium delocalizes the strongly localized states, deeper defect levels get transitioned into shallow levels generating more trap states. With the increase in the trap states, to reach a steady value of photocurrent, the density of carriers trapped in the trap states should be increased in proportion to the density of free carriers.[231] Hence we observe an increase in rise time with an increase in the dielectric constant of the surrounding medium. The decay time is usually limited by the deep traps.[215] In a photoconductor, the decay time is given by [215]

$$\tau_{\mathrm{t}}^{-1} = s_{\mathrm{p}} N_{\mathrm{v}} V_{\mathrm{th}} \exp\left(\frac{-\Delta E}{kT}\right) \tag{4.4}$$

where s_p is the capture cross-section of the trap center, N_v is the effective density of states in the valence bands, V_{th} is the thermal velocity of the carriers and ΔE is the energy difference between the trap state and the valence band edge ($\Delta E =$

$E_{tp} - E_v$). As the energy difference between the trap state and band edges increase, the detrapping time increases which in turn increases the decay time. Since the defect transition level is inversely proportional to the effective dielectric constant of the material, more deep levels become shallow as the dielectric screening increases. Hence with an increase in the dielectric constant of the surrounding medium, we observe a decrease in the fall time.

4.4 Summary

In summary, the sensitivity of 2D TMDs to their surrounding environment have been exploited to tune their optoelectrical transport properties. We obtained a two-order enhancement in mobility by varying the dielectric constant of the surrounding medium. The efficient dielectric screening of Coulomb impurities by the surrounding medium resulted in a monotonous increase in mobility. The reduced bandgap and screening of defects in MoS_2 by the dielectric medium produced a non-linear increase in source-drain current deviating from the saturation behavior in the output characteristics. The screening of defects also contributed to the modulation of the transient photoresponse relaxation times. Our study demonstrates a method of improving the mobility and photoresponse relaxation in TMDs and provides a substratum to investigate the intrinsic properties of MoS_2 as well as other TMDs, with potential application in various high-performance electronic and optoelectronic devices. A better understanding of 2D devices in liquid environments will also help in better designing various chemical and biological sensors and wearable devices.

Chapter 5

Photoresponse Enhancement in Mixed-Dimensional vdW Heterostructure through Dielectric Engineering

This chapter is an adaptation of the research article published in " Advanced Materials Interfaces 9(9), 2102054, 2022".

5.1 Introduction

2D materials and their heterostructures offer greatly tunable optoelectronic properties which are not accessible in conventional 3D materials. 2D materials, because of their reduced dimension, experience weak dielectric screening.[232, 233] This results in a large exciton binding energy [232, 233, 32, 41, 234, 235] as well as increased quasiparticle band gap [35] and make the electrical and optical properties of the material susceptible to its dielectric environment.[33, 236] As mentioned in the previous chapter, the dielectric environment modifies the electron-hole interactions in 2D materials and helps in controlling the band gap of 2D materials [35, 237] without disturbing the pristine quality of these materials. The the dielectric environment also plays a crucial role in determining the impurity scattering of charge carriers in 2D materials.[56, 38, 238] Depending on the dielectric mismatch between the 2D semiconducting materials and the surrounding dielectric environment, the effective potential experienced by a mobile electron due to an ionized impurity at the surface

of the membrane enhances or diminishes.[56] This effect also depends on the thickness of the semiconducting membrane. When the thickness increases above a critical limit, dielectric mismatch has no effect on Coulomb scattering.[56] All these effects show that controlling the dielectric environment of 2D materials is particularly interesting because of its profound impact on the electronic band gap, screening, exciton and trion binding energies, exciton transport, and mobility modulation, which can help toward the the efficient design of various optoelectronic devices.

Even though research on 2D TMDs is growing faster with the discovery of more exciting properties, its production and application has not yet started at an industrial scale. So, it is very important to look for the possibility of combining the properties of these 2D TMDs with the existing semiconductor technology. For various optoelectronic applications, p–n junctions are one of the most important building blocks. Conventional p–n junction made from 3D materials works due to the formation of a depletion layer at the junction area of p-type and n-type bulk materials. The characteristic of the depletion layer is determined by the dopant type and their amount on both sides. The electric field present at the junction is responsible for the separation of charge carriers in photodetectors and solar cells. In the case of heterostructures of 2D materials, the p–n junction is formed due to the particular band structure of the two adjacent layers held together by van der Waals interaction.[97, 239] In this case, due to the presence of van der Waals gap, no depletion layer forms nor band bending takes place and charge transport occurs via tunneling or hopping across the van der Waals interface.[98, 240, 241] A single layer of n-type MoS_2, when combined with p-type silicon, forms a type-II heterojunction.[66, 84] Such a 2D–3D heterojunction would help in the effective separation of electron–hole pairs which found potential applications in photodetectors [242, 243, 244, 103, 245, 246] and solar cells.[66, 247, 99, 248, 249]

Heterostructures of MoS_2 with several bulk semiconductors like Si, Ge, GaAs,

GaN, etc. have been studied, previously.[250] But combining MoS_2 with silicon is particularly interesting because of the excellent compatibility of silicon with the existing CMOS process and the possibility of silicon acting both as a substrate and an active component with promising performance. The choice of silicon type results in a different photodiode behavior due to the difference in band alignment between MoS_2 and n/p-type silicon.[169] The strong built-in electric field at the p-n junction formed between p silicon and n MoS_2, facilitates the efficient separation of photogenerated charge carriers. It is a minority carrier-dominated device. In contrast, a weak built-in field is developed at the n silicon/n MoS_2 interface with a majority carrier-dominated transport. Here the photogenerated exciton modulates the photoresponsivity by varying the barrier height and width at the interface. In addition, the reverse saturation current shows a deviation from the exponential current of the p-n junction due to the dependence of its barrier height on the applied voltage. A single layer of MoS_2 can absorb as much solar light as 50 nm of silicon.[251] Thus, with MoS_2 as the photoactive layer could compensate for the requirement of thicker silicon for efficient solar absorption.[252] Band-to-band tunnel field-effect transistors formed by vdW heterostructure of bilayer MoS_2 and highly doped Ge have exhibited subthermionic subthreshold swing.[241]

In this chapter, we utilized the effect of a dielectric environment to achieve large enhancement in the photodetection properties of mixed-dimensional vdW p–n junctions fabricated by placing n-type MoS_2 monolayer atop p-type silicon. We used heavily doped Si as this will help in establishing a large electric field at the van der Waals interface.[241] Also, the observed photoresponse will have only features of MoS_2, which will help to identify the changing contribution of MoS_2 layer in varying dielectric environments. Due to the bulk nature of the silicon, the changing dielectric constant of the environment will have little or no effect. Any change in the optoelectronic properties of such 2D–3D hetero-interface p–n junction will be primarily due to the MoS_2 monolayer. We studied the optoelectronic characteristics

under varying dielectric environments to understand how the change in the dielectric environment affects the current-voltage characteristics and photoresponse properties of these heterostructures. Several liquids as well as solid dielectrics with various dielectric constants were used to tune the dielectric environment. A large enhancement in photocurrent was observed with the increasing dielectric constant of the environment. Though we observed increased dark current with increasing dielectric constant, the overall enhancement of photoresponse was much stronger.

5.2 Experimental details

5.2.1 CVD synthesis of MoS_2

60 mg MoO_3 powder was placed in an alumina boat at the center of the furnace. 600 mg sulfur was placed in a separate boat at around 200 ℃ towards the left of MoO_3 boat separated by a distance of 15 cm. SiO_2/ Si substrates were placed facing up on a separate boat towards the right of MoO_3 boat at a distance of 2cm from it. The reaction was carried out at 700 ℃ for 20 minutes with nitrogen as the carrier gas at a flow rate of 28 sccm.

5.2.2 Heterostructure fabrication

Silicon-MoS_2 heterostructure was formed by transferring CVD-grown monolayer MoS_2 using a wet transfer method onto a patterned SiO_2/ Si substrate. The substrate consists of degenerately doped p-type silicon (0.001-0.005 ohm-cm) with 300 nm thermally grown SiO_2. A part of the SiO_2 was removed from the SiO_2/ Si substrate by a combination of wet and dry etching. Initially, 250 nm SiO_2 was removed by reactive ion etching (RIE) using a SF_6: O_2 mixture. The remaining 50 nm was removed

by buffered oxide etchant (BOE). A second wet etching step was done with dilute HF to passivate the Si surface properly.[253] Monolayers of MoS_2 were immediately transferred onto this surface. The atomic force microscope image of the silicon surface after the etching process shows the formation of a smooth surface (Figure 5.1).

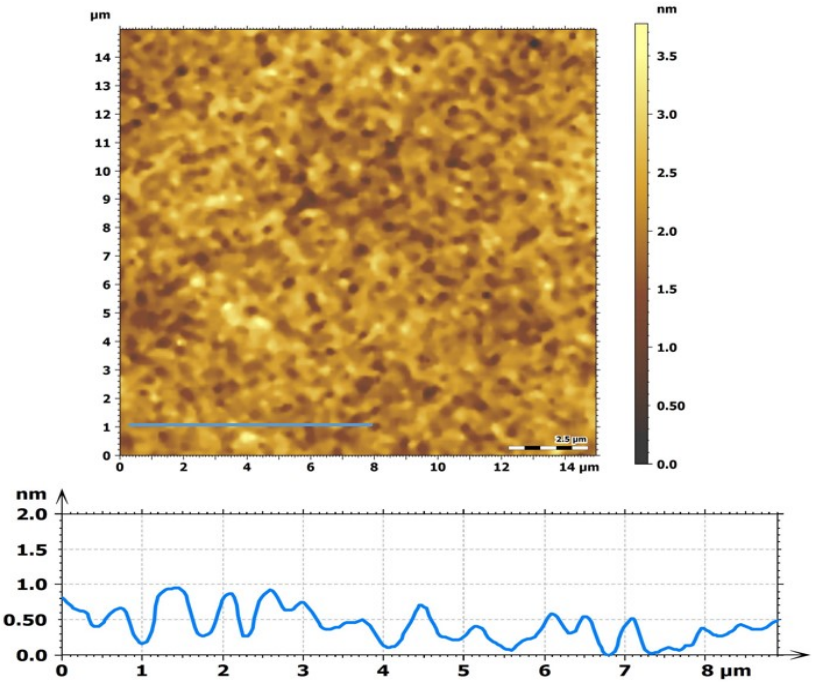

Figure 5.1: (a) AFM image and (b) Line profile (corresponding to the blue line in fig.(a)) of the silicon surface after etching the SiO_2 layer.

The root mean square (RMS) roughness of the silicon surface after etching the SiO_2 layer is about 0.362 nm with a mean height of less than 1 nm, indicating a smooth surface. Figure 5.2 shows the various steps involved in making the heterostructure.

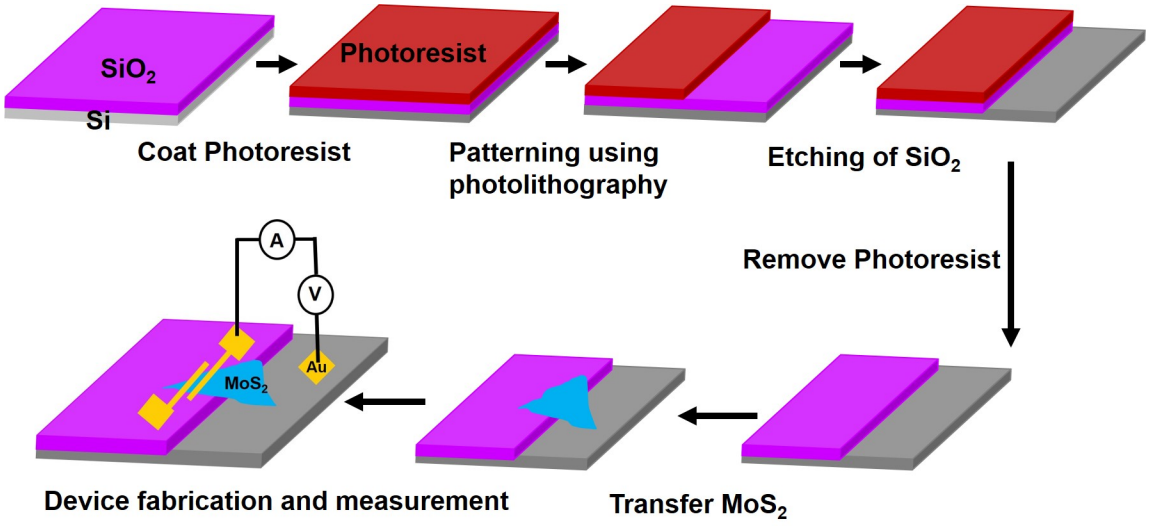

Figure 5.2: Schematic of the steps involved in patterning the SiO_2/Si substrate and subsequent transfer of monolayer MoS_2 to form the Si- MoS_2 heterostructure.

5.3 Results and discussions

5.3.1 Optical Characterisation

Figures 5.3(a) and 5.3(b) show the FESEM and optical microscope image, respectively of a typical monolayer MoS_2 transferred over the patterned SiO_2/Si substrate forming the heterostructure. The image shows that the transferred film is uniform and continuous without any tear due to the transfer process. Photoluminescence and Raman spectra in Figure 5.3(c) and 5.3(d), respectively were used to characterize the MoS_2 synthesized using CVD before and after transferring to the patterned substrate. Raman spectra (Figure 5.3(d)) shows two prominent peaks at 380.2 cm^{-1} and 400 cm^{-1} corresponding to in-plane (E^1_{2g}) and out-of-plane (A_{1g}) vibrational modes. A difference of 19.8 cm^{-1} between the modes confirms the formation of monolayer MoS_2.[254]

The E^1_{2g} and A_{1g} modes get slightly shifted to 380 cm^{-1} and 399.9 cm^{-1} re-

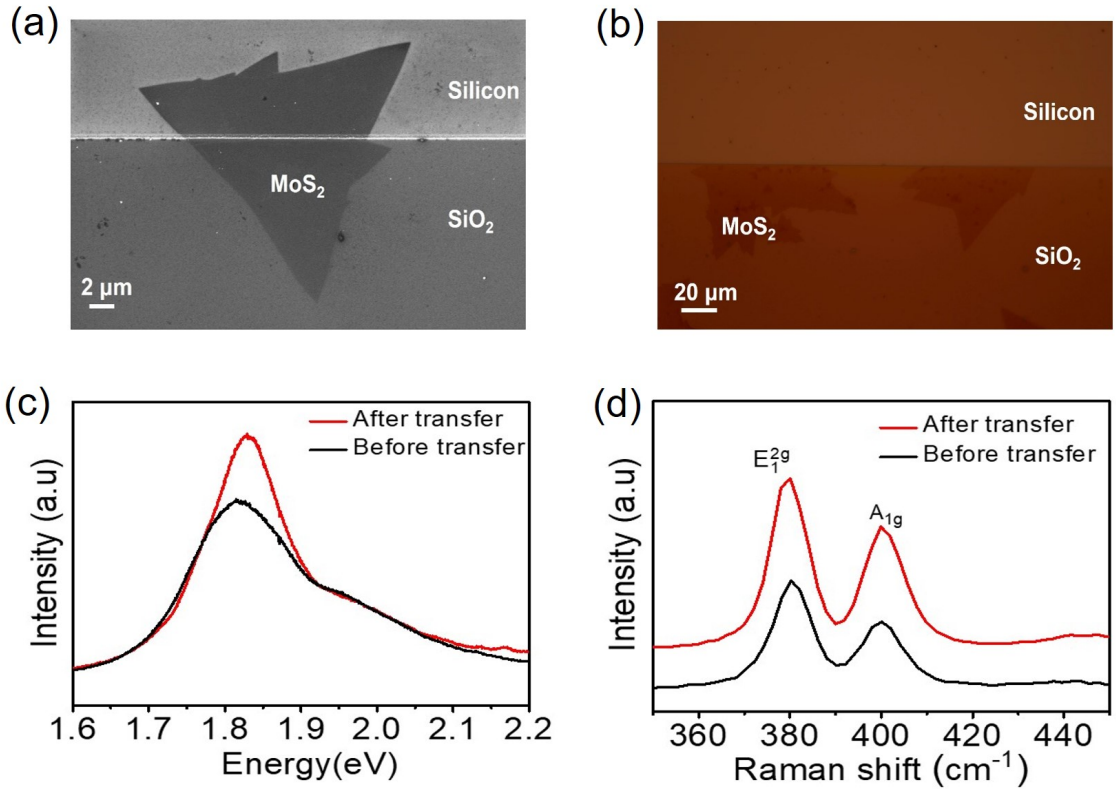

Figure 5.3: (a) FESEM and (b) Optical microscope images of the silicon– MoS_2 heterostructure. In the optical image monolayer MoS_2 is only visible on the SiO_2 part. (c) Photoluminescence (PL) and (d) Raman spectra of as-grown monolayer MoS_2 before and after transferring on to the patterned substrate.

spectively after transferring to the patterned substrate. PL measurements (Figure 5.2(d)) show a strong signal at 1.81 eV corresponding to the A1 exciton peak and a small B1 excitonic peak at 1.95 eV.[254] After transfer, the peak position of the A exciton slightly shifts to 1.82 eV and the peak intensity increases. The shifts in both Raman and PL spectra can be attributed to the release of the tensile strain during the transfer process, which was built in the as-grown material due to the mismatch in the thermal expansion coefficient of MoS_2 and Si/SiO_2.[255] Hence the pretransfer quality of the MoS_2 flakes is retained and preserved after the transfer process.

5.3.2 Electrical Characterisation

The I–V characteristics in the absence of light show strong rectifying diode behavior (Figure 5.4(a)). When illuminated with a 535 nm LED of intensity 2 mW cm^{-2}, significant photocurrent was observed (Figure 5.4(a)). The device has an area of approximately 0.019 mm^2. In conventional (bulk) p–n junction, a wider depletion region and an enhanced electric field in the reverse bias results in a higher photocurrent due to the photogenerated carriers, whereas a narrow depletion region, results in a negligible photocurrent in the forward direction. In the case of the vdW heterostructures, no such depletion layer forms and the band structure of the individual materials remains intact whose relative position decides the nature of the I–V characteristics.[98] The CVD-grown monolayers of MoS_2 are n-type and it forms a type-II heterojunction with p-silicon.[256] To ensure that the observed behavior is from the heterojunction and not from the contacts, we made separate devices across the MoS_2 as well as silicon using similar contact materials and measured the I–V characteristics ((Figure 5.4(b,c))). The linear and symmetric I–V curve across both the devices confirms that the asymmetric I–V characteristic is from Si–MoS_2 due to the presence of van der Waals p–n junction. Using the conventional p–n junction diode equation, we estimate an ideality factor of 2.9. Based on the diode equation, ideality factor is one when the carrier recombination is direct bimolecular (Langevin) type and the value becomes two for trap-mediated (Shockley–Read–Hall) recombination.[97, 98, 249] Ideality factor greater than two is predicted for Schottky diode with a distribution of barrier height.[257] For vdW p–n junction the large ideality is often observed and is probably related to the accumulation of charge carrier due to the low mobility of the materials.[249, 258, 259]

The potential barrier (ϕ_b) of Si– MoS_2 heterostructure was calculated from the dark I-V curve using the thermionic emission theory of charge carriers over a poten-

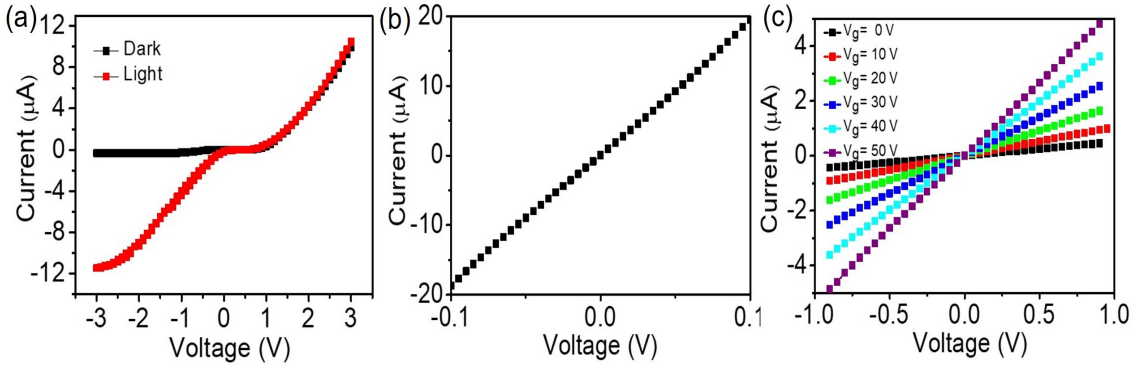

Figure 5.4: (a) I–V characteristics of the Si–MoS_2 heterostructure in the absence and presence of light (535 nm LED of intensity 2 mW cm^{-2}. The reverse current increases in the presence of light with a nearly constant forward current exhibiting a photodiode-like behavior. (b) I-V characteristics of a device fabricated on silicon with gold contacts. (c)Gate dependent I-V characteristics of a device fabricated on MoS_2 with gold contacts.The linear and symmetric I–V characteristics confirm the formation of nearly Ohmic contacts at the MoS_2-Au and silicon-Au interface and hence the nonlinear I–V characteristics of the Si-MoS_2 heterostructure is due to the formation of the p-n junction.

tial zero-bias barrier.[242, 243, 244, 103, 260, 256]

$$\emptyset_b = \frac{k_B T}{q} \ln\left(\frac{AA^*T^2}{I_s}\right) \tag{5.1}$$

Where A is the area of the active device, is the Richardson's constant (for p-type silicon), T is the temperature, I_s is the reverse saturation current, k_B is the Boltzmann constant and q is the electron charge. Following the same, we get a potential barrier ϕ_b of 0.549 eV which is similar to earlier reports.[256]

5.3.3 Temperature dependent study

To further character ze the Si– MoS_2 p–n junction and to rule out the contribution of Schottky barrier for the observed photoresponse, we did temperature-dependent measurements. The forward bias dark current was found to be indepen-

dent of temperature (Figure 5.5(a)). This rule out the contribution of the Schottky barrier in determining the observed I–V characteristics. In the case of van der Waals p–n junction, the forward current is governed by tunneling-mediated interlayer recombination.[97, 98, 249] We found that under the dark condition the reverse bias current increases with increasing temperature (Figure 5.5(a,b)).

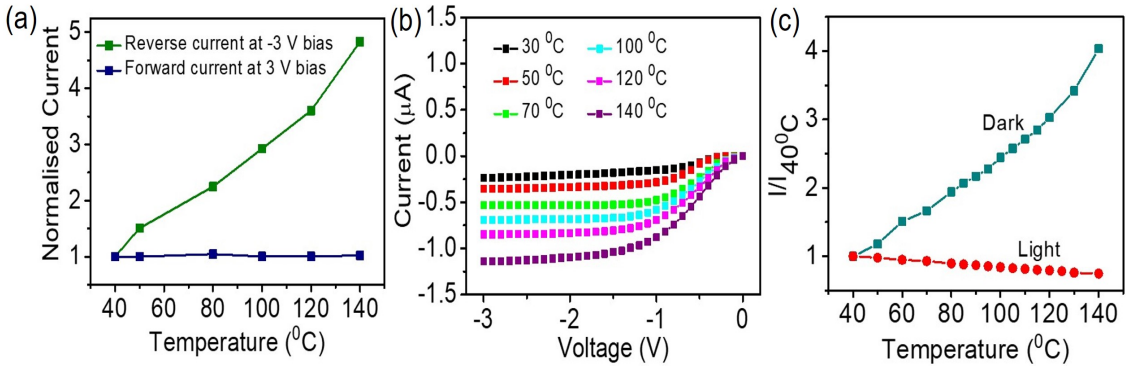

Figure 5.5: (a)Dark current (normalised by 40 ℃ value) for 3V reverse and forward bias. While the reverse current increases with temperature, the forward bias current does not show any significant temperature dependence. (b) Reverse bias dark I-V characteristics measured in the temperature range from 30 ℃ to 140 ℃. (c) Temperature-dependent current at an applied reverse bias of -3 V in dark and in the presence of light. With increasing temperature dark current increases and the photocurrent decreases.

In the reverse bias, electrons and holes encounter a higher energy barrier. With increasing temperature, more and more carriers gain sufficient energy to cross the barrier and produce more current. Thermally generated carrier number increases rapidly with increasing temperature. As a result, even though the carrier scattering due to lattice vibration increases, the overall current increases. Whereas, in the presence of light, current decreases with increasing temperature (Figure 5.5(c)). Due to the efficient absorption of light by the Si– MoS_2 heterostructures, a large number of photogenerated charge carriers are available in the system and the contribution of thermally generated carriers are not significant. So the overall number of carriers taking part in conduction does not change significantly with increasing

temperature. But the carriers experience enhanced scattering due to the increase in the lattice vibration with increasing temperature. As a result, the photocurrent decreases with increasing temperature. This result provides important information about the efficient generation of photoexcited carriers.

5.3.4 Time resolved photoresponse

Time-resolved photoresponse (Figure 5.6) of the devices showed a relatively faster response with a rise time of 49 µs and fall time of 77µs. The electron-hole pairs generated at the junction efficiently tunnel across the barrier of the p–n junction. The faster rise and fall time indicates a faster and more efficient electron-hole separation at the junction.

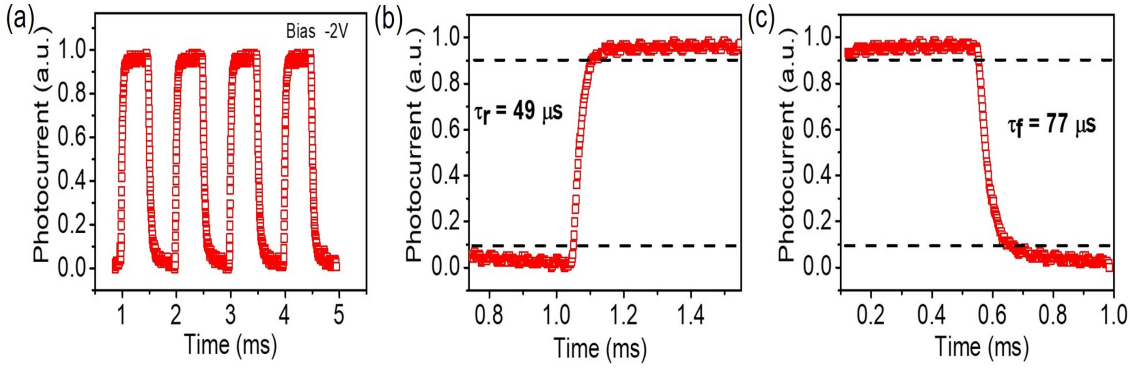

Figure 5.6: (a)Time-dependent photocurrent under the illumination of a 535 nm LED with intensity 2 mW cm^{-2} at a bias of -2 V. (b) Rise time and (d) fall time indicating a faster rise and fall time.

5.3.5 Optoelectronic studies

To further understand the interface quality, an intensity-dependent photoresponse study (Figure 5.7(a)) using a 465 nm LED was done. It is important to mention

that the qualitative nature of the device characteristics remains the same regardless of the wavelength of the LED used. The photocurrent increases with intensity and the data is fitted using a power law,

$$I \propto P^{\alpha} \tag{5.2}$$

where $\alpha = 1$ indicates a junction with low trap states.[242] We obtained a value of 0.95 ± 0.3 for α, which is indicative of the formation of a good junction with very low trap states at the junction interface.

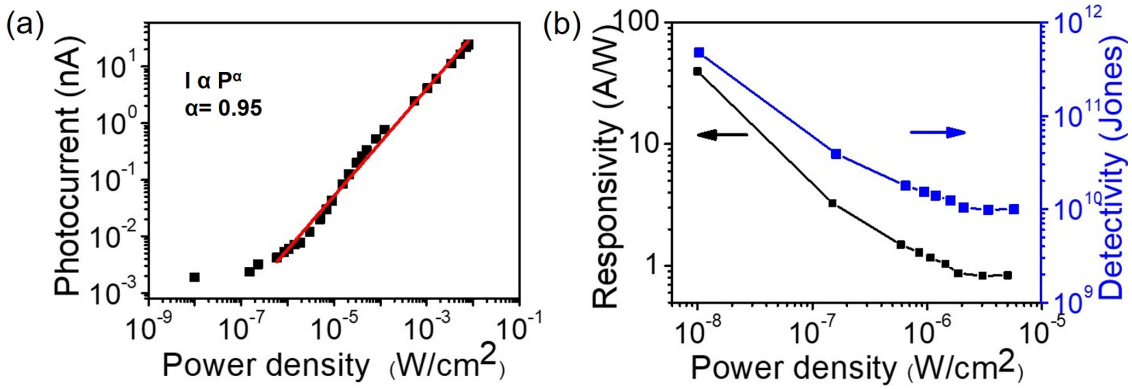

Figure 5.7: (a) Plot showing the dependence of photocurrent with an incident light intensity of the heterojunction when illuminated using a 465 nm LED. The data points are fitted well by the power law. (b) Responsivity and detectivity as a function of the power density of an incident wavelength of 465 nm. Both the responses were measured at an applied reverse bias of 3 V.

Responsivity and detectivity are two important figures of merit that evaluate the performance of photodetectors. Both responsivity and detectivity (Figure 5.7(b)) decrease with increasing power density. This is because of the presence of trap states at the interface.[242, 256] At lower power density of incident light, electrons are trapped by the trap states, resulting in reduced recombination and increase in hole lifetime leading to higher R and D. As the power density increases the number of available trap states decreases resulting in the saturation of photoresponse.[242]

At an incident intensity of 10 nW cm^{-2}, a detectivity of 4.7 $\times$ 10^{11} Jones and responsivity of 39.7 A W^{-1} was obtained. Reasonably high values of detectivity and responsivity obtained indicate the efficiency of the device as a photodetector.

5.4 Effect of dielectric environment

To explore the change in optoelectrical properties of silicon– MoS_2 heterostructure with the dielectric environment we used various solid (hBN, PVDF-TrFe) and liquid (silicone oil, anisole, novec, IPA, ethanol, water, etc.) dielectric materials. First, we encapsulate the device with a ferroelectric polymer, PVDF-TrFe (70:30 mol %). To understand the electrical performance of the device, the reverse I–V curve in the absence and presence of light (535 nm LED), before and after coating PVDF-TrFe was measured (Figure 5.8 (a)). The photocurrent shows a significant enhancement and the barrier potential, calculated from the dark I–V, decreased from 0.66 to 0.55 eV after coating PVDF-TrFe. The relative magnitude of enhancement of current in the presence of light after the coating was much higher than that under dark conditions. This is an indication of the efficient separation and contribution of photocarriers toward the total current. In the presence of a high dielectric environment, the photocurrent keeps increasing under the increasing reverse bias (Figure 5.8(a)). This unsaturating behavior indicates an inefficient extraction of the photogenerated charge carriers.[249] This effect is more prominent in the presence of higher dielectric materials (discussed later).

To get a better understanding of the improved photodetection capability of the device, we determined the responsivity of the device with and without PVDF-TrFe coating. Responsivity is higher at lower wavelengths (Figure 5.8(b)), and it decreases with increasing wavelength. Beyond 730 nm, responsivity drops to less than 1 A W^{-1}. The curve shows three prominent peaks at 609, 660, and 430 nm corre-

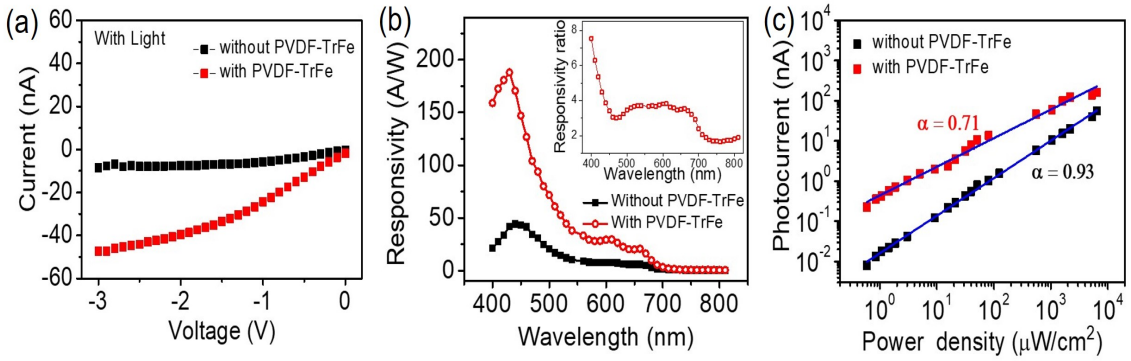

Figure 5.8: (a) Reverse bias I–V characteristics in the presence of light before and after coating PVDF-TrFe. (b) Responsivity as a function of different wavelengths in the presence and absence of PVDF-TrFe coating. The responsivity ratio with and without PVDF-TrFe coating has been shown as a function of wavelength in the inset. (c) The photocurrent is shown as a function of power density when illuminated with a 465 nm LED at an applied reverse bias of 3 V in the presence and absence of PVDF-TrFe coating (blue line indicates linear fitting).

spond to A1, B1, and C excitons of MoS_2, respectively.[261] Hence, the contribution from MoS_2 dominates the responsivity, which is expected due to the choice of highly doped Si. As monolayer MoS_2 is a direct band gap semiconductor, it can absorb light more efficiently compared to indirect band gap materials. Hence any modification in the properties of MoS_2 due to the change in the dielectric environment gets reflected in the photocurrent. The responsivity curve peaks around 430 nm with the responsivity increasing from 42 A W^{-1} in the absence to 188 A W^{-1} in the presence of PVDF-TrFe, giving a 4.5 times enhancement. It is evident that responsivity exhibits significant enhancement at lower wavelengths in the presence of PVDF-TrFe coating (see inset of Figure 5.8(b)). It has been predicted that deep-level defect states can get effectively screened by a high dielectric environment and the level becomes shallow as a result the carriers can easily get delocalized and take part in electrical transport increasing the conductivity significantly.[2] Without the high dielectric environment, the low photoresponse in the low wavelength regime indicates that a significant portion of the photogenerated carriers get trapped by the deep defect lev-

els in the pristine device. Whereas, in the presence of a high dielectric environment the trap becomes shallow and the photogenerated carriers get efficiently collected increasing the responsivity significantly (Figure 5.8(b) inset). Transient photoresponse in the presence and absence of a high dielectric constant environment also supports this observation (Figure 5.9).

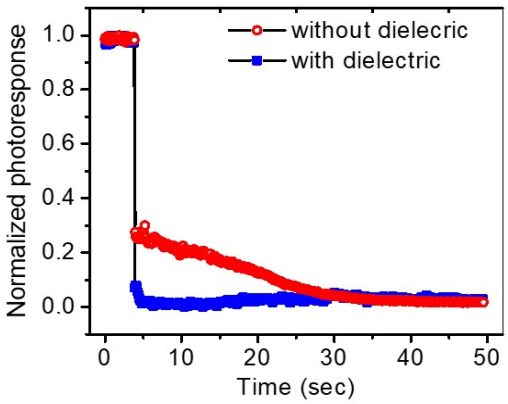

Figure 5.9: Normalized photoresponse is shown for devices with and without a high dielectric environment (here, Novec). From the data, it is clear that in the presence of a large dielectric constant environment, the temporal response is faster, and the slow part is absent.

When deep-level trap states are present, after turning off the illumination, the release of carriers happens very slowly. After the initial fast response, we found a very slow temporal response in the absence of any high dielectric environment (Figure 5.9). This slow temporal response indicates the presence of deep-level trap states.[262, 215] We found that when the sample is placed in a large dielectric constant environment the slow temporal response is absent (Figure 5.9). The photocurrent maintained its linear dependence with a power density (Figure 5.8(c)) in the presence of PVDF-TrFe coating but with a lower exponent value. The exponent in the power law $I \propto P^{\alpha}$ changes from 0.93 in the absence to 0.71 in the presence of PVDF-TrFe coating. Due to the enhanced screening by the environment dielectric, photogeneration of charge carriers becomes efficient. Hence, with increasing light in-

tensity, there will be large number of photogenerated carriers available in the device. However, due to the relatively low mobility of the 2D materials these photogenerated charge carriers pile up, hence carrier recombination will increase with increasing light intensity, which will cause the low value of the exponent.

5.4.1 Effect of varying the dielectric environment

To explore the effect of other dielectrics, we have taken various liquid dielectric media like hexane (ε_r = 1.88), silicone oil (ε_r = 2.3), toluene (ε_r = 2.38), anisole (ε_r = 4.3), Novec 7100 (ε_r = 7.4), isopropyl alcohol (IPA) (ε_r = 18.3), ethanol (ε_r = 24.6), ethylene glycol (ε_r = 37), and deionized water (ε_r = 80). Si– MoS_2 p–n junctions were exposed to these dielectrics and their I–V characteristics were studied in the presence and absence of light. After every measurement, the devices were washed in acetone and IPA and checked to ensure that they maintain their initial characteristics. There was no visible bubble formation while using water as a dielectric which eliminates the possibility of any hydrogen evolution reaction. To avoid any error, contribution of conductivity of the medium, has been subtracted (Figure 5.10(c)) from the total current. To measure the conductivity of the liquids, we made a device (Figure 5.10(a)) with the same device dimensions as the main device (Figure 5.10(b)) under study on the same chip, without MoS_2 so that no silicon –MoS_2 heterostructure is formed. The dielectrics were chosen such that they do not absorb any significant portion of the incident wavelengths.[263, 264, 265, 266]

Figure 5.11(a) shows the ratio of photocurrent (with respect to air) as a function of reverse bias voltage for various dielectric media. It is evident that for a fixed bias voltage, the photocurrent increases with the increasing dielectric constant of the environment. Also, for a particular medium, the photocurrent increases with increasing reverse bias. This unsaturating behavior is observed for both solid and liquid dielec-

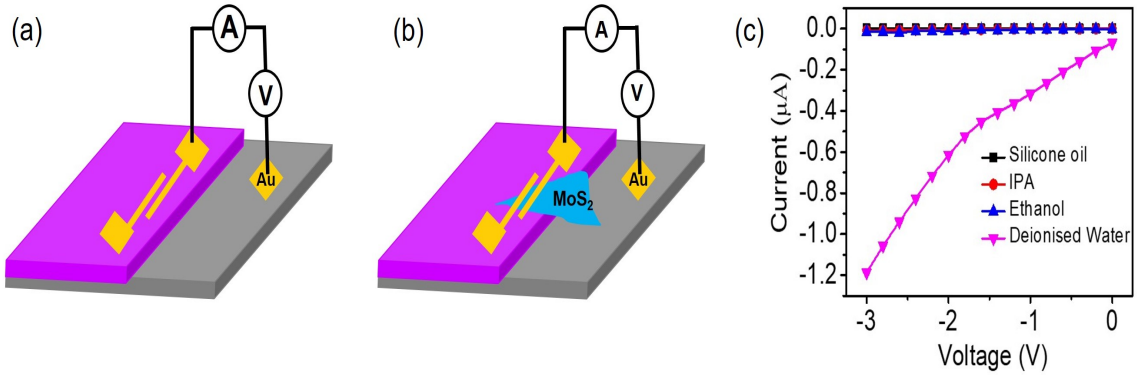

Figure 5.10: (a) Device geometry of the test device used for measuring the conductivity of the liquid dielectric mediums without MoS_2. (b) Device geometry of the silicon- MoS_2 heterostructure (c) I-V curve showing the current as a function of voltage passing through various liquid mediums alone.

tric but it is more pronounced for the higher dielectric constant environment.[249] We observed nearly three orders enhancement of photocurrent in the presence of a higher dielectric environment at 3 volt reverse bias (Figure 5.11(b)).

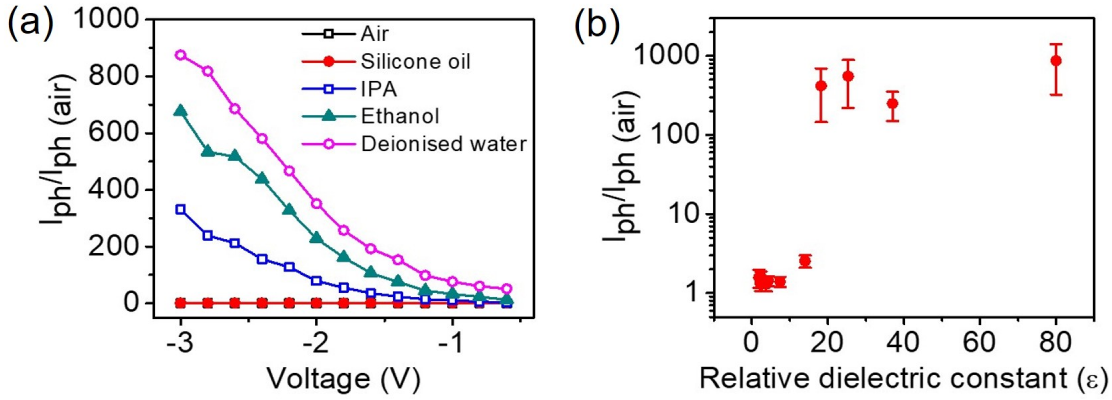

Figure 5.11: (a) Ratio of reverse bias photocurrent in the presence of various dielectric mediums shown as a function of bias voltage. (b) Enhancement of photocurrent shown as a function of relative dielectric constant with respect to air for -3 volt bias

This enhancement in current in the presence of a dielectric environment can be explained due to the combined effect of various phenomena. In 2D materials due to a lack of screening in the out-of-plane direction, the photogenerated electron-

hole pair remains strongly bound and forms an exciton with large excitonic binding energy. As a result, the carriers cannot contribute to the charge transport which demands delocalization of the carriers. In the presence of a high dielectric environment, the screening becomes efficient and excitonic binding energy decreases significantly hence the photogenerated carriers can easily get separated and contribute to the current.[267, 268] We do not expect any other factors like doping to contribute to this enhancement. We have used non-ionic liquids to avoid any contribution due to doping. As reported earlier [36], these liquids do not produce any doping of the sample. The water used in the experiment was deionized water. We have taken the Photoluminescence spectra of MoS_2, in the presence and absence of deionized water. (Figure 5.12) We observed that the PL peak position of the neutral A1 exciton peak shifts from 1.81 eV in the air to 1.87 eV in the presence of water. Such a large shift cannot be explained by a change in doping.[269] Hence we do not expect doping due to any of the liquids used as the dielectric.

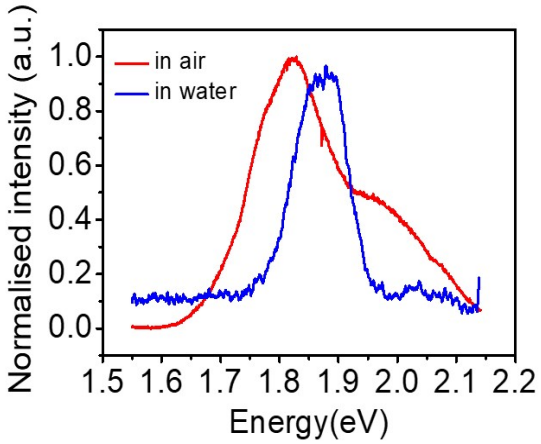

Figure 5.12: Photoluminescence spectra of monolayer MoS_2 in the presence and absence of deionised water

We do not expect any doping from PVDF-TrFe either, as any kind of doping contribution can be inferred from the shift in the A_{1g} peak in the Raman spectra. We did not observe any shift in the Raman peak position after PVDF-TrFe deposition

consistent with the previous report.[270]

We have corroborated our experimental hypothesis of reduced exciton binding under high dielectric environment improved photocurrent, using DFT calculations (done in collaboration with Chandan and Dr. Mukul Kabir, IISER Pune). Heterostructures of MoS_2/h-BN and MoS_2/HfO_2 that minimize the interfacial strain were designed and investigated exciton binding in the MoS_2-layer. The exciton binding energy of monolayer MoS_2 in the absence of any medium was calculated to be 488 meV and the direct band gap was predicted to be 2.12 eV at the K-point. Dielectric environment improved electron screening in the monolayer MoS_2, and should affect exciton binding in MoS_2/h-BN and MoS_2/HfO_2 heterostructures. While the direct gap at the K-point is unaffected in these heterostructures, a rigid shift in valence and conduction band is observed. In MoS_2/h-BN, the valence and conduction band shifts by $\Delta_{VB} = 0.82$ eV and $\Delta_{CB} = 0.80$ eV in energy and the exciton binding energy reduces to 432 meV . Improvement in the electron screening slightly reduces E_b in the MoS_2/h-BN, which is consistent with the experimental results on encapsulated MoS_2.[271] We also observed that in the presence of hBN the enhancement of photocurrent compared to air is only 30 % (Figure 5.11(b)). The overall trend in the electronic structure remains the same in MoS_2/HfO_2 heterostructure. But the valence and conduction bands get shifted by $\Delta_{VB} = 0.92$ eV and $\Delta_{CB} = =$ 0.91 eV. However, the exciton binding energy is greatly renormalized to 94 meV in MoS_2/HfO_2 due to the high dielectric nature of HfO_2. In our experiment presence of a medium with a relative dielectric constant of nearly 20 shows more than 400 times enhancement in photocurrent (Figure 5.11(b)). Therefore, under a high-dielectric environment, the exciton binding in the MoS_2 layer becomes weaker, which in turn helps to generate free carriers and increases the photocurrent.

The presence of a dielectric can also affect the electronic bandgap as the change in the electron-electron and electron– hole Coulomb interactions cause bandgap

renormalization.[33, 36, 272, 273] A steady decrease in electronic bandgap energy with an increase in dielectric screening [35, 42] has been predicted in TMDs using ab initio calculations.[33, 37, 274, 275, 276, 277] This change in the fundamental electronic bandgap of MoS_2 would change the overall band alignment of the heterostructure. A decrease in bandgap would result in a smaller potential barrier at the junction. This lowering of tunnel barrier height would allow more carriers to cross the junction, which results in a sharp increase in current. A higher dielectric environment will also screen the long-range Coulomb interaction due to the charged impurities [56, 51, 278, 217] which helps in the reduction of scattering of carriers. Thus, the photogenerated carriers can travel easily and contribute to the current enhancement. The abundance of photogenerated carriers in the high dielectric medium explains the non-saturating behavior of photocurrent. Due to the relatively low mobility of these materials, the charge carriers cannot move easily, and with increasing bias voltage, more and more carriers reach to the contacts. As a result, photocurrent shows an increasing trend without saturating.

5.5 Summary

In this chapter, we have successfully improved the photoresponse of a silicon monolayer MoS_2 mixed dimensional vdW heterostructure by nearly three orders of magnitude by controlling the environment dielectric constant. Our study helps in understanding how the surrounding dielectric environment influences the charge transport and optoelectronic properties of 3D–2D vdW hybrid device and shows the importance of a dielectric environment in modulating the properties of 2D materials. Medium with higher dielectric permittivity provided better screening of Coulomb interaction between charge carriers. As a result, the excitonic binding energy decreases, which helps in separating the photogenerated charge carriers, and the photocurrent

increases significantly. A high dielectric environment also screens the impurity's potential, thereby reducing the scattering of charge carriers and contributing to higher conductivity. The dielectric environment also changes the overall bandgap of the heterostructure and provides a lower energy barrier for the charge carriers. Due to the tunneling-mediated charge transfer between the adjacent layers in vdW heterostructures, most of them suffer from very low efficiency. Our study shows the profound effect of environment dielectric on the optoelectronic properties of the atomically thin 2D semiconductors and demonstrated a facile way to significantly improve the device's efficiency.

Chapter 6

Role of Defects on the Transport Properties and Photoresponse of Silicon-MoS_2 Heterostructure

This chapter is an adaptation of the research article published in "ACS Applied Electronic Materials, 4, 12, 6038–6046, 2022 "

6.1 Introduction

Studies of heterostructures based on 2D materials have generated a great deal of interest due to their excellent optoelectronic properties as well as their versatility in integrating with different dimensional materials, including semiconducting industry pioneers like silicon, III-V materials, and related compounds.[100, 84] Due to the interlayer vdW interactions, 2D materials are free from dangling bonds which are a major source of surface recombination and circumvents the problem of lattice mismatching in heterostructures.[100] Also, a mixed dimensional vdW heterostructure can offer greater optical absorption cross section and charge separation overall 2D heterostructure, making mixed dimensional vdW heterostructure promising for applications in optoelectronics, photonics, and energy harvesting technologies.[84]

Combining 2D TMDs with mature silicon technology can compensate for the drawbacks of silicon and overcome the compatibility issues due to lattice mismatch.[100, 279] The combination of TMDs and silicon is particularly interesting because of the

excellent compatibility of silicon with the existing CMOS process and the possibility of silicon acting both as a substrate and an active component with promising performance.

Several optoelectronic devices based on silicon and 2D TMDs have been reported with broad operation wavelength bands.[100] But often, defects present in the device can cause inevitable recombination.[260] These defects can contribute to the recombination of optically injected electrons and holes, reducing the quantum efficiencies.[280, 281] A large surface-to-volume ratio and reduced thickness make 2D TMDs vulnerable to surface defects and potential disorders.[55] Reports have shown the existence of structural defects like vacancies, dislocations, and grain boundaries in CVD grown MoS_2.[212] These defects can act as charge traps and aid in recombining photogenerated charge carriers, reducing the photocurrent.[282] In general, defect states can be a mid-gap state or band tail state. Mid-gap states favor charge carrier recombination (Shockley-Read Hall type), whereas a band tail state act as an electron or hole trap state depending on its proximity to conduction or valence band edges.[283] Through optical and THz pump-probe experiments, it was shown that in WS_2, photogenerated charge carriers get annihilated by the mid-gap states within a lifetime of 1ns.[283] Hence defects can be detrimental to the performance of optoelectronic devices based on 2D TMDs. Regardless of the number of reports demonstrating the photoresponse in silicon-TMD heterostructures, there is a lack of comprehensive understanding of the temperature-dependent photoresponse and how the defects present in 2D TMDs affect the heterostructure's photoresponse.

In this chapter, we investigate the temperature-dependent electrical characteristics and photoresponse of a p-n junction formed between silicon-MoS_2 mixed dimensional vdW heterostructure and identify the contribution of defects and charged impurities in limiting the photoresponse. The temperature variable current-voltage measurement demonstrates a space charge-limited conduction with an exponen-

tial distribution of trap states. The heterostructure also exhibited a high and temperature-dependent ideality factor, which was explained by the generation recombination model. The intensity-dependent photocurrent's temperature dependency reveals a change from bimolecular to monomolecular recombination. The photoresponse relaxation times were calculated from the time-resolved photoresponse measurement and were observed to increase with temperature. Various defect states and charged impurities present in the device act as recombination centers and scatterers, degrading the photoresponse. These defect states can be effectively screened and the strength of the Coulomb interactions be weakened by modifying the surrounding dielectric environment. In the previous chapter we have seen how, a three-order enhancement in photoresponse was achieved by modulating the surrounding environment. In this chapter, we show that the effect of this dielectric environment is more prominent towards low temperatures. A thin layer of a ferroelectric polymer namely, poly (vinylidene fluoride–trifluorethylene) (PVDF-TrFe) ($\varepsilon_r = 14$) is deposited over the heterostructure to modify the surrounding dielectric environment, which enhanced the photoresponse and effectively suppressed the noise levels in the heterostructure.

6.2 Experimental details

P-type silicon substrate with 300 nm thermally grown SiO_2 was patterned using photolithography and the SiO_2 layer was selectively etched to obtain a clean p-type silicon surface. To prevent large under-etching and to get a nearly vertical SiO_2 sidewall, 200 nm SiO_2 was initially removed by reactive ion etching followed by removing the remaining 100 nm using wet etching.[284] The freshly etched silicon surface was then dipped in a 1 % Hydrofluoric acid (HF) aqueous solution to obtain a dangling bond-free hydrogen-terminated silicon surface.[253] CVD grown [285, 286]

monolayer MoS_2 was transferred to this patterned substrate using polystyrene assisted wet transfer method.[287] 5nm/65nm Cr/Au deposited on MoS_2 by thermal vapor deposition served as one of the electrodes for electrical measurements while the second electrode was taken from the back side of silicon using silver paint. Measurements were done in a cryo-free closed-cycle cryostat (Janis research) from room temperature (300K) down to 12K. To modify the dielectric environment, 5 % solution of PVDF-TrFe (70:30) dissolved in Methyl ethyl ketone (MEK) was spin-coated at 2000 rpm for 120s. The film was then heated at 70 ℃ for 1 hour to evaporate the solvent and then heated at 140 ℃ for 3 hours for crystallization.

6.3 Results and discussions

Figure 6.1(a) shows the optical microscope image of monolayer MoS_2 transferred on the patterned silicon substrate to form the silicon-MoS_2 heterostructure. The FESEM image (Figure 6.1(b)) shows the transferred MoS_2 is uniform and continuous without any damage during the transfer. The number of layers of MoS_2 was determined using Raman spectroscopy (Figure 6.1(c)). The characteristic Raman peaks for the E^1_{2g} and A_{1g} vibration modes appeared at 386.7 cm^{-1} and 406.5. cm^{-1} .The difference between the peak positions is 19.6 cm^{-1}, comparable to the reported values for monolayer MoS_2.[199]

6.3.1 Electrical Characterisation

The electrical measurements were performed by applying a positive voltage to the silicon contact and negative voltage to the MoS_2 contact. The current- voltage (I-V) characteristics (Figure 6.2(a)) show good rectifying behavior with a rectification ratio of nearly 10^2 at $\pm$ 2 V, confirming the formation of a p-n junction. The linear

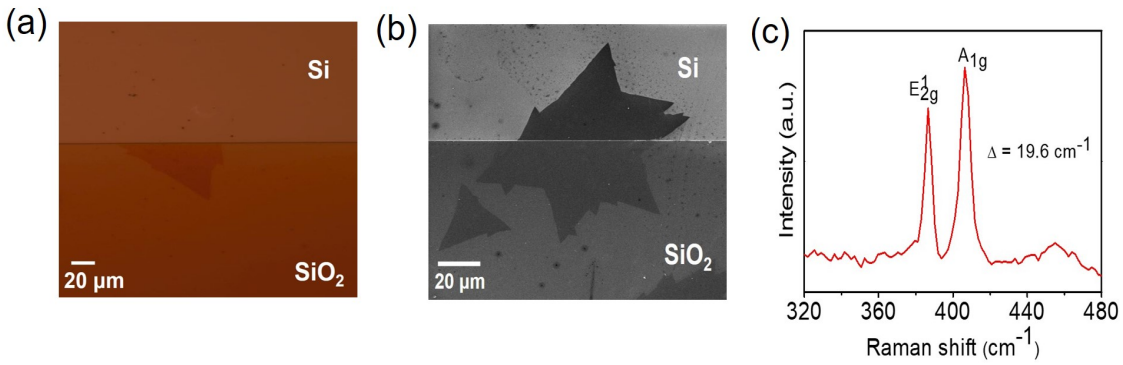

Figure 6.1: (a) Optical microscope image and (b) FESEM image of a monolayer MoS_2 transferred onto a patterned Si/ SiO_2 substrate. (c) Raman spectrum of monolayer MoS_2.

I-V characteristics obtained from the Au/MoS_2/Au device (Figure 6.2(b)) proves that the rectification behavior is originating from the p-n junction formed between silicon and MoS_2 and not from the Au/MoS_2 contact. A dark current of 0.18 µA was obtained at a reverse bias of 2 V, which enhances by 30 times upon illumination under 630. nm light of intensity 2 mW cm^{-2}. The measured device had an effective area of 44 μm^2. The ideality factor of the the device was extracted from the dark

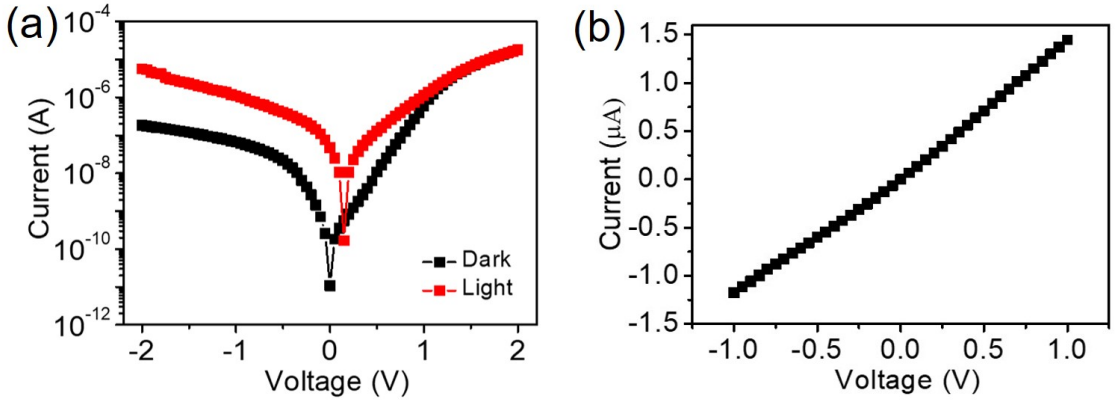

Figure 6.2: (a) *I-V* characteristics of silicon-MoS_2 p-n junction in the absence and presence of light. An asymmetric *I-V* curve with a rectification ratio of nearly 10^2 at ± 2 V was obtained. At a reverse bias of 2 V, the current enhances by 30 times upon illumination under 630.nm light of intensity 2 mW/cm^2 (b)*I-V* characteristics (under dark conditions) measured across MoS_2 using Cr/Au as contact electrode.

I-V characteristics using the equation [242]

$$\mathrm{n} = \frac{\mathrm{q}}{\mathrm{k_B}T}\frac{\mathrm{dV}}{\mathrm{d\,ln\,I}} \tag{6.1}$$

(where q is the unit charge, k_B is the Boltzmann's constant, T is the absolute temperature, and $\frac{\mathrm{dV}}{\mathrm{d\,ln\,I}}$ is the inverse slope of the semi-log I–V curve in the forward bias direction) was around 4.4. This value is much higher than that of an ideal diode (n=1). Van der Waals heterostructures with trap states at the interface usually exhibit high ideality factors.[288, 289, 290] Often, these interface states are present due to structural defects or sulfur vacancies in CVD-grown MoS_2 [291], or any non-ideality of the silicon surface [292] etc.

The potential barrier height of the heterojunction can be deduced from the I-V curve in the dark and could be described by the thermionic emission theory of majority charge carriers over a zero bias barrier from the silicon to MoS_2 [256]

$$\emptyset_b = \frac{k_B T}{q}\ln\left(\frac{AA^*T^2}{I_s}\right) \tag{6.2}$$

Where A is the area of the active device, is the Richardson's constant (for p-type silicon), T is the temperature, $\mathrm{I_s}$ is the reverse saturation current, $\mathrm{k_B}$ is the Boltzmann constant and q is the electron charge. Following the same, we get a potential barrier ϕ_b of 0.5 eV.

A deeper insight and an in-depth understanding of the conduction mechanism and carrier dynamics in the silicon-MoS_2 p-n junction can be attained from temperature-dependent measurements. The temperature-dependent I-V characteristics (Figure 6.3(a)) showed that the reverse bias current increases with increasing temperature. This is mainly due to the thermal generation of electron-hole pairs in the p-n junction. The rectification ratio (ratio of forward to reverse current at a particular bias), calculated at 2 V bias, decreased with an increase in temperature (figure 6.3(b)).

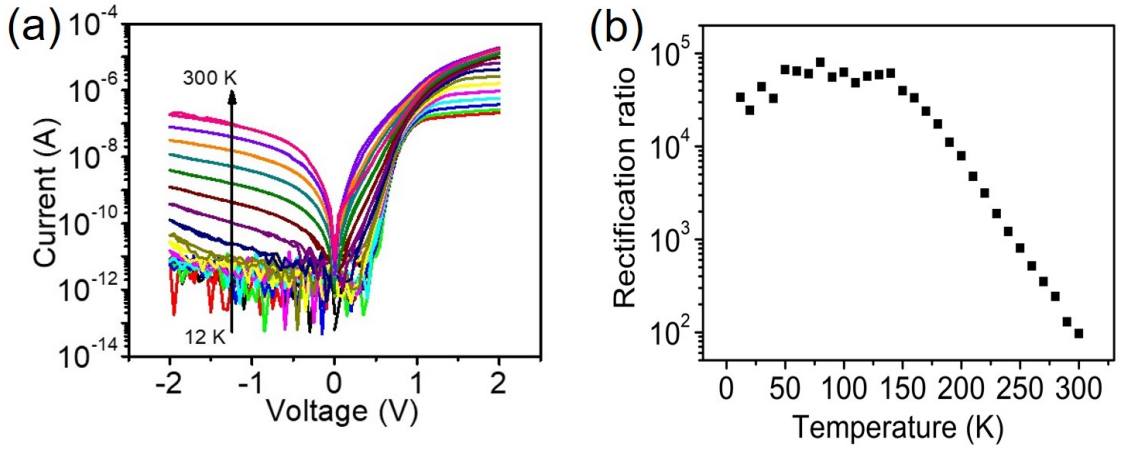

Figure 6.3: (a) Temperature-dependent dark I-V characteristics (b) Rectification ratio measured at 2 V as a function of temperature.

6.3.2 Temperature dependence of ideality factor (n)

The ideality factor (n) is found to decrease with increasing temperature (Figure 6.4(a)). A value of n greater than 2 implies that the current transport is dominated by some mechanism other than diffusion-recombination.[293] The increase in ideality factor with a decrease in temperature could be due to a tunneling effect.[294] The current transport will be dominated by tunneling-enhanced recombination via deep defect levels at the heterojunction interface.[294] To explain the observed temperature dependence of n, we invoke the generation-recombination model. According to this model, the temperature dependence of n, suggests the involvement of defect states in carrier generation recombination. The temperature dependence of n is modeled as[295]

$$n = n_0 + \frac{T_0}{T} \tag{6.3}$$

Where n_0 and T_0 are constants, which are independent of temperature and bias. The slope and an intercept from the graph between n and inverse temperature gives the value of n_0 and T_0 respectively. A plot of n versus T shows 2 regions, region I (12 K-140 K) can be fitted with equation (3) (Figure 6.4(b)) and we get a small value of

$n_0 \approx 0.187$, indicating the presence of several defect states in the carrier generation-recombination process and a large $T_0 \approx 500$ K, implying the possible contribution of tunneling current.[295] In region II (180 K-280 K), we observe an increase in n with T (Figure 6.4(c)) and can be fitted using a linear function. The slope of this fit is a relatively lower value (0.011) indicating a minimal temperature dependence of n.[296, 294] Larger the ideality factor greater the density of defects/trap states in the device.[289] Hence a decrease in temperature freezes the carriers in the defect states causing the recombination to be limited by these states.[297] Thus we observe an increase in the ideality factor with the decrease in temperature. The increase in the barrier height with temperature can also be ascribed to the contribution of recombination current in the total current.[298]

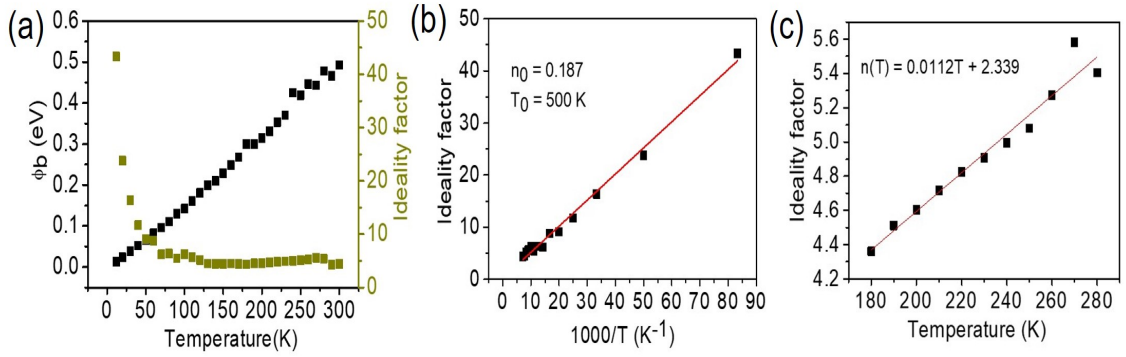

Figure 6.4: (a)Variation of barrier height and ideality factor with temperature. (b)Ideality factor calculated from dark I-V characteristics plotted as a function of inverse temperature and (c) temperature.

6.3.3 Space charge limited current (SCLC)

A log-log plot of forward current versus voltage (Figure 6.5(a) can give further information about the presence and nature of trap states present in the silicon-MoS_2 heterojunction device. The current follows a power law relation, $I \propto V^m$ with the voltage. Such a dependence with the value of m equal to or greater than 2 indicates

the existence of space charge limited current (SCLC). [289, 299, 300] The power law exponent m was calculated for various temperatures in the range 100 K – 300 K and was observed to increase with a decrease in temperature, with values between 4.2-9.8. An exponent m greater than 2 evinces the presence of exponentially distributed charge traps.[289, 300] A plot between m and the reciprocal of temperature (Figure 6.5(b)) can be fitted using a straight line whose slope gives the characteristic temperature, T_c = 1645 K. The characteristic trap energy can be calculated using the relation $E_t = kT_c$, where k is the Boltzmann constant.[299] The obtained value of trap energy 0.14 eV, suggests most of the traps present are deep traps.[299, 300] It has been reported that sulfur and molybdenum vacancies in MoS_2 can introduce deep defect levels.[222]

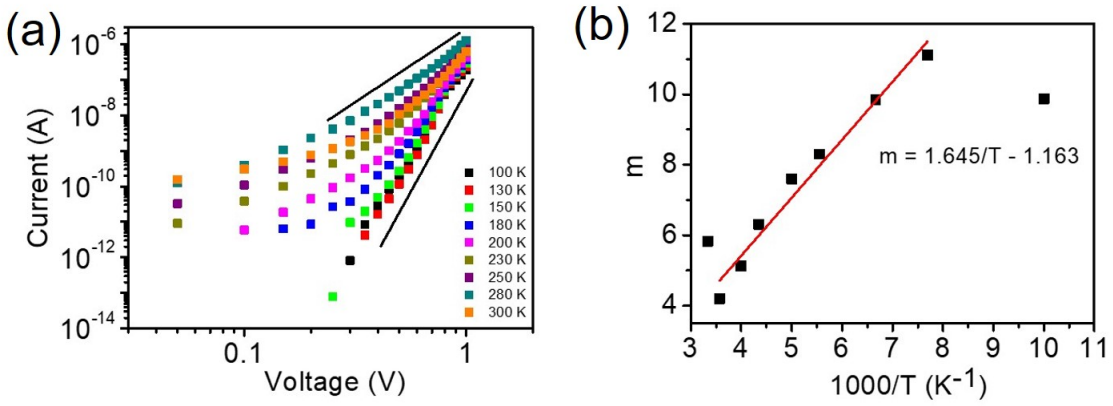

Figure 6.5: (a) Log-log plot of forward current versus voltage of the pristine silicon-MoS_2 p-n junction. (b) Plot of the power law exponent with inverse temperature.

6.3.4 Temperature dependence of photocurrent

The photocurrent (I_{ph}), measured at a reverse bias of 2 V, is observed to decrease with a decrease in temperature and attains nearly a constant value below 50 K (Figure 6.6(a)). Above 120 K up to 300 K, the photocurrent follows a thermally

activated behavior, increasing linearly with temperature. This I_{ph} produced by the thermal activation of photo carriers follows the relation

$$I_{ph} = I_0 \exp \frac{E_a}{kT} \tag{6.4}$$

Where I_0 is a prefactor, k is Boltzmann's constant, and E_a is the activation energy. The value of E_a can be obtained from the slope of the linear fit between log I_{ph} and $\frac{1000}{T}$ and was around 251 meV (Figure 6.6(b)).

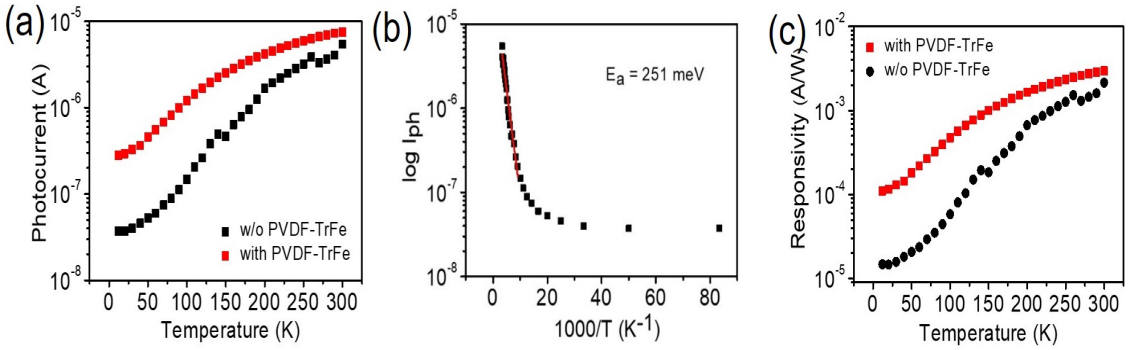

Figure 6.6: (a) Variation of photocurrent with the temperature of the silicon-MoS_2 p-n junction in the presence and absence of PVDF-TrFe at a reverse bias of 2 V.(b) Plot of log of photocurrent versus inverse temperature in the absence of PVDF-TrFe (c) Dependence of responsivity corresponding to (a) with temperature

6.3.5 Photocurrent enhancement with dielectric medium

From the previous chapter, we know that a significant enhancement in photoresponse can be obtained by varying the dielectric environment. In this chapter, we observe that the relative magnitude of this enhancement is more pronounced towards low temperatures (Figure 6.6(a)). A thin layer of PVDF-TrFe has been used to modify the dielectric environment. Nearly more than one order enhancement in photocurrent is observed at low temperatures whose relative magnitude decreases with an

increase in temperature. Correspondingly responsivity also shows a similar trend (Figure 6.6(c)). From these observations, we presume the contribution of defects or any charged impurities present at the interface or the surface to the photoresponse dominates at low temperatures. These defect states can increase the recombination, and charged impurities scatter the charge carriers, reducing the photoresponse. The dielectric medium screens the Coulomb scatterers [225] as well as delocalizes the localized defect states [2] thereby enhancing the photoresponse. The dielectric medium also tunes the defect levels by screening the bound carrier charged interactions, thereby converting many deep levels into shallow defect levels. [3] Since deep levels mostly contribute to bimolecular recombinations, the enhancement in photoresponse towards low temperatures can be attributed to the reduction in the number of recombination centers in the presence of the dielectric medium. The enhancement is ascribed to the dielectric constant of the medium.[284] We did not observe any significant difference even if the dielectric material is ferroelectric. Any possible contribution due to the ferroelectric property of the medium needs further careful investigation.

6.3.6 Temperature dependence of time-resolved photoresponse

The time-resolved photoresponse of the device (Figure 6.7(a)) was measured at a reverse bias of 3 V when illuminated with a 630 nm LED with 2 mW/cm^2 intensity. At room temperature, the device exhibits a faster rise/decay times of 36 µs /116 µs (Figure 6.7(b)). The relatively fast response time can be attributed to the rapid separation of the photogenerated carriers by the built-in electric field at the Si-MoS_2 junction. Both the rise and fall time increases with temperature. Rise time and decay time (Figure 6.7(c, d)) increase from 19.7 µs to 36 µs and 57 µs to 116 µs, respectively, as the temperature rises from 100 K to 300 K.

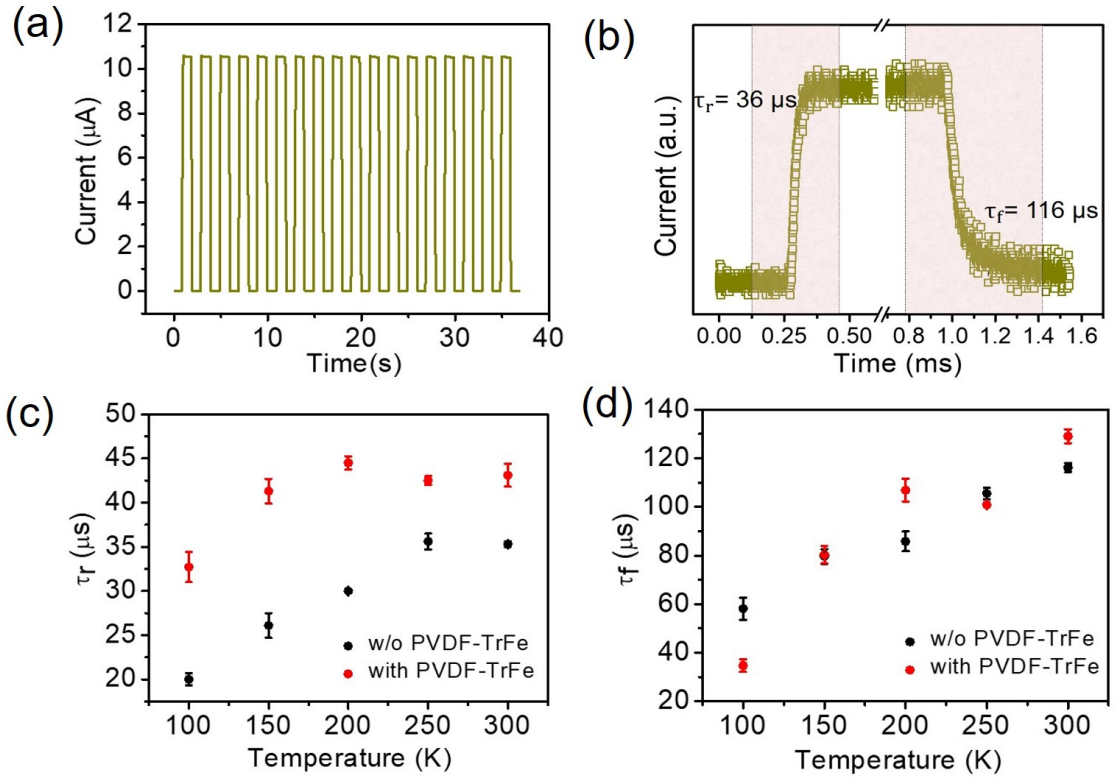

Figure 6.7: (a) Time-resolved photoresponse and (b) rise time and fall time of a pristine silicon-MoS_2 p-n junction when illuminated with a 630 nm LED at a reverse bias of 3 V at 300 K. Comparison of the (c) rise time (τ_r) and (d) fall time (τ_f) with temperature in the presence and absence of PVDF-TrFe. The generation of more shallow levels by the dielectric medium increases the lifetime of the photogenerated carriers.

This increase can be associated with the generation of more shallow levels with temperature. The energy difference between steady-state Fermi levels (explained in the next section) and their respective band edges depends on the absolute temperature.[231] With the increase in temperature, the steady state Fermi levels come closer. The defect levels between the steady state Fermi levels act as recombination centers (deep levels), and those between the steady state and band edges as trap states (shallow levels). Hence with an increase in temperature, the number of deep levels decreases, and shallow levels increases. These shallow defect levels can have a significant influence on the rise and fall time. With an increase in the number of shallow levels,

the trapping of carriers increases. Hence, under illumination, to increase the density of free carriers, the density of carriers in the shallow trapping states should be increased in the same proportion.[231] A steady state photocurrent can be attained only after filling the shallow traps. Thus depending on the ratio of carriers trapped in the shallow levels to free carriers, the rise time increases. Similarly, when the illumination is turned off, the carriers trapped in the shallow levels should get emptied. Decay time tends to increase with the ratio of trapped carriers in the shallow levels to free carriers.[231] In the presence of PVDF-TrFe, the general trend of response times with temperature remains the same as of the pristine device in the absence of a dielectric medium, but the rise time is observed to increase slightly, whereas the decay time remains nearly the same. This could be attributed to the deep to shallow defect level transitions facilitated by the dielectric screening of defect states.[2, 3] The generation of more shallow levels increases the lifetime of the photogenerated carriers making the device slower.[231]

6.3.7 Temperature dependence of intensity-dependent photocurrent

A comprehensive understanding of the distribution of trap states can be obtained from the measurement of photocurrent at low light intensities and various temperatures. The device was biased at a reverse bias of 2 V and illuminated with a 630 nm LED by varying the intensity from 0.1 µW to 100 µW. The photocurrent exhibited a fractional power dependence of the form $I \propto P^{\alpha}$ with light intensity (Figure 6.8(a)). The value of the exponent α was observed to increase with temperature. For the pristine device, α varied from 0.43 to 0.86 as the temperature increased from 50 K to 300 K (Figure 6.8(b)).

This sublinear dependence indicates the presence of trap states in the device.[242]

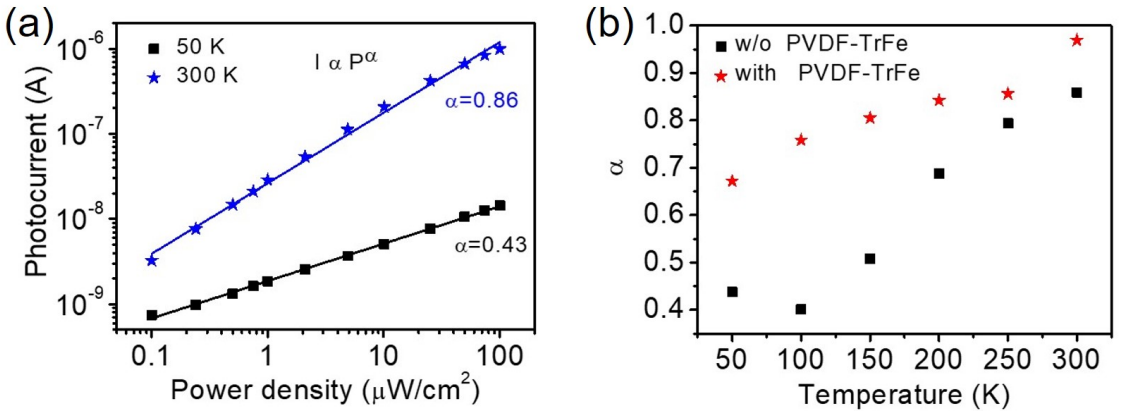

Figure 6.8: (a) Intensity-dependent photocurrent measured at a reverse bias of 2 V and temperatures 50K and 300K. (b) Dependence of the exponent (α) in the power law $I \propto P^{\alpha}$ with temperature.A transition from bimolecular to monomolecular recombination is observed with an increase in temperature.

When the the device is illuminated with light, the intrinsic Fermi level splits into two steady-state quasi-Fermi levels corresponding to the electron and hole concentrations in the conduction and valence bands respectively.[301] The trap states present between the steady state Fermi levels and the corresponding band edges do not contribute to recombination as the carriers trapped in these states quickly get thermally re-excited back into their respective bands.[215] Trap states between the steady states act as recombination centers and any charge carrier trapped in these states does not contribute to conductivity. With the increase in light intensity, steady-state Fermi levels move toward the band edges, generating more recombination centers. This , in turn, reduces the lifetime of the free carriers producing a sub-linear dependence of photocurrent on light intensity.[301] But with the increase in temperature, this process reverses as the steady-state Fermi levels come closer to each other [231, 302] and we observe a transition from bimolecular to monomolecular recombination. In the presence of PVDF-TrFe, the value of α increased compared to that of the pristine device. An increase in α was more significant at low temperatures (less than 250K). This could be attributed to the reduction in the number of recombination centers

as more deep levels get converted to shallow levels in the presence of the dielectric medium. The dielectric medium would screen the interaction between the charge carrier and the defect state producing a transition in the defect states from deep to shallow level. This shift in defect level is proportional to the effective dielectric constant of the environment.[3, 2]

6.3.8 Temperature dependence of low frequency 1/f noise

Temperature-dependent low-frequency noise analysis can give deeper insights into the presence of defects in the system. The normalized noise spectral density S_I/I^2 and noise amplitude can be used together to characterize the $1/f$ noise in a device. $1/f$ noise can be expressed using Hooge empirical law given by [303]

$$\frac{S_I}{I^2} = \frac{A}{I^\alpha} \tag{6.5}$$

where S_I is the current power spectral density, I is the mean device current, f is the frequency, and A is the noise amplitude (given by $A = \alpha_H/N$, α_H is the Hooge parameter and N is the total number of carriers) where the exponents α is ideally expected to be close to 1.[303] The noise spectra were measured at a reverse bias of 2 V and in the temperature range 150 K - 300 K in the presence and absence of PVDF-TrFe (Figure 6.9(a, b)). The device exhibited $1/f$ noise at all temperatures. S_I/I^2 measured at a frequency of 10 Hz (Figure 6.9(c)) was observed to decrease with increase in temperature. The variation was more significant in the absence of PVDF-TrFe, producing a three-order magnitude lower value at 300 K compared to that at 150 K.

Hopping conductivity through the defect states (localized states) can cause $1/f$ noise. Theoretical studies in transistors predict the existence of a broad distribution of the waiting time between successive hops for carriers in variable range hopping

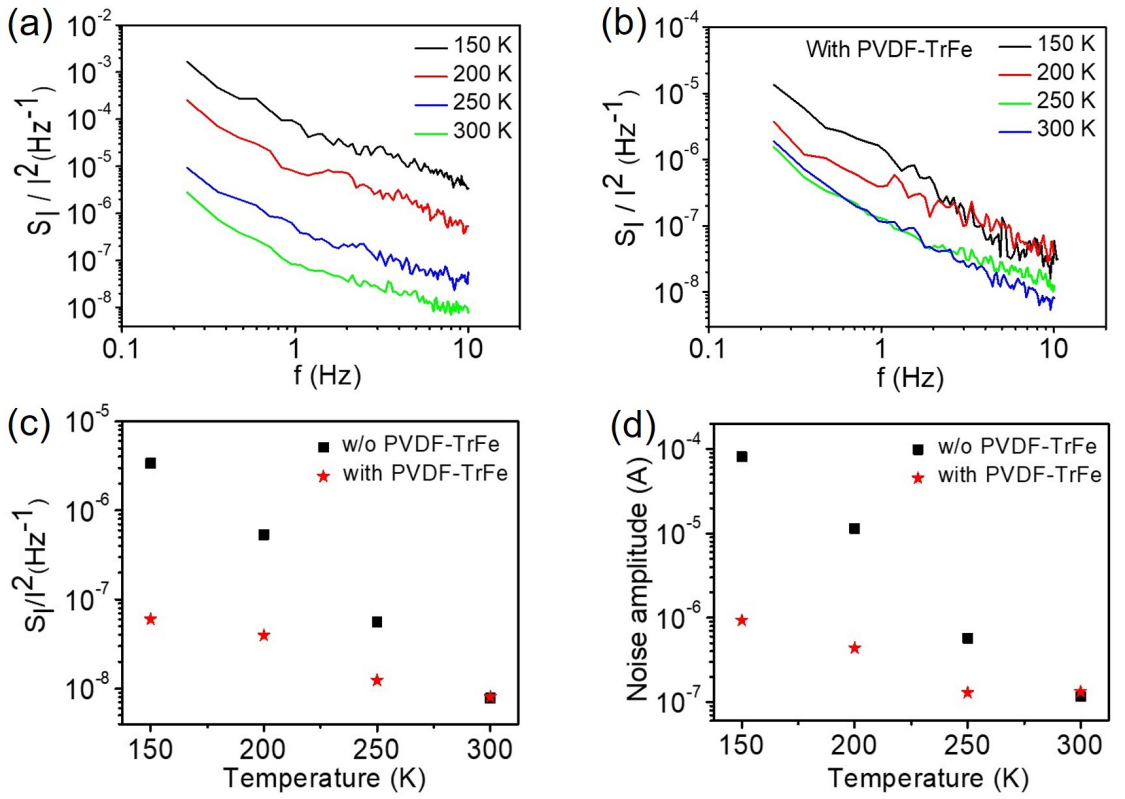

Figure 6.9: Normalized noise spectral density of silicon-MoS_2 p-n junction at 2 V reverse bias under dark conditions in the (a) presence and (b) absence of PVDF-TrFe at different temperatures. Comparison of (c) variation of normalized noise spectral density at 10 Hz frequency and (d) Noise amplitude (A) with temperature in the presence and absence of PVDF-TrFe. Hopping conductivity through the defect states (localized states) causes $1/f$ noise.

(VRH) transport. This causes the noise to increase with decreasing temperature. [304] Two models have been proposed namely the number fluctuation theory and the mobility fluctuation theory to explain such noise behaviors. According to mobility fluctuation theory, hopping noise has a weak temperature dependence whereas the carrier number fluctuation model predicts an increase in the number of carriers taking part in conduction with the increase in temperature due to the decreasing length of a typical jump.[305] In the presence of a dielectric environment (PVDF-TrFe), the strong Coulomb interaction between the charged defect and the charge

carrier gets screened. This, in turn, delocalizes the spatial distributions of the defect charge densities.[2] Thus, the decrease in S_I/I^2 with temperature in the presence of PVDF-TrFe is less rapid, nearly seven times, compared to that without PVDF-TrFe.The noise amplitude (A), which is a measure of the noise level in the device also shows a similar trend. The value of A decreases with increasing temperature (Figure 6.9(d)), which indicates an increase in the carrier density (which is consistent with the increase in the ideality factor in this temperature range). A decreases by more than two orders of magnitude when the temperature increases from 150 K to 300 K in the absence of PVDF-TrFe, while it decreases only by 9 times in the presence of PVDF-TrFe. At room temperature, the device exhibits a specific detectivity (D) [306] of around 1×10^{10} Jones, comparable to the previously reported values for silicon- MoS_2 heterostructure.[103]

6.4 Summary

In summary, we studied the temperature-dependent electronic transport properties of silicon- MoS_2 p-n junction heterostructure. The temperature-dependent I-V characteristics suggest the presence of a space charge limited transport. At low temperatures, transport predominantly takes place via hopping through defect states. The carrier number fluctuation model could explain the temperature dependence of low-frequency noise. From the intensity-dependent photoresponse, a transition from bimolecular to monomolecular recombination is observed with increasing temperature. The rise and the decay times of the photocurrent were also observed to increase with temperature. Our results show that the photoresponse in the p-n junction is mainly dominated by the presence of defect states. These states can act either as a trap state or recombination center depending on their position in energy. They can also act as scattering centers for the charge carriers. The deep-level traps act as effective

electron-hole recombination centers and reduce the photoconversion efficiency of the device by causing non-radiative recombinations. The role of defect states in limiting the photoresponse was observed to dominate more towards lower temperatures. The defects can be screened by varying the surrounding dielectric environment. We observed a significant enhancement in photoresponse and lower noise levels in the presence of a surrounding dielectric medium. The lower the noise levels, the better the sensitivity of the device. The decrease in the density of recombination centers would also increase the carrier lifetime of the charge carriers. The screening of defects and impurities would also reduce the charge carrier scattering which in turn improves the mobility of the device. Insights from this study can be extended to enhance the optoelectronic properties of devices based on various low-dimensional materials exploiting their sensitivity to the surrounding environment.

Chapter 7

Conclusions and Future Directions

7.1 Conclusions

This dissertation demonstrates the potential of dielectric engineering of the surrounding environment of 2D TMDs in modulating their optoelectronic properties. First, in chapter 3, using MoS_2 as a model system, the important role of various growth parameters and requisite of a growth promoter in the Chemical Vapor deposition synthesis of TMDs was investigated. The parameters were optimized and centimeter scale large area coverage of monolayer MoS_2 was achieved. CVD synthesis was observed to be very sensitive to each growth parameter. Further, engineering the surrounding dielectric environment of MoS_2 proved to be an efficient way of improving its charge transport and optoelectronic properties. Implementing this in chapter 4, a two-order enhancement in mobility and variation in photoresponse relaxation times were obtained in monolayer MoS_2 FET. This approach was also efficient in producing a three-order enhancement in photocurrent when extended to a mixed dimensional van der Waals heterostructure formed between silicon and MoS_2, as shown in chapter 5. Defects present in TMDs can often contribute to non-radiative recombinations and reduce the quantum efficiency of such heterostructures. Chapter 6 identifies deep-level defects as major recombination centers in limiting the photoresponse. These defects can be screened and converted to shallow levels by modulating their local dielectric environment, resulting in photoresponse enhancement.

7.2 Future directions

Below are some of the future directions of the thesis's outcome.

- In chapters 5 and 6, we have used PVDF-TrFe, a ferroelectric polymer, as the dielectric medium. We plan to understand whether its ferroelectric property plays any role in enhancing the photoresponse of the heterostructure. If so, how would electric poling the ferroelectric domains influence the device's optoelectronic properties?

- The concept of dielectric engineering can be utilized to modulate the electroluminescence emission peaks in light-emitting devices. Different dielectric environments experienced by the 2D materials modify the exciton binding energy and produce different emission peaks.

- The dielectric environment-dependent bandgap tuning of TMDs can be leveraged in tunneling field-effect transistors (TFET) based on van der Waals heterostructures. The large bandgap in monolayer TMDs reduces the band-to-band tunneling probability due to the larger tunnel barrier height. The tunnel barrier can be reduced by tuning the bandgap of the desired TMD by selecting a suitable dielectric medium.

- The dielectric environment of 2D materials can be selectively controlled to form homojunctions. The bandgap and the potential barrier at the junction can be further modulated by applying additional gate voltages. This would broaden and give better control over the wavelength range of photodetection and the magnitude of photoresponsivity.

Bibliography

[1] Driss Mouloua, Ahmed Kotbi, Geetanjali Deokar, Khaled Kaja, Mimoun El Marssi, My Ali El Khakani, and Mustapha Jouiad. Recent progress in the synthesis of mos2 thin films for sensing, photovoltaic and plasmonic applications: a review. *Materials*, 14(12):3283, 2021.

[2] Ji-Young Noh, Hanchul Kim, Minkyu Park, and Yong-Sung Kim. Deep-to-shallow level transition of re and nb dopants in monolayer mos 2 with dielectric environments. *Physical Review B*, 92(11):115431, 2015.

[3] Akash Singh, Aaditya Manjanath, and Abhishek K Singh. Engineering defect transition-levels through the van der waals heterostructure. *The Journal of Physical Chemistry C*, 122(42):24475–24480, 2018.

[4] Nan Ma and Debdeep Jena. Charge scattering and mobility in atomically thin semiconductors. *Physical Review X*, 4(1):011043, 2014.

[5] Luzhao Sun, Guowen Yuan, Libo Gao, Jieun Yang, Manish Chhowalla, Meysam Heydari Gharahcheshmeh, Karen K Gleason, Yong Seok Choi, Byung Hee Hong, and Zhongfan Liu. Chemical vapour deposition. *Nature Reviews Methods Primers*, 1(1):1–20, 2021.

[6] Andrea Splendiani, Liang Sun, Yuanbo Zhang, Tianshu Li, Jonghwan Kim, Chi-Yung Chim, Giulia Galli, and Feng Wang. Emerging photoluminescence in monolayer mos2. *Nano letters*, 10(4):1271–1275, 2010.

[7] Arnoud P Van Der Wel, Eric AM Klumperink, Jay S Kolhatkar, Eric Hoekstra, Martijn F Snoeij, Cora Salm, Hans Wallinga, and Bram Nauta. Low-frequency noise phenomena in switched mosfets. *IEEE journal of solid-state circuits*, 42(3):540–550, 2007.

[8] what-when how.com. Nanolithography: Length-scale limitations part 1 (nanotechnology). http://what-when-how.com/nanoscience-and-nanotechnology/nanolithography-length-scale-limitations-part-1-nanotechnology/.

[9] Hamid M Ghaithan, Saif MH Qaid, Zeyad A Alahmed, Mahmoud Hezam, Andreas Lyras, Mabrook Amer, and Abdullah S Aldwayyan. Anion substitution effects on the structural, electronic, and optical properties of inorganic cspb (i1–x br x) 3 and cspb (br1–x cl x) 3 perovskites: Theoretical and experimental approaches. *The Journal of Physical Chemistry C*, 125(1):886–897, 2021.

[10] Michael Huff. Microsystems manufacturing methods: Mems processes. In *Process Variations in Microsystems Manufacturing*, pages 99–171. Springer, 2020.

[11] Nicolas Mounet, Marco Gibertini, Philippe Schwaller, Davide Campi, Andrius Merkys, Antimo Marrazzo, Thibault Sohier, Ivano Eligio Castelli, Andrea Cepellotti, Giovanni Pizzi, et al. Two-dimensional materials from high-throughput computational exfoliation of experimentally known compounds. *Nature nanotechnology*, 13(3):246–252, 2018.

[12] Wei Cao, Junkai Jiang, Xuejun Xie, Arnab Pal, Jae Hwan Chu, Jiahao Kang, and Kaustav Banerjee. 2-d layered materials for next-generation electronics: Opportunities and challenges. *IEEE Transactions on Electron Devices*, 65(10):4109–4121, 2018.

[13] Kostya S Novoselov, D Jiang, F Schedin, TJ Booth, VV Khotkevich, SV Morozov, and Andre K Geim. Two-dimensional atomic crystals. *Proceedings of the National Academy of Sciences*, 102(30):10451–10453, 2005.

[14] Andre K Geim and Konstantin S Novoselov. The rise of graphene. *Nature materials*, 6(3):183–191, 2007.

[15] Kirill I Bolotin, K J Sikes, Zhifang Jiang, M Klima, G Fudenberg, James Hone, Phaly Kim, and Horst L Stormer. Ultrahigh electron mobility in suspended graphene. *Solid state communications*, 146(9-10):351–355, 2008.

[16] Xiao Li and Hongwei Zhu. Two-dimensional mos2: Properties, preparation, and applications. *Journal of Materiomics*, 1(1):33–44, 2015.

[17] Saptarshi Das, Joshua A Robinson, Madan Dubey, Humberto Terrones, and Mauricio Terrones. Beyond graphene: progress in novel two-dimensional materials and van der waals solids. *Annual Review of Materials Research*, pages 1–27, 2015.

[18] Kin Fai Mak, Changgu Lee, James Hone, Jie Shan, and Tony F Heinz. Atomically thin mos 2: a new direct-gap semiconductor. *Physical review letters*, 105(13):136805, 2010.

[19] Bei Zhao, Dingyi Shen, Zucheng Zhang, Ping Lu, Mongur Hossain, Jia Li, Bo Li, and Xidong Duan. 2d metallic transition-metal dichalcogenides: Structures, synthesis, properties, and applications. *Advanced Functional Materials*, 31(48):2105132, 2021.

[20] RF Frindt. Single crystals of mos2 several molecular layers thick. *Journal of Applied Physics*, 37(4):1928–1929, 1966.

[21] Per Joensen, RF Frindt, and S Roy Morrison. Single-layer mos2. *Materials research bulletin*, 21(4):457–461, 1986.

[22] D Avellaneda, I Sánchez-Orozco, JAA Martínez, S Shaji, and B Krishnan. Thin films of tin sulfides: Structure, composition and optoelectronic properties. *Materials Research Express*, 6(1):016409, 2018.

[23] Biswajit Barman, Kasturi V Bangera, and GK Shivakumar. Evaluation of semiconducting p-type tin sulfide thin films for photodetector applications. *Superlattices and Microstructures*, 133:106215, 2019.

[24] Mohammad Jafar Molaei, Mohammad Younas, and Mashallah Rezakazemi. A comprehensive review on recent advances in two-dimensional (2d) hexagonal boron nitride. *ACS Applied Electronic Materials*, 3(12):5165–5187, 2021.

[25] Joshua D Caldwell, Igor Aharonovich, Guillaume Cassabois, James H Edgar, Bernard Gil, and DN Basov. Photonics with hexagonal boron nitride. *Nature Reviews Materials*, 4(8):552–567, 2019.

[26] Vinod K Sangwan and Mark C Hersam. Electronic transport in two-dimensional materials. *arXiv preprint arXiv:1802.01045*, 2018.

[27] Yijun Xu, Zhe Shi, Xinyao Shi, Kai Zhang, and Han Zhang. Recent progress in black phosphorus and black-phosphorus-analogue materials: properties, synthesis and applications. *Nanoscale*, 11(31):14491–14527, 2019.

[28] Wonbong Choi, Nitin Choudhary, Gang Hee Han, Juhong Park, Deji Akinwande, and Young Hee Lee. Recent development of two-dimensional transition metal dichalcogenides and their applications. *Materials Today*, 20(3):116–130, 2017.

[29] Qing Hua Wang, Kourosh Kalantar-Zadeh, Andras Kis, Jonathan N Coleman, and Michael S Strano. Electronics and optoelectronics of two-dimensional transition metal dichalcogenides. *Nature nanotechnology*, 7(11):699–712, 2012.

[30] Unni Krishnan, Manjot Kaur, Kulwinder Singh, Manjeet Kumar, and Akshay Kumar. A synoptic review of mos2: Synthesis to applications. *Superlattices and Microstructures*, 128:274–297, 2019.

[31] Simone Bertolazzi, Jacopo Brivio, and Andras Kis. Stretching and breaking of ultrathin mos2. *ACS nano*, 5(12):9703–9709, 2011.

[32] Diana Y Qiu, H Felipe, and Steven G Louie. Optical spectrum of mos 2: many-body effects and diversity of exciton states. *Physical review letters*, 111(21):216805, 2013.

[33] Miguel M Ugeda, Aaron J Bradley, Su-Fei Shi, Felipe H Da Jornada, Yi Zhang, Diana Y Qiu, Wei Ruan, Sung-Kwan Mo, Zahid Hussain, Zhi-Xun Shen, et al. Giant bandgap renormalization and excitonic effects in a monolayer transition metal dichalcogenide semiconductor. *Nature materials*, 13(12):1091–1095, 2014.

[34] Ashwin Ramasubramaniam. Large excitonic effects in monolayers of molybdenum and tungsten dichalcogenides. *Physical Review B*, 86(11):115409, 2012.

[35] Junga Ryou, Yong-Sung Kim, Santosh Kc, and Kyeongjae Cho. Monolayer mos2 bandgap modulation by dielectric environments and tunable bandgap transistors. *Scientific reports*, 6(1):1–8, 2016.

[36] Yuxuan Lin, Xi Ling, Lili Yu, Shengxi Huang, Allen L Hsu, Yi-Hsien Lee, Jing Kong, Mildred S Dresselhaus, and Tomás Palacios. Dielectric screening of excitons and trions in single-layer mos2. *Nano letters*, 14(10):5569–5576, 2014.

[37] Archana Raja, Andrey Chaves, Jaeeun Yu, Ghidewon Arefe, Heather M Hill, Albert F Rigosi, Timothy C Berkelbach, Philipp Nagler, Christian Schüller, Tobias Korn, et al. Coulomb engineering of the bandgap and excitons in two-dimensional materials. *Nature communications*, 8(1):1–7, 2017.

[38] Branimir Radisavljevic and Andras Kis. Mobility engineering and a metal–insulator transition in monolayer mos2. *Nature materials*, 12(9):815–820, 2013.

[39] LV Keldysh. Coulomb interaction in thin semiconductor and semimetal films. *Soviet Journal of Experimental and Theoretical Physics Letters*, 29:658, 1979.

[40] Timothy C Berkelbach, Mark S Hybertsen, and David R Reichman. Theory of neutral and charged excitons in monolayer transition metal dichalcogenides. *Physical Review B*, 88(4):045318, 2013.

[41] Gang Wang, Alexey Chernikov, Mikhail M Glazov, Tony F Heinz, Xavier Marie, Thierry Amand, and Bernhard Urbaszek. Colloquium: Excitons in atomically thin transition metal dichalcogenides. *Reviews of Modern Physics*, 90(2):021001, 2018.

[42] Yeongsu Cho and Timothy C Berkelbach. Environmentally sensitive theory of electronic and optical transitions in atomically thin semiconductors. *Physical Review B*, 97(4):041409, 2018.

[43] M Utama, Hans Kleemann, Wenyu Zhao, Chin Shen Ong, Felipe H da Jornada, Diana Y Qiu, Hui Cai, Han Li, Rai Kou, Sihan Zhao, et al. A dielectric-defined lateral heterojunction in a monolayer semiconductor. *Nature Electronics*, 2(2):60–65, 2019.

[44] Qiang Xu, Yingri Sun, Peng Yang, and Yaping Dan. Density of defect states retrieved from the hysteretic gate transfer characteristics of monolayer mos2 field effect transistors. *AIP Advances*, 9(1):015230, 2019.

[45] Raquel Esteban-Puyuelo and Biplab Sanyal. Role of defects in ultrafast charge recombination in monolayer mos 2. *Physical Review B*, 103(23):235433, 2021.

[46] Bing Huang, Mina Yoon, Bobby G Sumpter, Su-Huai Wei, and Feng Liu. Alloy engineering of defect properties in semiconductors: suppression of deep levels in transition-metal dichalcogenides. *Physical Review Letters*, 115(12):126806, 2015.

[47] Ji-Young Noh, Hanchul Kim, and Yong-Sung Kim. Stability and electronic structures of native defects in single-layer mos 2. *Physical Review B*, 89(20):205417, 2014.

[48] Linqiu Li, Run Long, and Oleg V Prezhdo. Why chemical vapor deposition grown mos2 samples outperform physical vapor deposition samples: time-domain ab initio analysis. *Nano Letters*, 18(6):4008–4014, 2018.

[49] Dan Wang and Ravishankar Sundararaman. Layer dependence of defect charge transition levels in two-dimensional materials. *Physical Review B*, 101(5):054103, 2020.

[50] Dan Wang and Ravishankar Sundararaman. Substrate effects on charged defects in two-dimensional materials. *Physical Review Materials*, 3(8):083803, 2019.

[51] Zhihao Yu, Zhun-Yong Ong, Songlin Li, Jian-Bin Xu, Gang Zhang, Yong-Wei Zhang, Yi Shi, and Xinran Wang. Analyzing the carrier mobility in transition-metal dichalcogenide mos2 field-effect transistors. *Advanced Functional Materials*, 27(19):1604093, 2017.

[52] Kristen Kaasbjerg, Kristian S Thygesen, and Karsten W Jacobsen. Phonon-limited mobility in n-type single-layer mos 2 from first principles. *Physical Review B*, 85(11):115317, 2012.

[53] Zhihao Yu, Yiming Pan, Yuting Shen, Zilu Wang, Zhun-Yong Ong, Tao Xu, Run Xin, Lijia Pan, Baigeng Wang, Litao Sun, et al. Towards intrinsic charge transport in monolayer molybdenum disulfide by defect and interface engineering. *Nature communications*, 5(1):1–7, 2014.

[54] Zhihao Yu, Zhun-Yong Ong, Yiming Pan, Yang Cui, Run Xin, Yi Shi, Baigeng Wang, Yun Wu, Tangsheng Chen, Yong-Wei Zhang, et al. Realization of room-

temperature phonon-limited carrier transport in monolayer mos2 by dielectric and carrier screening. *Advanced Materials*, 28(3):547–552, 2016.

[55] Subhamoy Ghatak, Atindra Nath Pal, and Arindam Ghosh. Nature of electronic states in atomically thin mos2 field-effect transistors. *ACS nano*, 5(10):7707–7712, 2011.

[56] Debdeep Jena and Aniruddha Konar. Enhancement of carrier mobility in semiconductor nanostructures by dielectric engineering. *Physical review letters*, 98(13):136805, 2007.

[57] Branimir Radisavljevic, Aleksandra Radenovic, Jacopo Brivio, Valentina Giacometti, and Andras Kis. Single-layer mos2 transistors. *Nature nanotechnology*, 6(3):147–150, 2011.

[58] Dominik Lembke and Andras Kis. Breakdown of high-performance monolayer mos2 transistors. *ACS nano*, 6(11):10070–10075, 2012.

[59] Branimir Radisavljevic, Michael Brian Whitwick, and Andras Kis. Integrated circuits and logic operations based on single-layer mos2. *ACS nano*, 5(12):9934–9938, 2011.

[60] Daria Krasnozhon, Dominik Lembke, Clemens Nyffeler, Yusuf Leblebici, and Andras Kis. Mos2 transistors operating at gigahertz frequencies. *Nano letters*, 14(10):5905–5911, 2014.

[61] Branimir Radisavljevic, Michael B Whitwick, and Andras Kis. Small-signal amplifier based on single-layer mos2. *Applied Physics Letters*, 101(4):043103, 2012.

[62] Simone Bertolazzi, Daria Krasnozhon, and Andras Kis. Nonvolatile memory cells based on mos2/graphene heterostructures. *ACS nano*, 7(4):3246–3252, 2013.

[63] Oriol Lopez-Sanchez, Dominik Lembke, Metin Kayci, Aleksandra Radenovic, and Andras Kis. Ultrasensitive photodetectors based on monolayer mos2. *Nature nanotechnology*, 8(7):497–501, 2013.

[64] RS Sundaram, M Engel, A Lombardo, R Krupke, AC Ferrari, Ph Avouris, and M Steiner. Electroluminescence in single layer mos2. *Nano letters*, 13(4):1416–1421, 2013.

[65] Oriol Lopez-Sanchez, Esther Alarcon Llado, Volodymyr Koman, Anna Fontcuberta i Morral, Aleksandra Radenovic, and Andras Kis. Light generation and harvesting in a van der waals heterostructure. *Acs Nano*, 8(3):3042–3048, 2014.

[66] Meng-Lin Tsai, Sheng-Han Su, Jan-Kai Chang, Dung-Sheng Tsai, Chang-Hsiao Chen, Chih-I Wu, Lain-Jong Li, Lih-Juann Chen, and Jr-Hau He. Monolayer mos2 heterojunction solar cells. *ACS nano*, 8(8):8317–8322, 2014.

[67] Yuka Tsuboi, Feijiu Wang, Daichi Kozawa, Kazuma Funahashi, Shinichiro Mouri, Yuhei Miyauchi, Taishi Takenobu, and Kazunari Matsuda. Enhanced photovoltaic performances of graphene/si solar cells by insertion of a mos 2 thin film. *Nanoscale*, 7(34):14476–14482, 2015.

[68] Eric Singh, Ki Seok Kim, Geun Young Yeom, and Hari Singh Nalwa. Atomically thin-layered molybdenum disulfide (mos2) for bulk-heterojunction solar cells. *ACS applied materials & interfaces*, 9(4):3223–3245, 2017.

[69] Xiaotian Hu, Lie Chen, Licheng Tan, Yong Zhang, Lin Hu, Bing Xie, and Yiwang Chen. Versatile mos2 nanosheets in ito-free and semi-transparent polymer power-generating glass. *Scientific reports*, 5(1):1–13, 2015.

[70] Yu Geun Kim, Ki Chang Kwon, Quyet Van Le, Kootak Hong, Ho Won Jang, and Soo Young Kim. Atomically thin two-dimensional materials as hole ex-

traction layers in organolead halide perovskite photovoltaic cells. *Journal of Power Sources*, 319:1–8, 2016.

[71] PM Solomon, BA Bryce, MA Kuroda, R Keech, S Shetty, TM Shaw, M Copel, L-W Hung, AG Schrott, C Armstrong, et al. Pathway to the piezoelectronic transduction logic device. *Nano letters*, 15(4):2391–2395, 2015.

[72] Dennis Newns, Bruce Elmegreen, Xiao Hu Liu, and Glenn Martyna. A low-voltage high-speed electronic switch based on piezoelectric transduction. *Journal of Applied Physics*, 111(8):084509, 2012.

[73] Eric Singh, Pragya Singh, Ki Seok Kim, Geun Young Yeom, and Hari Singh Nalwa. Flexible molybdenum disulfide (mos2) atomic layers for wearable electronics and optoelectronics. *ACS applied materials & interfaces*, 11(12):11061–11105, 2019.

[74] Ananthakumar Ramadoss, Taehyun Kim, Gui-Shik Kim, and Sang Jae Kim. Enhanced activity of a hydrothermally synthesized mesoporous mos 2 nanostructure for high performance supercapacitor applications. *New Journal of Chemistry*, 38(6):2379–2385, 2014.

[75] Rusen Yan, Jeffrey R Simpson, Simone Bertolazzi, Jacopo Brivio, Michael Watson, Xufei Wu, Andras Kis, Tengfei Luo, Angela R Hight Walker, and Huili Grace Xing. Thermal conductivity of monolayer molybdenum disulfide obtained from temperature-dependent raman spectroscopy. *ACS nano*, 8(1):986–993, 2014.

[76] Michele Buscema, Maria Barkelid, Val Zwiller, Herre SJ van der Zant, Gary A Steele, and Andres Castellanos-Gomez. Large and tunable photothermoelectric effect in single-layer mos2. *Nano letters*, 13(2):358–363, 2013.

[77] Wen Huang, Xin Luo, Chee Kwan Gan, Su Ying Quek, and Gengchiau Liang. Theoretical study of thermoelectric properties of few-layer mos 2 and wse 2. *Physical Chemistry Chemical Physics*, 16(22):10866–10874, 2014.

[78] Deblina Sarkar, Wei Liu, Xuejun Xie, Aaron C Anselmo, Samir Mitragotri, and Kaustav Banerjee. Mos2 field-effect transistor for next-generation label-free biosensors. *ACS nano*, 8(4):3992–4003, 2014.

[79] Lu Wang, Ye Wang, Jen It Wong, Tomás Palacios, Jing Kong, and Hui Ying Yang. Functionalized mos2 nanosheet-based field-effect biosensor for label-free sensitive detection of cancer marker proteins in solution. *Small*, 10(6):1101–1105, 2014.

[80] Bilu Liu, Liang Chen, Gang Liu, Ahmad N Abbas, Mohammad Fathi, and Chongwu Zhou. High-performance chemical sensing using schottky-contacted chemical vapor deposition grown monolayer mos2 transistors. *ACS nano*, 8(5):5304–5314, 2014.

[81] Adam L Friedman, F Keith Perkins, Enrique Cobas, Glenn G Jernigan, Paul M Campbell, Aubrey T Hanbicki, and Berend T Jonker. Chemical vapor sensing of two-dimensional mos2 field effect transistor devices. *Solid-state electronics*, 101:2–7, 2014.

[82] Yongji Gong, Junhao Lin, Xingli Wang, Gang Shi, Sidong Lei, Zhong Lin, Xiaolong Zou, Gonglan Ye, Robert Vajtai, Boris I Yakobson, et al. Vertical and in-plane heterostructures from ws2/mos2 monolayers. *Nature materials*, 13(12):1135–1142, 2014.

[83] KS Novoselov, o A Mishchenko, o A Carvalho, and AH Castro Neto. 2d materials and van der waals heterostructures. *Science*, 353(6298):aac9439, 2016.

[84] Deep Jariwala, Tobin J Marks, and Mark C Hersam. Mixed-dimensional van der waals heterostructures. *Nature materials*, 16(2):170–181, 2017.

[85] Frank Schwierz. Graphene transistors. *Nature nanotechnology*, 5(7):487–496, 2010.

[86] Zongyou Yin, Hai Li, Hong Li, Lin Jiang, Yumeng Shi, Yinghui Sun, Gang Lu, Qing Zhang, Xiaodong Chen, and Hua Zhang. Single-layer mos2 phototransistors. *ACS nano*, 6(1):74–80, 2012.

[87] Wenzhong Bao, Xinghan Cai, Dohun Kim, Karthik Sridhara, and Michael S Fuhrer. High mobility ambipolar mos2 field-effect transistors: Substrate and dielectric effects. *Applied Physics Letters*, 102(4):042104, 2013.

[88] Gwan-Hyoung Lee, Young-Jun Yu, Xu Cui, Nicholas Petrone, Chul-Ho Lee, Min Sup Choi, Dae-Yeong Lee, Changgu Lee, Won Jong Yoo, Kenji Watanabe, et al. Flexible and transparent mos2 field-effect transistors on hexagonal boron nitride-graphene heterostructures. *ACS nano*, 7(9):7931–7936, 2013.

[89] Saptarshi Das, Hong-Yan Chen, Ashish Verma Penumatcha, and Joerg Appenzeller. High performance multilayer mos2 transistors with scandium contacts. *Nano letters*, 13(1):100–105, 2013.

[90] Aravindh Kumar, Kirstin Schauble, Kathryn M Neilson, Alvin Tang, Pranav Ramesh, H-S Philip Wong, Eric Pop, and Krishna Saraswat. Sub-200 $\omega\cdot$ μm alloyed contacts to synthetic monolayer mos2. In *2021 IEEE International Electron Devices Meeting (IEDM)*, pages 7–3. IEEE, 2021.

[91] Pin-Chun Shen, Cong Su, Yuxuan Lin, Ang-Sheng Chou, Chao-Ching Cheng, Ji-Hoon Park, Ming-Hui Chiu, Ang-Yu Lu, Hao-Ling Tang, Mohammad Mahdi Tavakoli, et al. Ultralow contact resistance between semimetal and monolayer semiconductors. *Nature*, 593(7858):211–217, 2021.

[92] Zheng Yang, Changsik Kim, Kwang Young Lee, Myeongjin Lee, Samudrala Appalakondaiah, Chang-Ho Ra, Kenji Watanabe, Takashi Taniguchi, Kyeongjae Cho, Euyheon Hwang, et al. A fermi-level-pinning-free 1d electrical contact at the intrinsic 2d mos2–metal junction. *Advanced Materials*, 31(25):1808231, 2019.

[93] Rajesh Kappera, Damien Voiry, Sibel Ebru Yalcin, Brittany Branch, Gautam Gupta, Aditya D Mohite, and Manish Chhowalla. Phase-engineered low-resistance contacts for ultrathin mos2 transistors. *Nature materials*, 13(12):1128–1134, 2014.

[94] Jingli Wang, Qian Yao, Chun-Wei Huang, Xuming Zou, Lei Liao, Shanshan Chen, Zhiyong Fan, Kai Zhang, Wei Wu, Xiangheng Xiao, et al. High mobility mos2 transistor with low schottky barrier contact by using atomic thick h-bn as a tunneling layer. *Advanced materials*, 28(37):8302–8308, 2016.

[95] Seunghyun Lee, Alvin Tang, Shaul Aloni, and H-S Philip Wong. Statistical study on the schottky barrier reduction of tunneling contacts to cvd synthesized mos2. *Nano letters*, 16(1):276–281, 2016.

[96] Amritanand Sebastian, Rahul Pendurthi, Tanushree H Choudhury, Joan M Redwing, and Saptarshi Das. Benchmarking monolayer mos2 and ws2 field-effect transistors. *Nature communications*, 12(1):1–12, 2021.

[97] Chul-Ho Lee, Gwan-Hyoung Lee, Arend M Van Der Zande, Wenchao Chen, Yilei Li, Minyong Han, Xu Cui, Ghidewon Arefe, Colin Nuckolls, Tony F Heinz, et al. Atomically thin p–n junctions with van der waals heterointerfaces. *Nature nanotechnology*, 9(9):676–681, 2014.

[98] Riccardo Frisenda, Aday J Molina-Mendoza, Thomas Mueller, Andres Castellanos-Gomez, and Herre SJ Van Der Zant. Atomically thin p–n junctions

based on two-dimensional materials. *Chemical Society Reviews*, 47(9):3339–3358, 2018.

[99] Atteq ur Rehman, Muhammad Farooq Khan, Muhammad Arslan Shehzad, Sajjad Hussain, Muhammad Fahad Bhopal, Sang Hee Lee, Jonghwa Eom, Yongho Seo, Jongwan Jung, and Soo Hong Lee. n-mos2/p-si solar cells with al2o3 passivation for enhanced photogeneration. *ACS Applied Materials & Interfaces*, 8(43):29383–29390, 2016.

[100] Chaoyue Liu, Jingshu Guo, Laiwen Yu, Jiang Li, Ming Zhang, Huan Li, Yaocheng Shi, and Daoxin Dai. Silicon/2d-material photodetectors: from near-infrared to mid-infrared. *Light: Science & Applications*, 10(1):1–21, 2021.

[101] Jie You, Yukun Luo, Jie Yang, Jianghua Zhang, Ke Yin, Ke Wei, Xin Zheng, and Tian Jiang. Hybrid/integrated silicon photonics based on 2d materials in optical communication nanosystems. *Laser & Photonics Reviews*, 14(12):2000239, 2020.

[102] Yipeng Zhao and Gang Ouyang. Thickness-dependent photoelectric properties of mos2/si heterostructure solar cells. *Scientific Reports*, 9(1):1–11, 2019.

[103] Gwang Hyuk Shin, Junghoon Park, Khang June Lee, Geon-Beom Lee, Hyun Bae Jeon, Yang-Kyu Choi, Kyoungsik Yu, and Sung-Yool Choi. Si–mos2 vertical heterojunction for a photodetector with high responsivity and low noise equivalent power. *ACS applied materials & interfaces*, 11(7):7626–7634, 2019.

[104] Sajedeh Manzeli, Dmitry Ovchinnikov, Diego Pasquier, Oleg V Yazyev, and Andras Kis. 2d transition metal dichalcogenides. *Nature Reviews Materials*, 2(8):1–15, 2017.

[105] Yumeng Shi, Henan Li, and Lain-Jong Li. Recent advances in controlled synthesis of two-dimensional transition metal dichalcogenides via vapour deposition techniques. *Chemical Society Reviews*, 44(9):2744–2756, 2015.

[106] Zhengyang Cai, Bilu Liu, Xiaolong Zou, and Hui-Ming Cheng. Chemical vapor deposition growth and applications of two-dimensional materials and their heterostructures. *Chemical reviews*, 118(13):6091–6133, 2018.

[107] JR Creighton and P Ho. Introduction to chemical vapor deposition (cvd). *Chemical vapor deposition*, 2:1–22, 2001.

[108] Henan Li, Ying Li, Areej Aljarb, Yumeng Shi, and Lain-Jong Li. Epitaxial growth of two-dimensional layered transition-metal dichalcogenides: growth mechanism, controllability, and scalability. *Chemical reviews*, 118(13):6134–6150, 2017.

[109] Sayan Bhowmik and Ananth Govind Rajan. Chemical vapor deposition of 2d materials: A review of modeling, simulation, and machine learning studies. *Iscience*, page 103832, 2022.

[110] William M Haynes, David R Lide, and Thomas J Bruno. *CRC handbook of chemistry and physics*. CRC press, 2016.

[111] Kibum Kang, Saien Xie, Lujie Huang, Yimo Han, Pinshane Y Huang, Kin Fai Mak, Cheol-Joo Kim, David Muller, and Jiwoong Park. High-mobility three-atom-thick semiconducting films with wafer-scale homogeneity. *Nature*, 520(7549):656–660, 2015.

[112] Qingqing Ji, Yanfeng Zhang, Teng Gao, Yu Zhang, Donglin Ma, Mengxi Liu, Yubin Chen, Xiaofen Qiao, Ping-Heng Tan, Min Kan, et al. Epitaxial monolayer mos2 on mica with novel photoluminescence. *Nano letters*, 13(8):3870–3877, 2013.

[113] Yu Zhang, Yanfeng Zhang, Qingqing Ji, Jing Ju, Hongtao Yuan, Jianping Shi, Teng Gao, Donglin Ma, Mengxi Liu, Yubin Chen, et al. Controlled growth of high-quality monolayer ws2 layers on sapphire and imaging its grain boundary. *ACS nano*, 7(10):8963–8971, 2013.

[114] Peiyu Chen, Wenshuo Xu, Yakun Gao, Jamie H Warner, and Martin R Castell. Epitaxial growth of monolayer mos2 on srtio3 single crystal substrates for applications in nanoelectronics. *ACS Applied Nano Materials*, 1(12):6976–6988, 2018.

[115] Yongji Gong, Bo Li, Gonglan Ye, Shize Yang, Xiaolong Zou, Sidong Lei, Zehua Jin, Elisabeth Bianco, Soumya Vinod, Boris I Yakobson, et al. Direct growth of mos2 single crystals on polyimide substrates. *2D Materials*, 4(2):021028, 2017.

[116] Liang Chen, Bilu Liu, Mingyuan Ge, Yuqiang Ma, Ahmad N Abbas, and Chongwu Zhou. Step-edge-guided nucleation and growth of aligned wse2 on sapphire via a layer-over-layer growth mode. *Acs Nano*, 9(8):8368–8375, 2015.

[117] Jianping Shi, Xiaona Zhang, Donglin Ma, Jianbao Zhu, Yu Zhang, Zhenxi Guo, Yu Yao, Qingqing Ji, Xiuju Song, Yanshuo Zhang, et al. Substrate facet effect on the growth of monolayer mos2 on au foils. *ACS nano*, 9(4):4017–4025, 2015.

[118] Shanshan Wang, Merce Pacios, Harish Bhaskaran, and Jamie H Warner. Substrate control for large area continuous films of monolayer mos2 by atmospheric pressure chemical vapor deposition. *Nanotechnology*, 27(8):085604, 2016.

[119] Yi-Hsien Lee, Lili Yu, Han Wang, Wenjing Fang, Xi Ling, Yumeng Shi, Cheng-Te Lin, Jing-Kai Huang, Mu-Tung Chang, Chia-Seng Chang, et al. Synthesis and transfer of single-layer transition metal disulfides on diverse surfaces. *Nano letters*, 13(4):1852–1857, 2013.

[120] Shisheng Li, Shunfeng Wang, Dai-Ming Tang, Weijie Zhao, Huilong Xu, Leiqiang Chu, Yoshio Bando, Dmitri Golberg, and Goki Eda. Halide-assisted atmospheric pressure growth of large wse2 and ws2 monolayer crystals. *Applied Materials Today*, 1(1):60–66, 2015.

[121] Zhan Wang, Yong Xie, Haolin Wang, Ruixue Wu, Tang Nan, Yongjie Zhan, Jing Sun, Teng Jiang, Ying Zhao, Yimin Lei, et al. Nacl-assisted one-step growth of mos2–ws2 in-plane heterostructures. *Nanotechnology*, 28(32):325602, 2017.

[122] John R Ferraro. *Introductory raman spectroscopy*. Elsevier, 2003.

[123] Riichiro Saito, Y Tatsumi, Shengxi Huang, X Ling, and MS Dresselhaus. Raman spectroscopy of transition metal dichalcogenides. *Journal of Physics: Condensed Matter*, 28(35):353002, 2016.

[124] Changgu Lee, Hugen Yan, Louis E Brus, Tony F Heinz, James Hone, and Sunmin Ryu. Anomalous lattice vibrations of single-and few-layer mos2. *ACS nano*, 4(5):2695–2700, 2010.

[125] X Zhang, WP Han, JB Wu, Silvia Milana, Y Lu, QQ Li, AC Ferrari, and PH Tan. Raman spectroscopy of shear and layer breathing modes in multilayer mos 2. *Physical Review B*, 87(11):115413, 2013.

[126] Marcel Placidi, Mirjana Dimitrievska, Victor Izquierdo-Roca, Xavier Fontané, Andres Castellanos-Gomez, Amador Pérez-Tomás, Narcis Mestres, Moises Espindola-Rodriguez, Simon López-Marino, Markus Neuschitzer, et al. Multi-wavelength excitation raman scattering analysis of bulk and two-dimensional mos2: vibrational properties of atomically thin mos2 layers. *2D Materials*, 2(3):035006, 2015.

[127] Fang Liang, Hejun Xu, Xing Wu, Chaolun Wang, Chen Luo, and Jian Zhang. Raman spectroscopy characterization of two-dimensional materials. *Chinese Physics B*, 27(3):037802, 2018.

[128] Biswanath Chakraborty, Achintya Bera, DVS Muthu, Somnath Bhowmick, Umesh V Waghmare, and AK Sood. Symmetry-dependent phonon renormalization in monolayer mos 2 transistor. *Physical Review B*, 85(16):161403, 2012.

[129] Yumeng Shi, Jing-Kai Huang, Limin Jin, Yu-Te Hsu, Siu Fung Yu, Lain-Jong Li, and Hui Ying Yang. Selective decoration of au nanoparticles on monolayer mos2 single crystals. *Scientific reports*, 3(1):1–7, 2013.

[130] Sandro Mignuzzi, Andrew J Pollard, Nicola Bonini, Barry Brennan, Ian S Gilmore, Marcos A Pimenta, David Richards, and Debdulal Roy. Effect of disorder on raman scattering of single-layer mo s 2. *Physical Review B*, 91(19):195411, 2015.

[131] Wenjing Jie, Zhibin Yang, Gongxun Bai, and Jianhua Hao. Luminescence in 2d materials and van der waals heterostructures. *Advanced Optical Materials*, 6(10):1701296, 2018.

[132] HORIBA Scientific. Photoluminescence (pl) i& electroluminescence (el). `https://www.horiba.com/ind/scientific/technologies/photoluminescence-pl/photoluminescence-pl-electroluminescence-el/`.

[133] Agnieszka Kuc, Nourdine Zibouche, and Thomas Heine. Influence of quantum confinement on the electronic structure of the transition metal sulfide t s 2. *Physical Review B*, 83(24):245213, 2011.

[134] Minh Dao Tran, Ji-Hee Kim, and Young Hee Lee. Tailoring photoluminescence of monolayer transition metal dichalcogenides. *Current Applied Physics*, 16(9):1159–1174, 2016.

[135] Gerd Binnig, Calvin F Quate, and Ch Gerber. Atomic force microscope. *Physical review letters*, 56(9):930, 1986.

[136] Hang Zhang, Junxiang Huang, Yongwei Wang, Rui Liu, Xiulan Huai, Jingjing Jiang, and Chantelle Anfuso. Atomic force microscopy for two-dimensional materials: A tutorial review. *Optics Communications*, 406:3–17, 2018.

[137] Michael R Nellist, Yikai Chen, Andreas Mark, Sebastian Gödrich, Christian Stelling, Jingjing Jiang, Rakesh Poddar, Chunzeng Li, Ravi Kumar, Georg Papastavrou, et al. Atomic force microscopy with nanoelectrode tips for high resolution electrochemical, nanoadhesion and nanoelectrical imaging. *Nanotechnology*, 28(9):095711, 2017.

[138] Kenan Zhang, Tianning Zhang, Guanghui Cheng, Tianxin Li, Shuxia Wang, Wei Wei, Xiaohao Zhou, Weiwei Yu, Yan Sun, Peng Wang, et al. Interlayer transition and infrared photodetection in atomically thin type-ii mote2/mos2 van der waals heterostructures. *ACS nano*, 10(3):3852–3858, 2016.

[139] Philipp Tonndorf, Robert Schmidt, Philipp Böttger, Xiao Zhang, Janna Börner, Andreas Liebig, Manfred Albrecht, Christian Kloc, Ovidiu Gordan, Dietrich RT Zahn, et al. Photoluminescence emission and raman response of monolayer mos 2, mose 2, and wse 2. *Optics express*, 21(4):4908–4916, 2013.

[140] Weilie Zhou, Robert Apkarian, Zhong Lin Wang, and David Joy. Fundamentals of scanning electron microscopy (sem). In *Scanning microscopy for nanotechnology*, pages 1–40. Springer, 2006.

[141] Kalsoom Akhtar, Shahid Ali Khan, Sher Bahadar Khan, and Abdullah M Asiri. Scanning electron microscopy: Principle and applications in nanomaterials characterization. In *Handbook of materials characterization*, pages 113–145. Springer, 2018.

[142] David B Williams and C Barry Carter. The transmission electron microscope. In *Transmission electron microscopy*, pages 3–17. Springer, 1996.

[143] Linda E Franken, Kay Grünewald, Egbert J Boekema, and Marc CA Stuart. A technical introduction to transmission electron microscopy for soft-matter: Imaging, possibilities, choices, and technical developments. *Small*, 16(14):1906198, 2020.

[144] Yun-Yeong Chang, Heung Nam Han, and Miyoung Kim. Analyzing the microstructure and related properties of 2d materials by transmission electron microscopy. *Applied Microscopy*, 49(1):1–7, 2019.

[145] AK Raychaudhuri. Measurement of 1/f noise and its application in materials science. *Current opinion in solid state and materials science*, 6(1):67–85, 2002.

[146] Friits N Hooge. 1/f noise sources. *IEEE Transactions on electron devices*, 41(11):1926–1935, 1994.

[147] Alexander A Balandin. Low-frequency 1/f noise in graphene devices. *Nature nanotechnology*, 8(8):549–555, 2013.

[148] Vinod K Sangwan, Heather N Arnold, Deep Jariwala, Tobin J Marks, Lincoln J Lauhon, and Mark C Hersam. Low-frequency electronic noise in single-layer mos2 transistors. *Nano letters*, 13(9):4351–4355, 2013.

[149] FN Hooge and LKJ Vandamme. Lattice scattering causes 1/f noise. *Physics Letters A*, 66(4):315–316, 1978.

[150] Paritosh Karnatak, Tathagata Paul, Saurav Islam, and Arindam Ghosh. 1/f noise in van der waals materials and hybrids. *Advances in Physics: X*, 2(2):428–449, 2017.

[151] FN Hooge, TGM Kleinpenning, and Lode KJ Vandamme. Experimental studies on 1/f noise. *Reports on progress in Physics*, 44(5):479, 1981.

[152] R Fabian Pease and Stephen Y Chou. Lithography and other patterning techniques for future electronics. *Proceedings of the IEEE*, 96(2):248–270, 2008.

[153] Ekta Sharma, Reena Rathi, Jaya Misharwal, Bhavya Sinhmar, Suman Kumari, Jasvir Dalal, and Anand Kumar. Evolution in lithography techniques: Microlithography to nanolithography. *Nanomaterials*, 12(16):2754, 2022.

[154] Tahir Iqbal Awan, Almas Bashir, and Aqsa Tehseen. *Chemistry of Nanomaterials: Fundamentals and Applications*. Elsevier, 2020.

[155] S Franssila and L Sainiemi. Reactive ion etching (rie). In *Encyclopedia of Microfluidics and Nanofluidics*, pages 1772–1781. Springer Boston, MA, USA, 2008.

[156] James A Bondur. Dry process technology (reactive ion etching). *Journal of Vacuum Science and Technology*, 13(5):1023–1029, 1976.

[157] Ruben Mas-Balleste, Cristina Gomez-Navarro, Julio Gomez-Herrero, and Felix Zamora. 2d materials: to graphene and beyond. *Nanoscale*, 3(1):20–30, 2011.

[158] Konstantin S Novoselov, L Colombo, PR Gellert, MG Schwab, K Kim, et al. A roadmap for graphene. *nature*, 490(7419):192–200, 2012.

[159] Yoichi Kubota, Kenji Watanabe, Osamu Tsuda, and Takashi Taniguchi. Deep ultraviolet light-emitting hexagonal boron nitride synthesized at atmospheric pressure. *Science*, 317(5840):932–934, 2007.

[160] Liangzhi Kou, Changfeng Chen, and Sean C Smith. Phosphorene: fabrication, properties, and applications. *The journal of physical chemistry letters*, 6(14):2794–2805, 2015.

[161] Alessandro Molle, Carlo Grazianetti, Li Tao, Deepyanti Taneja, Md Hasibul Alam, and Deji Akinwande. Silicene, silicene derivatives, and their device applications. *Chemical Society Reviews*, 47(16):6370–6387, 2018.

[162] ME Dávila, Lede Xian, Seymur Cahangirov, Angel Rubio, and Guy Le Lay. Germanene: a novel two-dimensional germanium allotrope akin to graphene and silicene. *New Journal of Physics*, 16(9):095002, 2014.

[163] Jl A Wilson and AD Yoffe. The transition metal dichalcogenides discussion and interpretation of the observed optical, electrical and structural properties. *Advances in Physics*, 18(73):193–335, 1969.

[164] Ruitao Lv, Joshua A Robinson, Raymond E Schaak, Du Sun, Yifan Sun, Thomas E Mallouk, and Mauricio Terrones. Transition metal dichalcogenides and beyond: synthesis, properties, and applications of single-and few-layer nanosheets. *Accounts of chemical research*, 48(1):56–64, 2015.

[165] K Tsutsumi, Y Ishihara, and H Suzuki. Superconductivity in a layered transition-metal dichalcogenide 2h-tas2. *Solid state communications*, 74(10):1099–1101, 1990.

[166] Vitaly Podzorov, ME Gershenson, Ch Kloc, R Zeis, and E Bucher. High-mobility field-effect transistors based on transition metal dichalcogenides. *Applied Physics Letters*, 84(17):3301–3303, 2004.

[167] Andreas Pospischil, Marco M Furchi, and Thomas Mueller. Solar-energy conversion and light emission in an atomic monolayer p–n diode. *Nature nanotechnology*, 9(4):257–261, 2014.

[168] Shahriar Memaran, Nihar R Pradhan, Zhengguang Lu, Daniel Rhodes, Jonathan Ludwig, Qiong Zhou, Omotola Ogunsolu, Pulickel M Ajayan, Dmitry Smirnov, Antonio I Fernandez-Dominguez, et al. Pronounced photovoltaic response from multilayered transition-metal dichalcogenides pn-junctions. *Nano letters*, 15(11):7532–7538, 2015.

[169] Yang Li, Cheng-Yan Xu, Jia-Ying Wang, and Liang Zhen. Photodiode-like behavior and excellent photoresponse of vertical si/monolayer mos2 heterostructures. *Scientific reports*, 4(1):1–8, 2014.

[170] FHL Koppens, T Mueller, Ph Avouris, AC Ferrari, MS Vitiello, and M Polini. Photodetectors based on graphene, other two-dimensional materials and hybrid systems. *Nature nanotechnology*, 9(10):780–793, 2014.

[171] Hai Li, Zongyou Yin, Qiyuan He, Hong Li, Xiao Huang, Gang Lu, Derrick Wen Hui Fam, Alfred Iing Yoong Tok, Qing Zhang, and Hua Zhang. Fabrication of single-and multilayer mos2 film-based field-effect transistors for sensing no at room temperature. *small*, 8(1):63–67, 2012.

[172] Vinod K Sangwan, Deep Jariwala, In Soo Kim, Kan-Sheng Chen, Tobin J Marks, Lincoln J Lauhon, and Mark C Hersam. Gate-tunable memristive phenomena mediated by grain boundaries in single-layer mos2. *Nature nanotechnology*, 10(5):403–406, 2015.

[173] Goki Eda and Stefan A Maier. Two-dimensional crystals: managing light for optoelectronics. *ACS nano*, 7(7):5660–5665, 2013.

[174] Hualing Zeng, Junfeng Dai, Wang Yao, Di Xiao, and Xiaodong Cui. Valley polarization in mos2 monolayers by optical pumping. *Nature nanotechnology*, 7(8):490–493, 2012.

[175] Gábor Zsolt Magda, János Pető, Gergely Dobrik, Chanyong Hwang, László P Biró, and Levente Tapasztó. Exfoliation of large-area transition metal chalcogenide single layers. *Scientific reports*, 5(1):1–5, 2015.

[176] Valeria Nicolosi, Manish Chhowalla, Mercouri G Kanatzidis, Michael S Strano, and Jonathan N Coleman. Liquid exfoliation of layered materials. *Science*, 340(6139):1226419, 2013.

[177] Na Liu, Paul Kim, Ji Heon Kim, Jun Ho Ye, Sunkook Kim, and Cheol Jin Lee. Large-area atomically thin mos2 nanosheets prepared using electrochemical exfoliation. *ACS nano*, 8(7):6902–6910, 2014.

[178] Goki Eda, Hisato Yamaguchi, Damien Voiry, Takeshi Fujita, Mingwei Chen, and Manish Chhowalla. Photoluminescence from chemically exfoliated mos2. *Nano letters*, 11(12):5111–5116, 2011.

[179] Yi-Hsien Lee, Xin-Quan Zhang, Wenjing Zhang, Mu-Tung Chang, Cheng-Te Lin, Kai-Di Chang, Ya-Chu Yu, Jacob Tse-Wei Wang, Chia-Seng Chang, Lain-Jong Li, et al. Synthesis of large-area mos2 atomic layers with chemical vapor deposition. *Advanced materials*, 24(17):2320–2325, 2012.

[180] Jianyi Chen, Wei Tang, Bingbing Tian, Bo Liu, Xiaoxu Zhao, Yanpeng Liu, Tianhua Ren, Wei Liu, Dechao Geng, Hu Young Jeong, et al. Chemical vapor deposition of high-quality large-sized mos2 crystals on silicon dioxide substrates. *Advanced Science*, 3(8):1500033, 2016.

[181] Jaeho Jeon, Sung Kyu Jang, Su Min Jeon, Gwangwe Yoo, Yun Hee Jang, Jin-Hong Park, and Sungjoo Lee. Layer-controlled cvd growth of large-area two-dimensional mos 2 films. *Nanoscale*, 7(5):1688–1695, 2015.

[182] Deyi Fu, Xiaoxu Zhao, Yu-Yang Zhang, Linjun Li, Hai Xu, A-Rang Jang, Seong In Yoon, Peng Song, Sock Mui Poh, Tianhua Ren, et al. Molecular beam

epitaxy of highly crystalline monolayer molybdenum disulfide on hexagonal boron nitride. *Journal of the American Chemical Society*, 139(27):9392–9400, 2017.

[183] Arturo Valdivia, Douglas J Tweet, and John F Conley Jr. Atomic layer deposition of two dimensional mos2 on 150 mm substrates. *Journal of Vacuum Science & Technology A: Vacuum, Surfaces, and Films*, 34(2):021515, 2016.

[184] Junguang Tao, Jianwei Chai, Xin Lu, Lai Mun Wong, Ten It Wong, Jisheng Pan, Qihua Xiong, Dongzhi Chi, and Shijie Wang. Growth of wafer-scale mos 2 monolayer by magnetron sputtering. *Nanoscale*, 7(6):2497–2503, 2015.

[185] Xidong Duan, Chen Wang, Jonathan C Shaw, Rui Cheng, Yu Chen, Honglai Li, Xueping Wu, Ying Tang, Qinling Zhang, Anlian Pan, et al. Lateral epitaxial growth of two-dimensional layered semiconductor heterojunctions. *Nature nanotechnology*, 9(12):1024–1030, 2014.

[186] Ming-Yang Li, Yumeng Shi, Chia-Chin Cheng, Li-Syuan Lu, Yung-Chang Lin, Hao-Lin Tang, Meng-Lin Tsai, Chih-Wei Chu, Kung-Hwa Wei, Jr-Hau He, et al. Epitaxial growth of a monolayer wse2-mos2 lateral pn junction with an atomically sharp interface. *Science*, 349(6247):524–528, 2015.

[187] Li Tao, Kun Chen, Zefeng Chen, Wenjun Chen, Xuchun Gui, Huanjun Chen, Xinming Li, and Jian-Bin Xu. Centimeter-scale cvd growth of highly crystalline single-layer mos2 film with spatial homogeneity and the visualization of grain boundaries. *ACS applied materials & interfaces*, 9(13):12073–12081, 2017.

[188] Yifei Yu, Chun Li, Yi Liu, Liqin Su, Yong Zhang, and Linyou Cao. Controlled scalable synthesis of uniform, high-quality monolayer and few-layer mos2 films. *Scientific reports*, 3(1):1–6, 2013.

[189] Yongjie Zhan, Zheng Liu, Sina Najmaei, Pulickel M Ajayan, and Jun Lou. Large-area vapor-phase growth and characterization of mos2 atomic layers on a sio2 substrate. *Small*, 8(7):966–971, 2012.

[190] Kathleen M McCreary, Aubrey T Hanbicki, Jeremy T Robinson, Enrique Cobas, James C Culbertson, Adam L Friedman, Glenn G Jernigan, and Berend T Jonker. Large-area synthesis of continuous and uniform mos2 monolayer films on graphene. *Advanced Functional Materials*, 24(41):6449–6454, 2014.

[191] Keng-Ku Liu, Wenjing Zhang, Yi-Hsien Lee, Yu-Chuan Lin, Mu-Tung Chang, Ching-Yuan Su, Chia-Seng Chang, Hai Li, Yumeng Shi, Hua Zhang, et al. Growth of large-area and highly crystalline mos2 thin layers on insulating substrates. *Nano letters*, 12(3):1538–1544, 2012.

[192] Ananth Govind Rajan, Jamie H Warner, Daniel Blankschtein, and Michael S Strano. Generalized mechanistic model for the chemical vapor deposition of 2d transition metal dichalcogenide monolayers. *ACS nano*, 10(4):4330–4344, 2016.

[193] Yuping Shi, Pengfei Yang, Shaolong Jiang, Zhepeng Zhang, Yahuan Huan, Chunyu Xie, Min Hong, Jianping Shi, and Yanfeng Zhang. Na-assisted fast growth of large single-crystal mos2 on sapphire. *Nanotechnology*, 30(3):034002, 2018.

[194] Kehao Zhang, Brian M Bersch, Fu Zhang, Natalie C Briggs, Shruti Subramanian, Ke Xu, Mikhail Chubarov, Ke Wang, Jordan O Lerach, Joan M Redwing, et al. Considerations for utilizing sodium chloride in epitaxial molybdenum disulfide. *ACS applied materials & interfaces*, 10(47):40831–40837, 2018.

[195] Sina Najmaei, Zheng Liu, Wu Zhou, Xiaolong Zou, Gang Shi, Sidong Lei, Boris I Yakobson, Juan-Carlos Idrobo, Pulickel M Ajayan, and Jun Lou.

Vapour phase growth and grain boundary structure of molybdenum disulphide atomic layers. *Nature materials*, 12(8):754–759, 2013.

[196] Yong Xie, Xiaohua Ma, Zhan Wang, Tang Nan, Ruixue Wu, Peng Zhang, Haolin Wang, Yabin Wang, Yongjie Zhan, and Yue Hao. Nacl-assisted cvd synthesis, transfer and persistent photoconductivity properties of two-dimensional transition metal dichalcogenides. *MRS Advances*, 3(6-7):365–371, 2018.

[197] HoKwon Kim, Dmitry Ovchinnikov, Davide Deiana, Dmitrii Unuchek, and Andras Kis. Suppressing nucleation in metal–organic chemical vapor deposition of mos2 monolayers by alkali metal halides. *Nano letters*, 17(8):5056–5063, 2017.

[198] Gustavo A Lara Saenz, Chandan Biswas, Hisato Yamaguchi, Claudia Narvaez Villarrubia, Aditya D Mohite, and Anupama B Kaul. Effects of synthesis parameters on cvd molybdenum disulfide growth. *MRS Advances*, 1(32):2291–2296, 2016.

[199] Hong Li, Qing Zhang, Chin Chong Ray Yap, Beng Kang Tay, Teo Hang Tong Edwin, Aurelien Olivier, and Dominique Baillargeat. From bulk to monolayer mos2: evolution of raman scattering. *Advanced Functional Materials*, 22(7):1385–1390, 2012.

[200] NT McDevitt, JS Zabinski, MS Donley, and JE Bultman. Disorder-induced low-frequency raman band observed in deposited mos2 films. *Applied spectroscopy*, 48(6):733–736, 1994.

[201] Gitti L Frey, Reshef Tenne, Manyalibo J Matthews, MS Dresselhaus, and G Dresselhaus. Raman and resonance raman investigation of mos 2 nanoparticles. *Physical Review B*, 60(4):2883, 1999.

[202] Arend M Van Der Zande, Pinshane Y Huang, Daniel A Chenet, Timothy C Berkelbach, YuMeng You, Gwan-Hyoung Lee, Tony F Heinz, David R Reichman, David A Muller, and James C Hone. Grains and grain boundaries in highly crystalline monolayer molybdenum disulphide. *Nature materials*, 12(6):554–561, 2013.

[203] Wenfeng Wang, Haibo Shu, Jun Wang, Yecheng Cheng, Pei Liang, and Xiaoshuang Chen. Defect passivation and photoluminescence enhancement of monolayer mos2 crystals through sodium halide-assisted chemical vapor deposition growth. *ACS applied materials & interfaces*, 12(8):9563–9571, 2020.

[204] Hao Qiu, Tao Xu, Zilu Wang, Wei Ren, Haiyan Nan, Zhenhua Ni, Qian Chen, Shijun Yuan, Feng Miao, Fengqi Song, et al. Hopping transport through defect-induced localized states in molybdenum disulphide. *Nature communications*, 4(1):1–6, 2013.

[205] Dattatray J Late, Bin Liu, HSS Ramakrishna Matte, Vinayak P Dravid, and CNR Rao. Hysteresis in single-layer mos2 field effect transistors. *ACS nano*, 6(6):5635–5641, 2012.

[206] Matin Amani, Matthew L Chin, A Glen Birdwell, Terrance P O'Regan, Sina Najmaei, Zheng Liu, Pulickel M Ajayan, Jun Lou, and Madan Dubey. Electrical performance of monolayer mos2 field-effect transistors prepared by chemical vapor deposition. *Applied Physics Letters*, 102(19):193107, 2013.

[207] Fei Chen and Weitao Su. The effect of the experimental parameters on the growth of mos 2 flakes. *CrystEngComm*, 20(33):4823–4830, 2018.

[208] S Chaitoglou and E Bertran. Effect of pressure and hydrogen flow in nucleation density and morphology of graphene bidimensional crystals. *Materials Research Express*, 3(7):075603, 2016.

[209] Stefanos Chaitoglou, Polychronis Tsipas, Thanassis Speliotis, George Kordas, Antonios Vavouliotis, and Athanasios Dimoulas. Insight and control of the chemical vapor deposition growth parameters and morphological characteristics of graphene/mo2c heterostructures over liquid catalyst. *Journal of Crystal Growth*, 495:46–53, 2018.

[210] Jiawen You, Md Delowar Hossain, and Zhengtang Luo. Synthesis of 2d transition metal dichalcogenides by chemical vapor deposition with controlled layer number and morphology. *Nano Convergence*, 5(1):1–13, 2018.

[211] Yang Xu, Connor Horn, Jiacheng Zhu, Yanhao Tang, Liguo Ma, Lizhong Li, Song Liu, Kenji Watanabe, Takashi Taniguchi, James C Hone, et al. Creation of moiré bands in a monolayer semiconductor by spatially periodic dielectric screening. *Nature Materials*, 20(5):645–649, 2021.

[212] Wu Zhou, Xiaolong Zou, Sina Najmaei, Zheng Liu, Yumeng Shi, Jing Kong, Jun Lou, Pulickel M Ajayan, Boris I Yakobson, and Juan-Carlos Idrobo. Intrinsic structural defects in monolayer molybdenum disulfide. *Nano letters*, 13(6):2615–2622, 2013.

[213] Zhangting Wu and Zhenhua Ni. Spectroscopic investigation of defects in two-dimensional materials. *Nanophotonics*, 6(6):1219–1237, 2017.

[214] Penghong Ci, Xuezeng Tian, Jun Kang, Anthony Salazar, Kazutaka Eriguchi, Sarah Warkander, Kechao Tang, Jiaman Liu, Yabin Chen, Sefaattin Tongay, et al. Chemical trends of deep levels in van der waals semiconductors. *Nature communications*, 11(1):1–8, 2020.

[215] Jie Jiang, Chongyi Ling, Tao Xu, Wenhui Wang, Xianghong Niu, Amina Zafar, Zhenzhong Yan, Xiaomu Wang, Yumeng You, Litao Sun, et al. Defect engineering for modulating the trap states in 2d photoconductors. *Advanced Materials*, 30(40):1804332, 2018.

[216] Fang Chen, Jilin Xia, David K Ferry, and Nongjian Tao. Dielectric screening enhanced performance in graphene fet. *Nano letters*, 9(7):2571–2574, 2009.

[217] Aniruddha Konar, Tian Fang, and Debdeep Jena. Effect of high-κ gate dielectrics on charge transport in graphene-based field effect transistors. *Physical Review B*, 82(11):115452, 2010.

[218] Jian-Hao Chen, Chaun Jang, Shudong Xiao, Masa Ishigami, and Michael S Fuhrer. Intrinsic and extrinsic performance limits of graphene devices on sio2. *Nature nanotechnology*, 3(4):206–209, 2008.

[219] Damon B Farmer, Hsin-Ying Chiu, Yu-Ming Lin, Keith A Jenkins, Fengnian Xia, and Phaedon Avouris. Utilization of a buffered dielectric to achieve high field-effect carrier mobility in graphene transistors. *Nano letters*, 9(12):4474–4478, 2009.

[220] Aniruddha Konar. *Electronic and optical properties of low dimensional systems: Effect of the dielectric environment*. University of Notre Dame, 2011.

[221] Jessamine Ng Lee, Cheolmin Park, and George M Whitesides. Solvent compatibility of poly (dimethylsiloxane)-based microfluidic devices. *Analytical chemistry*, 75(23):6544–6554, 2003.

[222] KC Santosh, Roberto C Longo, Rafik Addou, Robert M Wallace, and Kyeongjae Cho. Impact of intrinsic atomic defects on the electronic structure of mos2 monolayers. *Nanotechnology*, 25(37):375703, 2014.

[223] KR Olasupo and MK Hatalis. Leakage current mechanism in sub-micron polysilicon thin-film transistors. *IEEE Transactions on Electron Devices*, 43(8):1218–1223, 1996.

[224] Song-Lin Li, Kazuhito Tsukagoshi, Emanuele Orgiu, and Paolo Samorì. Charge transport and mobility engineering in two-dimensional transition metal chalcogenide semiconductors. *Chemical Society Reviews*, 45(1):118–151, 2016.

[225] C Jang, Shaffique Adam, J-H Chen, Ellen D Williams, S Das Sarma, and MS Fuhrer. Tuning the effective fine structure constant in graphene: Opposing effects of dielectric screening on short-and long-range potential scattering. *Physical review letters*, 101(14):146805, 2008.

[226] Shaffique Adam and S Das Sarma. Boltzmann transport and residual conductivity in bilayer graphene. *Physical Review B*, 77(11):115436, 2008.

[227] Anthony Ayari, Enrique Cobas, Ololade Ogundadegbe, and Michael S Fuhrer. Realization and electrical characterization of ultrathin crystals of layered transition-metal dichalcogenides. *Journal of applied physics*, 101(1):014507, 2007.

[228] Lihua Fu, Hai Lu, Dunjun Chen, Rong Zhang, Youdou Zheng, Tangsheng Chen, Ke Wei, and Xinyu Liu. Field-dependent carrier trapping induced kink effect in algan/gan high electron mobility transistors. *Applied Physics Letters*, 98(17):173508, 2011.

[229] Laurent Brunel, Nathalie Malbert, Arnaud Curutchet, Nathalie Labat, and Benoit Lambert. Kink effect characterization in algan/gan hemts by dc and drain current transient measurements. In *2012 Proceedings of the European Solid-State Device Research Conference (ESSDERC)*, pages 270–273. IEEE, 2012.

[230] Saptarshi Das. Two dimensional electrostrictive field effect transistor (2d-efet): a sub-60mv/decade steep slope device with high on current. *Scientific reports*, 6(1):1–7, 2016.

[231] Albert Rose. Performance of photoconductors. *Proceedings of the IRE*, 43(12):1850–1869, 1955.

[232] Alexey Chernikov, Arend M Van Der Zande, Heather M Hill, Albert F Rigosi, Ajanth Velauthapillai, James Hone, and Tony F Heinz. Electrical tuning of exciton binding energies in monolayer ws 2. *Physical review letters*, 115(12):126802, 2015.

[233] Keliang He, Nardeep Kumar, Liang Zhao, Zefang Wang, Kin Fai Mak, Hui Zhao, and Jie Shan. Tightly bound excitons in monolayer wse 2. *Physical review letters*, 113(2):026803, 2014.

[234] Bairen Zhu, Xi Chen, and Xiaodong Cui. Exciton binding energy of monolayer ws2. *Scientific reports*, 5(1):1–5, 2015.

[235] Etienne Lorchat, Luis E Parra López, Cédric Robert, Delphine Lagarde, Guillaume Froehlicher, Takashi Taniguchi, Kenji Watanabe, Xavier Marie, and Stéphane Berciaud. Filtering the photoluminescence spectra of atomically thin semiconductors with graphene. *Nature Nanotechnology*, 15(4):283–288, 2020.

[236] Yuto Kajino, Kenichi Oto, and Yasuhiro Yamada. Modification of optical properties in monolayer ws2 on dielectric substrates by coulomb engineering. *The Journal of Physical Chemistry C*, 123(22):14097–14102, 2019.

[237] Archana Raja, Lutz Waldecker, Jonas Zipfel, Yeongsu Cho, Samuel Brem, Jonas D Ziegler, Marvin Kulig, Takashi Taniguchi, Kenji Watanabe, Ermin Malic, et al. Dielectric disorder in two-dimensional materials. *Nature nanotechnology*, 14(9):832–837, 2019.

[238] Chunlei Wan, Yumi Kodama, Mami Kondo, Ryo Sasai, Xin Qian, Xiaokun Gu, Kenji Koga, Kazuhisa Yabuki, Ronggui Yang, and Kunihito Koumoto.

Dielectric mismatch mediates carrier mobility in organic-intercalated layered tis2. *Nano letters*, 15(10):6302–6308, 2015.

[239] Yuan Liu, Yu Huang, and Xiangfeng Duan. Van der waals integration before and beyond two-dimensional materials. *Nature*, 567(7748):323–333, 2019.

[240] Adrien Allain, Jiahao Kang, Kaustav Banerjee, and Andras Kis. Electrical contacts to two-dimensional semiconductors. *Nature materials*, 14(12):1195–1205, 2015.

[241] Deblina Sarkar, Xuejun Xie, Wei Liu, Wei Cao, Jiahao Kang, Yongji Gong, Stephan Kraemer, Pulickel M Ajayan, and Kaustav Banerjee. A sub-thermionic tunnel field-effect transistor with an atomically thin channel. *Nature*, 526(7571):91–95, 2015.

[242] Liu Wang, Jiansheng Jie, Zhibin Shao, Qing Zhang, Xiaohong Zhang, Yuming Wang, Zheng Sun, and Shuit-Tong Lee. Mos2/si heterojunction with vertically standing layered structure for ultrafast, high-detectivity, self-driven visible–near infrared photodetectors. *Advanced Functional Materials*, 25(19):2910–2919, 2015.

[243] Yan Zhang, Yongqiang Yu, Longfei Mi, Hui Wang, Zhifeng Zhu, Qingyun Wu, Yugang Zhang, and Yang Jiang. In situ fabrication of vertical multilayered mos2/si homotype heterojunction for high-speed visible–near-infrared photodetectors. *Small*, 12(8):1062–1071, 2016.

[244] Shuang Qiao, Ridong Cong, Jihong Liu, Baolai Liang, Guangsheng Fu, Wei Yu, Kailiang Ren, Shufang Wang, and Caofeng Pan. A vertically layered mos 2/si heterojunction for an ultrahigh and ultrafast photoresponse photodetector. *Journal of Materials Chemistry C*, 6(13):3233–3239, 2018.

[245] Mohammad R Esmaeili-Rad and Sayeef Salahuddin. High performance molybdenum disulfide amorphous silicon heterojunction photodetector. *Scientific reports*, 3(1):1–6, 2013.

[246] Feng Wu, Qing Li, Peng Wang, Hui Xia, Zhen Wang, Yang Wang, Man Luo, Long Chen, Fansheng Chen, Jinshui Miao, et al. High efficiency and fast van der waals hetero-photodiodes with a unilateral depletion region. *Nature communications*, 10(1):1–8, 2019.

[247] Lanzhong Hao, Yunjie Liu, Wei Gao, Zhide Han, Qingzhong Xue, Huizhong Zeng, Zhipeng Wu, Jun Zhu, and Wanli Zhang. Electrical and photovoltaic characteristics of mos2/si pn junctions. *Journal of Applied Physics*, 117(11):114502, 2015.

[248] Sangram K Pradhan, Bo Xiao, and Aswini K Pradhan. Enhanced photoresponse in p-si/mos2 heterojunction-based solar cells. *Solar Energy Materials and Solar Cells*, 144:117–127, 2016.

[249] Marco M Furchi, Florian Höller, Lukas Dobusch, Dmitry K Polyushkin, Simone Schuler, and Thomas Mueller. Device physics of van der waals heterojunction solar cells. *npj 2D Materials and Applications*, 2(1):1–7, 2018.

[250] Monika Moun and Rajendra Singh. Exploring conduction mechanism and photoresponse in p-gan/n-mos2 heterojunction diode. *Journal of Applied Physics*, 127(13):135702, 2020.

[251] Marco Bernardi, Maurizia Palummo, and Jeffrey C Grossman. Extraordinary sunlight absorption and one nanometer thick photovoltaics using two-dimensional monolayer materials. *Nano letters*, 13(8):3664–3670, 2013.

[252] Sayak Bhattacharya and Sajeev John. Beyond 30% conversion efficiency in silicon solar cells: a numerical demonstration. *Scientific reports*, 9(1):12482, 2019.

[253] T Takahagi, I Nagai, A Ishitani, H Kuroda, and Y Nagasawa. The formation of hydrogen passivated silicon single-crystal surfaces using ultraviolet cleaning and hf etching. *Journal of applied physics*, 64(7):3516–3521, 1988.

[254] Kai Liu, Qimin Yan, Michelle Chen, Wen Fan, Yinghui Sun, Joonki Suh, Deyi Fu, Sangwook Lee, Jian Zhou, Sefaattin Tongay, et al. Elastic properties of chemical-vapor-deposited monolayer mos2, ws2, and their bilayer heterostructures. *Nano letters*, 14(9):5097–5103, 2014.

[255] Shanshan Wang, Xiaochen Wang, and Jamie H Warner. All chemical vapor deposition growth of mos2: h-bn vertical van der waals heterostructures. *ACS nano*, 9(5):5246–5254, 2015.

[256] Veerendra Dhyani and Samaresh Das. High-speed scalable silicon-mos2 pn heterojunction photodetectors. *Scientific reports*, 7(1):1–9, 2017.

[257] Subhash Chand and Jitendra Kumar. Effects of barrier height distribution on the behavior of a schottky diode. *Journal of applied physics*, 82(10):5005–5010, 1997.

[258] Uli Würfel, Dieter Neher, Annika Spies, and Steve Albrecht. Impact of charge transport on current–voltage characteristics and power-conversion efficiency of organic solar cells. *Nature communications*, 6(1):1–9, 2015.

[259] Dieter Neher, Juliane Kniepert, Arik Elimelech, and L Koster. A new figure of merit for organic solar cells with transport-limited photocurrents. *Scientific reports*, 6(1):1–9, 2016.

[260] Subhrajit Mukherjee, Rishi Maiti, Ajit K Katiyar, Soumen Das, and Samit K Ray. Novel colloidal mos2 quantum dot heterojunctions on silicon platforms for multifunctional optoelectronic devices. *Scientific reports*, 6(1):1–11, 2016.

[261] Daniel S Schneider, Annika Grundmann, Andreas Bablich, Vikram Passi, Satender Kataria, Holger Kalisch, Michael Heuken, Andrei Vescan, Daniel Neumaier, and Max C Lemme. Highly responsive flexible photodetectors based on movpe grown uniform few-layer mos2. *ACS Photonics*, 7(6):1388–1395, 2020.

[262] Gerasimos Konstantatos, Larissa Levina, Armin Fischer, and Edward H Sargent. Engineering the temporal response of photoconductive photodetectors via selective introduction of surface trap states. *Nano letters*, 8(5):1446–1450, 2008.

[263] Osmarie Martinez, Ariana G Bravo, and Nicholas J Pinto. Fabrication of poly (vinylidene fluoride- trifluoroethylene)/poly (3, 4-ethylenedioxythiophene)-polystyrene sulfonate composite nanofibers via electrospinning. *Macromolecules*, 42(20):7924–7929, 2009.

[264] Xiaodong Li, Zhi Wang, Zemin Zhang, Lulu Chen, Jianli Cheng, Wei Ni, Bin Wang, and Erqing Xie. Light illuminated α- fe2o3/pt nanoparticles as water activation agent for photoelectrochemical water splitting. *Scientific reports*, 5(1):1–7, 2015.

[265] Ali Can Zaman and Cengiz Kaya. Determination of quantity of materials in suspensions and in electrophoretic coatings by uv-visible absorption spectroscopy. *Journal of The Electrochemical Society*, 162(11):D3109, 2015.

[266] Yoshizo Kawaguchi, Hideki Ohmura, and Tadatake Sato. Detection of trace substances adhered to a metal surface by laser-induced breakdown spectroscopy. *Journal of Analytical Atomic Spectrometry*, 32(3):609–615, 2017.

[267] IG Hill, A Kahn, ZG Soos, and RA Pascal Jr. Charge-separation energy in films of π-conjugated organic molecules. *Chemical Physics Letters*, 327(3-4):181–188, 2000.

[268] Sibel Y Leblebici, Teresa L Chen, Paul Olalde-Velasco, Wanli Yang, and Biwu Ma. Reducing exciton binding energy by increasing thin film permittivity: an effective approach to enhance exciton separation efficiency in organic solar cells. *ACS applied materials & interfaces*, 5(20):10105–10110, 2013.

[269] Andrey R Klots, Benjamin Weintrub, Dhiraj Prasai, Daniel Kidd, Kalman Varga, Kirill A Velizhanin, and Kirill I Bolotin. Controlled dynamic screening of excitonic complexes in 2d semiconductors. *Scientific reports*, 8(1):1–8, 2018.

[270] Byeong-Cheol Kang and Tae-Jun Ha. The improved performance of molybdenum disulphide thin-film transistors operating at low voltages by solution-processed fluorocarbon encapsulation. *Electronic Materials Letters*, 15(4):391–395, 2019.

[271] M Goryca, Jing Li, Andreas V Stier, Takashi Taniguchi, Kenji Watanabe, Emmanuel Courtade, Shivangi Shree, Cedric Robert, Bernhard Urbaszek, Xavier Marie, et al. Revealing exciton masses and dielectric properties of monolayer semiconductors with high magnetic fields. *Nature communications*, 10(1):1–12, 2019.

[272] Sven Borghardt, Jhih-Sian Tu, Florian Winkler, Jürgen Schubert, Willi Zander, Kristjan Leosson, and Beata E Kardynał. Engineering of optical and electronic band gaps in transition metal dichalcogenide monolayers through external dielectric screening. *Physical review materials*, 1(5):054001, 2017.

[273] Diana Y Qiu, Felipe H da Jornada, and Steven G Louie. Environmental screening effects in 2d materials: renormalization of the bandgap, electronic

structure, and optical spectra of few-layer black phosphorus. *Nano letters*, 17(8):4706–4712, 2017.

[274] Andreas V Stier, Nathan P Wilson, Genevieve Clark, Xiaodong Xu, and Scott A Crooker. Probing the influence of dielectric environment on excitons in monolayer wse2: insight from high magnetic fields. *Nano letters*, 16(11):7054–7060, 2016.

[275] Hannu-Pekka Komsa and Arkady V Krasheninnikov. Effects of confinement and environment on the electronic structure and exciton binding energy of mos 2 from first principles. *Physical Review B*, 86(24):241201, 2012.

[276] Simone Latini, Thomas Olsen, and Kristian Sommer Thygesen. Excitons in van der waals heterostructures: The important role of dielectric screening. *Physical Review B*, 92(24):245123, 2015.

[277] Ilkka Kylänpää and Hannu-Pekka Komsa. Binding energies of exciton complexes in transition metal dichalcogenide monolayers and effect of dielectric environment. *Physical Review B*, 92(20):205418, 2015.

[278] AKM Newaz, Yevgeniy S Puzyrev, Bin Wang, Sokrates T Pantelides, and Kirill I Bolotin. Probing charge scattering mechanisms in suspended graphene by varying its dielectric environment. *Nature communications*, 3(1):1–6, 2012.

[279] Jinshui Miao, Xiwen Liu, Kiyoung Jo, Kang He, Ravindra Saxena, Baokun Song, Huiqin Zhang, Jiale He, Myung-Geun Han, Weida Hu, et al. Gate-tunable semiconductor heterojunctions from 2d/3d van der waals interfaces. *Nano Letters*, 20(4):2907–2915, 2020.

[280] Haining Wang, Changjian Zhang, and Farhan Rana. Ultrafast dynamics of defect-assisted electron–hole recombination in monolayer mos2. *Nano letters*, 15(1):339–345, 2015.

[281] Haining Wang, Jared H Strait, Changjian Zhang, Weimin Chan, Christina Manolatou, Sandip Tiwari, and Farhan Rana. Fast exciton annihilation by capture of electrons or holes by defects via auger scattering in monolayer metal dichalcogenides. *Physical Review B*, 91(16):165411, 2015.

[282] Wenjing Zhang, Jing-Kai Huang, Chang-Hsiao Chen, Yung-Huang Chang, Yuh-Jen Cheng, and Lain-Jong Li. High-gain phototransistors based on a cvd mos2 monolayer. *Advanced materials*, 25(25):3456–3461, 2013.

[283] Zhaodong Chu, Chun-Yuan Wang, Jiamin Quan, Chenhui Zhang, Chao Lei, Ali Han, Xuejian Ma, Hao-Ling Tang, Dishan Abeysinghe, Matthew Staab, et al. Unveiling defect-mediated carrier dynamics in monolayer semiconductors by spatiotemporal microwave imaging. *Proceedings of the National Academy of Sciences*, 117(25):13908–13913, 2020.

[284] Vrinda Narayanan P, Gokul MA, Tamaghna Chowdhury, Chandan K Singh, Shailendra Kumar Chaubey, Takashi Taniguchi, Kenji Watanabe, Mukul Kabir, GV Pavan Kumar, and Atikur Rahman. Giant photoresponse enhancement in mixed-dimensional van der waals heterostructure through dielectric engineering. *Advanced Materials Interfaces*, 9(9):2102054, 2022.

[285] MA Gokul, Vrinda Narayanan, and Atikur Rahman. Modulating flow near substrate surface to grow clean and large-area monolayer mos2. *Nanotechnology*, 31(41):415706, 2020.

[286] Vrinda Narayanan, MA Gokul, and Atikur Rahman. How to 'train'your cvd to grow large-area 2d materials. *Materials Research Express*, 6(12):125002, 2019.

[287] Alper Gurarslan, Yifei Yu, Liqin Su, Yiling Yu, Francisco Suarez, Shanshan Yao, Yong Zhu, Mehmet Ozturk, Yong Zhang, and Linyou Cao. Surface-energy-assisted perfect transfer of centimeter-scale monolayer and few-layer mos2 films onto arbitrary substrates. *ACS nano*, 8(11):11522–11528, 2014.

[288] Fucai Liu, Wai Leong Chow, Xuexia He, Peng Hu, Shoujun Zheng, Xingli Wang, Jiadong Zhou, Qundong Fu, Wei Fu, Peng Yu, et al. Van der waals p–n junction based on an organic–inorganic heterostructure. *Advanced Functional Materials*, 25(36):5865–5871, 2015.

[289] Jae-Keun Kim, Kyungjune Cho, Tae-Young Kim, Jinsu Pak, Jingon Jang, Younggul Song, Youngrok Kim, Barbara Yuri Choi, Seungjun Chung, Woong-Ki Hong, et al. Trap-mediated electronic transport properties of gate-tunable pentacene/mos2 pn heterojunction diodes. *Scientific reports*, 6(1):1–8, 2016.

[290] Daowei He, Yiming Pan, Haiyan Nan, Shuai Gu, Ziyi Yang, Bing Wu, Xiaoguang Luo, Bingchen Xu, Yuhan Zhang, Yun Li, et al. A van der waals pn heterojunction with organic/inorganic semiconductors. *Applied Physics Letters*, 107(18):183103, 2015.

[291] Pradeep Desai, Ajinkya K Ranade, Rakesh Mahyavanshi, Masaki Tanemura, and Golap Kalita. Influence of mos2-silicon interface states on spectral photoresponse characteristics. *physica status solidi (a)*, 216(18):1900349, 2019.

[292] Peirui Ji, Shuming Yang, Yu Wang, Kaili Li, Yiming Wang, Hao Suo, Yonas Tesfaye Woldu, Xiaomin Wang, Fei Wang, Liangliang Zhang, et al. High-performance photodetector based on an interface engineering-assisted graphene/silicon schottky junction. *Microsystems & nanoengineering*, 8(1):1–9, 2022.

[293] Johan Verschraegen, Marc Burgelman, and Jürgen Penndorf. Temperature dependence of the diode ideality factor in cuins2-on-cu-tape solar cells. *Thin Solid Films*, 480:307–311, 2005.

[294] A Sertap Kavasoglu, Fahrettin Yakuphanoglu, Nese Kavasoglu, Osman Pakma, Ozcan Birgi, and Sener Oktik. The analysis of the charge transport mecha-

nism of n-si/meh-ppv device structure using forward bias i–v–t characteristics. *Journal of alloys and compounds*, 492(1-2):421–426, 2010.

[295] Md Nazrul Islam, Sanjay K Ram, and Satyendra Kumar. Band edge discontinuities and carrier transport in c-si/porous silicon heterojunctions. *Journal of Physics D: Applied Physics*, 40(19):5840, 2007.

[296] J Osvald. Temperature dependence of barrier height parameters of inhomogeneous schottky diodes. *Microelectronic Engineering*, 86(1):117–120, 2009.

[297] Noel C Giebink, Gary P Wiederrecht, Michael R Wasielewski, and Stephen R Forrest. Ideal diode equation for organic heterojunctions. i. derivation and application. *Physical Review B*, 82(15):155305, 2010.

[298] TP Chen, TC Lee, CC Ling, CD Beling, and S Fung. Current transport and its effect on the determination of the schottky-barrier height in a typical system: Gold on silicon. *Solid-state electronics*, 36(7):949–954, 1993.

[299] MALİK Kaya, HİDAYET Çetin, B Boyarbay, A Gök, and ENİSE Ayyildiz. Temperature dependence of the current–voltage characteristics of sn/pani/p-si/al heterojunctions. *Journal of Physics: Condensed Matter*, 19(40):406205, 2007.

[300] Manisha Tyagi, Monika Tomar, and Vinay Gupta. Trap assisted space charge conduction in p-nio/n-zno heterojunction diode. *Materials Research Bulletin*, 66:123–131, 2015.

[301] Sujoy Ghosh, Andrew Winchester, Baleeswaraiah Muchharla, Milinda Wasala, Simin Feng, Ana Laura Elias, M Krishna, Takaaki Harada, Catherine Chin, Keshav Dani, et al. Ultrafast intrinsic photoresponse and direct evidence of sub-gap states in liquid phase exfoliated mos2thin films. *Scientific reports*, 5(1):1–8, 2015.

[302] Albert Rose. *Concepts in photoconductivity and allied problems*. Number 19. Interscience publishers, 1963.

[303] J Renteria, R Samnakay, SL Rumyantsev, P Goli, MS Shur, and AA Balandin. Low-frequency 1/f noise in molybdenum disulfide transistors. *arXiv preprint arXiv:1312.6868*, 2013.

[304] Bing Zhang, Congzhen Hu, Youze Xin, Yaoxin Li, Yiyun Xie, Qian Xing, Zhuoqi Guo, Zhongming Xue, Dan Li, Guohe Zhang, et al. Analysis of low-frequency 1/f noise characteristics for mote2 ambipolar field-effect transistors. *Nanomaterials*, 12(8):1325, 2022.

[305] DV Kuksenkov, H Temkin, A Osinsky, R Gaska, and MA Khan. Origin of conductivity and low-frequency noise in reverse-biased gan pn junction. *Applied physics letters*, 72(11):1365–1367, 1998.

[306] Hao Jiang, Jingxuan Wei, Feiying Sun, Changbin Nie, Jintao Fu, Haofei Shi, Jiuxun Sun, Xingzhan Wei, and Cheng-Wei Qiu. Enhanced photogating effect in graphene photodetectors via potential fluctuation engineering. *ACS nano*, 16(3):4458–4466, 2022.

[307] Kathleen M McCreary, Aubrey T Hanbicki, Saujan V Sivaram, and Berend T Jonker. A-and b-exciton photoluminescence intensity ratio as a measure of sample quality for transition metal dichalcogenide monolayers. *Apl Materials*, 6(11):111106, 2018.

[308] Kin Fai Mak and Jie Shan. Photonics and optoelectronics of 2d semiconductor transition metal dichalcogenides. *Nature Photonics*, 10(4):216–226, 2016.

[309] Bang Lin Li, Jinping Wang, Hao Lin Zou, Slaven Garaj, Chwee Teck Lim, Jianping Xie, Nian Bing Li, and David Tai Leong. Low-dimensional transi-

tion metal dichalcogenide nanostructures based sensors. *Advanced Functional Materials*, 26(39):7034–7056, 2016.

[310] Andres Castellanos-Gomez, Rafael Roldán, Emmanuele Cappelluti, Michele Buscema, Francisco Guinea, Herre SJ van der Zant, and Gary A Steele. Local strain engineering in atomically thin mos2. *Nano letters*, 13(11):5361–5366, 2013.

[311] John R Schaibley, Hongyi Yu, Genevieve Clark, Pasqual Rivera, Jason S Ross, Kyle L Seyler, Wang Yao, and Xiaodong Xu. Valleytronics in 2d materials. *Nature Reviews Materials*, 1(11):1–15, 2016.

[312] Wei Han. Perspectives for spintronics in 2d materials. *Apl Materials*, 4(3):032401, 2016.

[313] Shengcai Hao, Matthew Z Bellus, Dawei He, Yongsheng Wang, and Hui Zhao. Controlling exciton transport in monolayer mose 2 by dielectric screening. *Nanoscale Horizons*, 5(1):139–143, 2020.

[314] Pierluigi Cudazzo, Lorenzo Sponza, Christine Giorgetti, Lucia Reining, Francesco Sottile, and Matteo Gatti. Exciton band structure in two-dimensional materials. *Physical review letters*, 116(6):066803, 2016.

[315] Srilatha Arra, Rohit Babar, and Mukul Kabir. Exciton in phosphorene: Strain, impurity, thickness, and heterostructure. *Physical Review B*, 99(4):045432, 2019.

[316] Pierluigi Cudazzo, Ilya V Tokatly, and Angel Rubio. Dielectric screening in two-dimensional insulators: Implications for excitonic and impurity states in graphane. *Physical Review B*, 84(8):085406, 2011.

[317] Chendong Zhang, Amber Johnson, Chang-Lung Hsu, Lain-Jong Li, and Chih-Kang Shih. Direct imaging of band profile in single layer mos2 on graphite:

quasiparticle energy gap, metallic edge states, and edge band bending. *Nano letters*, 14(5):2443–2447, 2014.

[318] AR Klots, AKM Newaz, Bin Wang, D Prasai, H Krzyzanowska, Junhao Lin, D Caudel, NJ Ghimire, J Yan, BL Ivanov, et al. Probing excitonic states in suspended two-dimensional semiconductors by photocurrent spectroscopy. *Scientific reports*, 4(1):1–7, 2014.

[319] Kristian Sommer Thygesen. Calculating excitons, plasmons, and quasiparticles in 2d materials and van der waals heterostructures. *2D Materials*, 4(2):022004, 2017.

[320] Liam Britnell, Ricardo Mendes Ribeiro, Axel Eckmann, Rashid Jalil, Branson D Belle, Artem Mishchenko, Y-J Kim, Roman V Gorbachev, Thanasis Georgiou, Sergei V Morozov, et al. Strong light-matter interactions in heterostructures of atomically thin films. *Science*, 340(6138):1311–1314, 2013.

[321] Michele Buscema, Joshua O Island, Dirk J Groenendijk, Sofya I Blanter, Gary A Steele, Herre SJ van der Zant, and Andres Castellanos-Gomez. Photocurrent generation with two-dimensional van der waals semiconductors. *Chemical Society Reviews*, 44(11):3691–3718, 2015.

[322] Hari Singh Nalwa. A review of molybdenum disulfide (mos 2) based photodetectors: from ultra-broadband, self-powered to flexible devices. *RSC advances*, 10(51):30529–30602, 2020.

[323] Matteo Salomoni, Rosalinde Pots, Etiennette Auffray, and Paul Lecoq. Enhancing light extraction of inorganic scintillators using photonic crystals. *Crystals*, 8(2):78, 2018.

[324] Luca Banszerus, Michael Schmitz, Stephan Engels, Jan Dauber, Martin Oellers, Federica Haupt, Kenji Watanabe, Takashi Taniguchi, Bernd

Beschoten, and Christoph Stampfer. Ultrahigh-mobility graphene devices from chemical vapor deposition on reusable copper. *Science advances*, 1(6):e1500222, 2015.

[325] Alexey Chernikov, Timothy C Berkelbach, Heather M Hill, Albert Rigosi, Yilei Li, Burak Aslan, David R Reichman, Mark S Hybertsen, and Tony F Heinz. Exciton binding energy and nonhydrogenic rydberg series in monolayer ws 2. *Physical review letters*, 113(7):076802, 2014.

[326] Sungjin Wi, Hyunsoo Kim, Mikai Chen, Hongsuk Nam, L Jay Guo, Edgar Meyhofer, and Xiaogan Liang. Enhancement of photovoltaic response in multilayer mos2 induced by plasma doping. *ACS nano*, 8(5):5270–5281, 2014.

[327] Carlos Forsythe, Xiaodong Zhou, Kenji Watanabe, Takashi Taniguchi, Abhay Pasupathy, Pilkyung Moon, Mikito Koshino, Philip Kim, and Cory R Dean. Band structure engineering of 2d materials using patterned dielectric superlattices. *Nature nanotechnology*, 13(7):566–571, 2018.

[328] Terirama Thingujam, Dong-Hyeok Son, Jeong-Gil Kim, Sorin Cristoloveanu, and Jung-Hee Lee. Effects of interface traps and self-heating on the performance of gaa gan vertical nanowire mosfet. *IEEE Transactions on Electron Devices*, 67(3):816–821, 2020.

[329] Natalia S Rytova. Screened potential of a point charge in a thin film. *arXiv preprint arXiv:1806.00976*, 2018.

[330] Hennrik Schmidt, Shunfeng Wang, Leiqiang Chu, Minglin Toh, Rajeev Kumar, Weijie Zhao, AH Castro Neto, Jens Martin, Shaffique Adam, Barbaros Ozyilmaz, et al. Transport properties of monolayer mos2 grown by chemical vapor deposition. *Nano letters*, 14(4):1909–1913, 2014.